Investigation of dielectron production in quasi-free $p - n$ scattering at $1.25GeV$ with HADES

mgr Radosław Trębacz

Thesis Supervisor

dr hab. Piotr Salabura, JU prof.

Faculty of Physics, Astronomy and Applied Computer Science

of the Jagiellonian University

Cracow, 2012

Contents

Abstract

Investigation of dielectron pair production in quasi-free $n-p$ interactions using deuterium beams on proton target at kinetic energy of $1.25 GeV/u$ is presented. Detection of spectator proton from deuterium break-up at forward angles ($0.3^\circ < \theta < 7^\circ$) and electron-positron pairs in High Acceptance Dielectron Spectromter (HADES) located at GSI (Gesellschaft für Schwerionenforschung) allows for detailed analysis of pair production in the $n-p$ reactions. The results are compared with predictions obtained from Monte Carlo simulations assuming known processes of pair production and a realistic detector response. Inclusive invariant mass, transverse momentum and various angular distributions of dielectron pairs are presented and confronted with model calculations. Furthermore, the results are compared with pair production in $p-p$ reactions and $C+C$ collisions to conclude on the dielectron yield excess with respect to predictions of various theoretical models.

Besides aforementioned result, thesis contains also author's contribution to the HADES data acquisition upgrade important for future operation with Au beams.

Chapter 1

Introduction

1.1 Results from previous experiments: DLS experiment

In the last decades large experimental and theoretical efforts have been directed towards the investigation of dilepton production in heavy ion collisions. One should here mention the following experiments, where low-mass dileptons ($0 < M_{e^+e^-} < 1GeV/c^2$) have been studied at three different energy ranges: HADES [1] and DLS [2] at the beam kinetic energy of $1 - 2AGeV$; CERES [3], NA60 [4] and HELIOS [5] in the region of $40 - 200AGeV$ as well as PHENIX [6] at $\sqrt{s_{NN}} = 200\ GeV$.

The DiLepton Spectrometer (DLS) was built at Lawrence Berkeley National Laboratory. The measurements were carried out at the Bevalac accelerator capable to produce proton, deuterium and heavy ion beams in the projectile kinetic energy range of $1-5AGeV$ [7], similar to the one currently available at SIS18 at GSI Darmstadt.

DLS was designed as a magnetic spectrometer consisting of two identical arms which fanned out from the interaction zone on either side of the beam line. A schematic drawing of the spectrometer is shown in Fig. 1.1, where each of the primary spectrometer components are identified.

The spectrometer was composed of the following detectors:

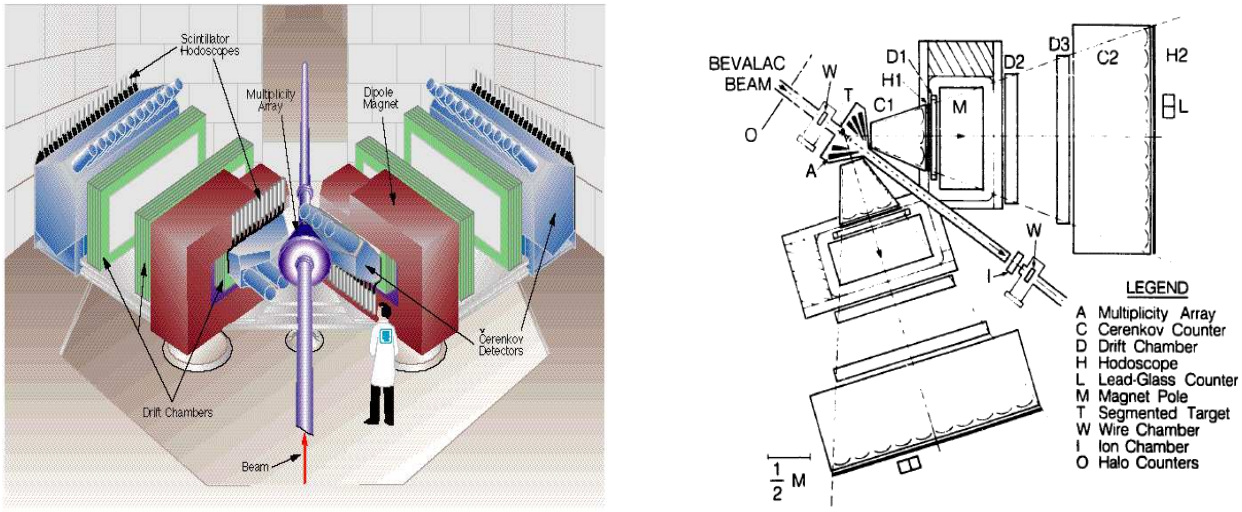

Figure 1.1: Schematic view of DLS spectrometer with multiplicity array, scintillator hodoscopes, dipole magnet, drift chambers and Cherenkov detectors.

1. Electron sensitive Cherenkov counters used for hadron rejection.

2. Three drift chambers in each arm for particle track reconstruction and momentum determination.

3. DLS dipole magnet.

4. Hodoscopes to deliver time of flight for each track for particle identification.

5. A multiplicity array around the target to provide measurement of the impact parameter in HI collision.

6. Lead-glass counters for calibration purposes.

The trigger for data acquisition was a coincidence between the right and the left arm, and within each arm a coincidence between the four counters (front and rear hodoscopes and front and rear Cherenkov detectors) [8]. The relative mass resolution of the entire system was 10% at ρ/ω mass region.

DLS measured the dilepton invariant mass spectra for $p+p$, $p+d$ collisions with beam energies from $1.04GeV$ to $4.88GeV$ and $Ca+Ca$ at 1 GeV and 2 GeV [2], and $C+C$ at $1.04GeV$ [9].

The spectra for $p+p$ and $d+p$ collisions are presented in Fig. 1.2. One can notice the remarkable difference in shape between both collision systems at low beam energies. However, when the beam energy increases, the shape difference disappears and the *pd* cross section becomes approximately twice the *pp* cross section for all masses manifesting same cross sections for pair production in $p+p$ and $p+n$ collisions.

The obtained inclusive distributions of the invariant mass of e^+e^- for these energies can be expected to be composed of following sources (see for example [9] and Fig. 1.6):

1. $\pi^0 \rightarrow \gamma\ e^+e^-$ Dalitz decay channel which creates a dominant peak at low masses ($M_{e^+e^-} < 140MeV/c^2$). It is not clearly seen due to limitations in the DLS acceptance.

2. Dalitz decays of $\Delta \rightarrow Ne^+e^-$, $\eta \rightarrow \gamma\ e^+e^-$ that contribute to the e^+e^- yield in the intermediate mass region ($140MeV/c^2 < M_{e^+e^-} < 550MeV/c^2$).

3. Dalitz decays of higher baryonic resonances as N^* or Δ^*, or two-body decays of the vector mesons (ω/ρ) into e^+e^- contributing for the highest masses ($M_{e^+e^-} > 550MeV/c^2$).

In general, any hadron which has a decay branch leading to a real photon has also a decay branch which produces a dielectron [10] but with lower probability, because of additional coupling constant α. Thus, hadron decays can be divided into two sub-categories: two-body and three-body (Dalitz decays).

There are only two known particles which can be produced in the beam energy range of interest ($1.25GeV$) and exhibit two-body decay to an electron-positron pair. These are the π^0 and, due to its large width, the ρ meson. However, since the branching ratio of $\pi^0 \rightarrow e^+e^-$ is too low $(6.46 \pm 0.33) \times 10^{-8}$ [11] it cannot be seen in the spectra.

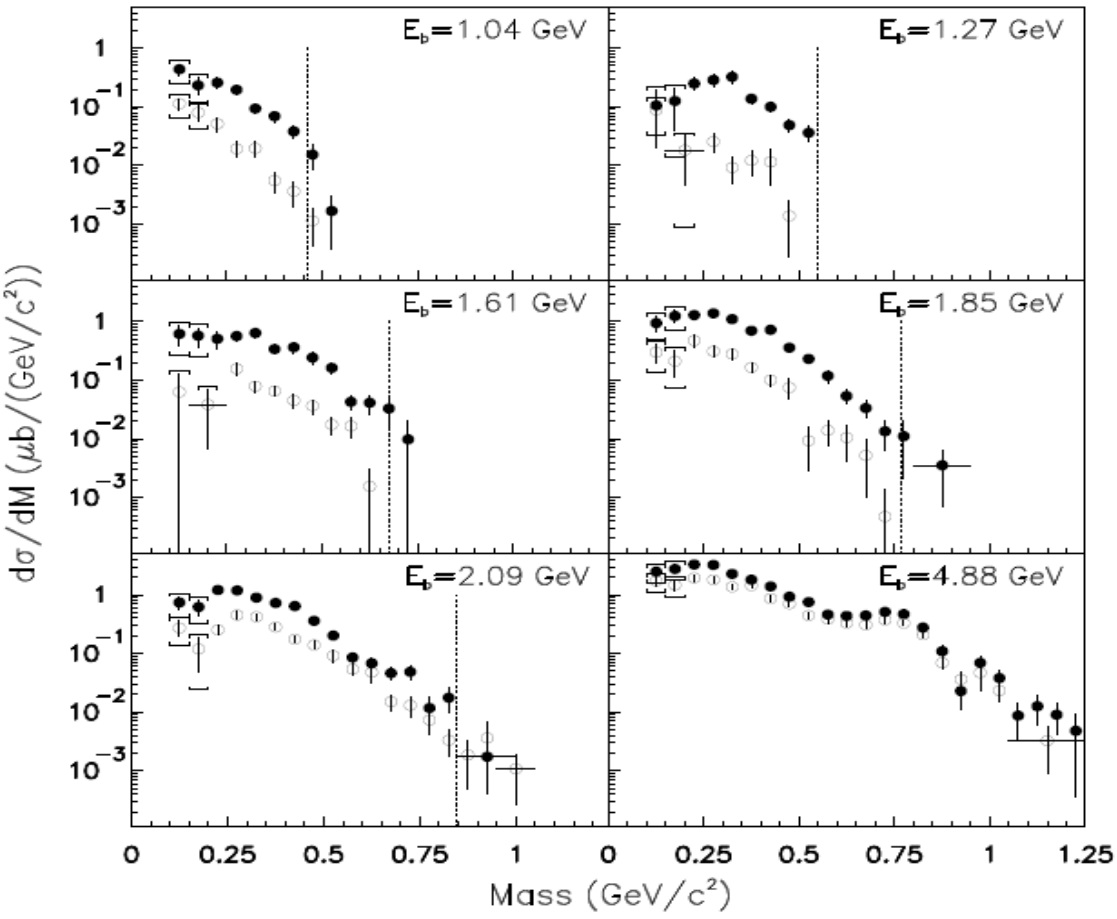

Figure 1.2: Acceptance-corrected mass spectra for the *pd* (filled circles) and *pp* (open circles) systems measured in DLS [14]. The brackets above and below the low mass data points indicate systematic uncertainties in the shape of the spectra. The dashed lines indicate the kinematical upper limit on the pair mass in the *pp* system.

There are several hadrons which undergo three-body Dalitz decays, including the $\Delta \rightarrow Ne^+e^-$ resonance [12] and the neutral mesons [13] $\pi^0, \eta \rightarrow e^+e^-\gamma$. Unlike the two-body decays which can produce recognizable peak in the invariant mass spectra, Dalitz decays produce continuous mass distributions, making isolation of the individual contributions a

more difficult task.

Finally, dielectron production from N-N bremsstrahlung processes is another (poorly known) category of production process. It will be described in detail in the next chapter and was one of the main objectives studied in this thesis.

Summarizing, in the vicinity of $1.25GeV$, sources of dielectrons could be divided into three general categories:

1. Three-body Dalitz decays (π^0, η, $\Delta \rightarrow \gamma e^+e^-$).
2. Hadronic bremsstrahlung (NN $\rightarrow$ NN e^+e^-).
3. Two-body decays ($\rho \rightarrow e^+e^-$).

The measured spectra of dielectron pairs are only qualitatively in agreement with aforementioned sources as well for the $p + p$ and the $n + p$ reactions [18]. Furthermore, going to $C + C$ and $Ca + Ca$ discrepancies become very large [15] and could neither be explained by including the in-medium modified ρ spectral function, nor by a meson mass dropping scenario, which assumes the ρ mass lowering as a function of the nuclear matter density [16]. This case has been named in literature as "DLS puzzle" [9]. The observed discrepancy between theory and the DLS data was one of the main motivations to built HADES experiment and explore the dilepton signal in the same energy range as DLS, but with much better acceptance and resolution. The main question to be answered was wether the observed excess is due to in-medium effects or not properly included (or missing) elementary dielectron production sources.

1.1.1 Bremsstrahlung

A possible candidate process which can be responsible for the missing yield is the poorly known nucleon-nucleon bremsstrahlung. This process is responsible for an electromagnetic radiation created during the change of velocity or direction of charged nucleon due to the strong interactions. The bremsstrahlung process can be studied experimentally in proton-proton and proton-neutron collisions, but the physics of $np \rightarrow np\gamma$ reaction differs from

that of $pp \to pp\gamma$. For example, in a classical picture np electric dipole radiation is allowed, whereas in pp the lowest allowed multipolarity is electric quadrupole. As a consequence, pp cross section is expected to be smaller than in the case of np, at least for small beam energies.

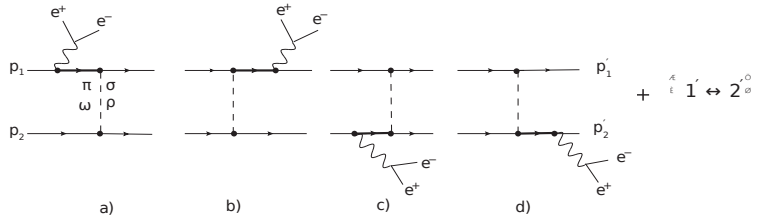

Figure 1.3: Bremsstrahlung diagrams for the process $N_1 + N_2 \to N_1' + N_2' e^+e^-$, where N_1 and N_2' stand for protons and N_2 and N_1' denote nucleons, in the one photon and one-boson exchange approximation (thick lines denotes propagators of either nucleons or baryon resonances) [17].

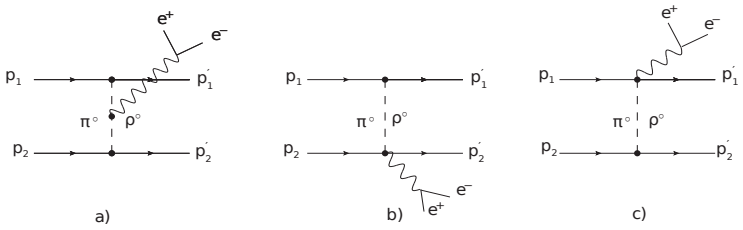

Figure 1.4: Contribution of meson exchange currents (a) and seagull terms (b), (c) for the $N_1 + N_2 \to N_1' + N_2' e^+e^-$ process [17].

More precisely, the N-N bremsstrahlung process is calculated using One Boson Exchange (OBE) models, where the nucleon-nucleon interactions are represented by exchange of mesons. Respective Feynman diagrams, among which one can distinguish channels with a resonance propagation, like Δ or quasi-elastic processes without nucleon excitation into resonance state are shown in Fig. 1.3 and 1.4, respectively. One should note, that in contrast to the $p+p$ channel for the $p-n$ channel an exchange of charged mesons responsible

for the charge exchange reactions is possible. One can also separate contribution from the internal diagrams when photon is emitted from the interaction vertex (i.e. Fig. 1.4), and the external diagram in which photon is emitted by one of the nucleons (Fig. 1.3[a-d]). In particular, diagrams where photons are created in the interaction vertex are the most challenging part and very different for the $p-p$ and $p-n$ case.

First method trying to explain these interactions was based on a Soft Photon Approximation (SPA). In this approach the radiation from internal lines, shown in Fig. 1.4*a* is neglected (in other words, photons are radiated only from the initial or from the final charged lines, never from the internal line of exchanged meson) and the strong interaction vertex is assumed to be on shell (which is correct only for small photon energies). It means that it also does not include resonance excitations. According to SPA the strong interaction and the electromagnetic part can be separated and the cross section of the strong-interaction part is just the elastic $N-N$ collision cross section modified by a factor taking into account the phase-space reduction for the colliding particles due to emitted dielectron. Respective cross section can be written as follows:

$$\frac{d\sigma}{dy \quad d^2q_T \quad dM} = \frac{\sigma^2}{6\pi^2}\frac{\overline{\sigma}(s)}{Mq_0^2}\frac{R_2(s_2)}{R_2(s)}, \tag{1.1}$$

$$R_2(s) = \sqrt{1-(m_1-m_2)^2/s}, \tag{1.2}$$

$$s_2 = s + M^2 - 2q_0\sqrt{s}, \tag{1.3}$$

$$\overline{\sigma}(s) = \frac{s-(m_1+m_2)^2}{2m_1^2}\sigma(s), \tag{1.4}$$

where m_1 is the mass of the charged accelerated particle, m_2 is the mass of the second particle, $\sigma(s)$ is the NN elastic cross section weighed by the momentum transfer, s is the total energy of the system squared, s_2 is the squared effective energy of the system after the emision of the $\gamma^\star$, M is the dilepton invariant mass, q_0 denotes the energy, q_T the transverse momentum and y the rapidity of the dilepton pair [18].

This approach has been widely used for the calculation of the bremsstrahlung by different transport groups, and introduced by C. Gale and J. Kapusta [19] in the 80's and

90's.

As an example the early calculation results for the BUU (Boltzmann-Uehling-Uhlenbeck) microscopic transport model [20] is shown in Fig. 1.5. This theoretical approach is derived from a cascade model and assumes that the particles propagate in the mean field potential and collisions are considered as instantaneous interactions between two particles.

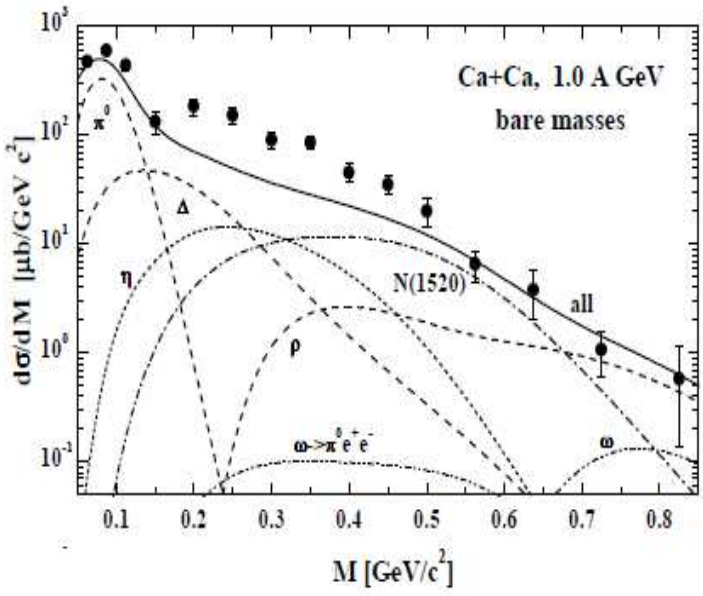

Figure 1.5: The dielectron invariant mass distribution from ^{40}Ca + ^{40}Ca collisions at 1 $AGeV$ measured by the DLS collaboration [20], in comparison with theoretical predictions from BUU transport model.

Fig. 1.5 shows comparison of BUU calculations with the invariant mass distribution of pairs from $Ca + Ca$ collisions. The theoretical cocktail underestimates the DLS dilepton yield in the mid-invariant mass range (between 0.2 GeV/c^2 and 0.6 GeV/c^2).

The next generation of transport models is Hadron-String-Dynamics (HSD) approach which has been developed based on the BUU model. It includes the off-shell dynamics of broad resonances explicitly and particle production via string fragmentation. Low energy hadron-hadron collisions are modeled based on experimental cross sections whereas high

energy inelastic hadron-hadron collisions ($> 40GeV$) are described by the FRITIOF string model [21], [22]. The latter one is based on the assumption that excited hadrons behave as a chain of color dipoles that move like one dimensional relativistic strings. Interactions are introduced via multiple small momentum exchanges between the color dipoles of two overlapping strings. HSD includes the formation and multiple rescattering of the hadrons created in hot and dense nuclear matter. Additionally, a new $n-p$ bremsstrahlung cross section, much larger than the one used before (see Fig. 1.7), adapted from recent OBE (One Boson Exchange) calculations [17] has been implemented.

Fig. 1.6 shows results of the model, obtained by E. Bratkovskaya et al. for $p+d$ and $C+C$ collisions [24]. In the second case theoretical model includes in-medium modifications. They seem to describe the DLS data better, but the quality of the available data does not provide sufficient constraints.

As mentioned above, HSD calculation utilized new prediction for $n-p$ bremsstrahlung OBE model [17]. In this approximation, unlike the SPA, both the internal and the external radiation as well as the influence of interference of different Feynman diagrams are taken into account. The intermediate nucleons or resonances can radiate a virtual photon which decays into a dilepton. Four mesons - $\pi, \sigma, \omega, \rho$ were used as the exchanging mesons. The coupling constants and the vertex form factors were adjusted to the known $N-N$ elastic cross section. This method was also used by Schaefner et al. [26] and later by Shyam et al. [27] but, worth to underline, resulted in much lower cross section as compared to [17] calculations. As one can see in Fig. 1.7 new calculations predict 4 times larger contribution from $N-N$ bremsstrahlung.

Furthermore, the calculation made by de Jong et al. [28] which was based on a full T-matrix approach [29] is also 3 times larger than the corresponding SPA and OBE calculations of Schaefner and Shyam.

Recently R. Shyam and U. Mosel improved their model of dilepton production in pp and quasifree pn reactions at $1.25AGeV$ [30]. They based on the same group of Feynman diagrams (Figs. 1.3 and 1.4) as [17] and used an effective Lagrangian model which is based on the exchange of the π, ρ, ω and σ mesons. It is described in detail in [27], [31]. In

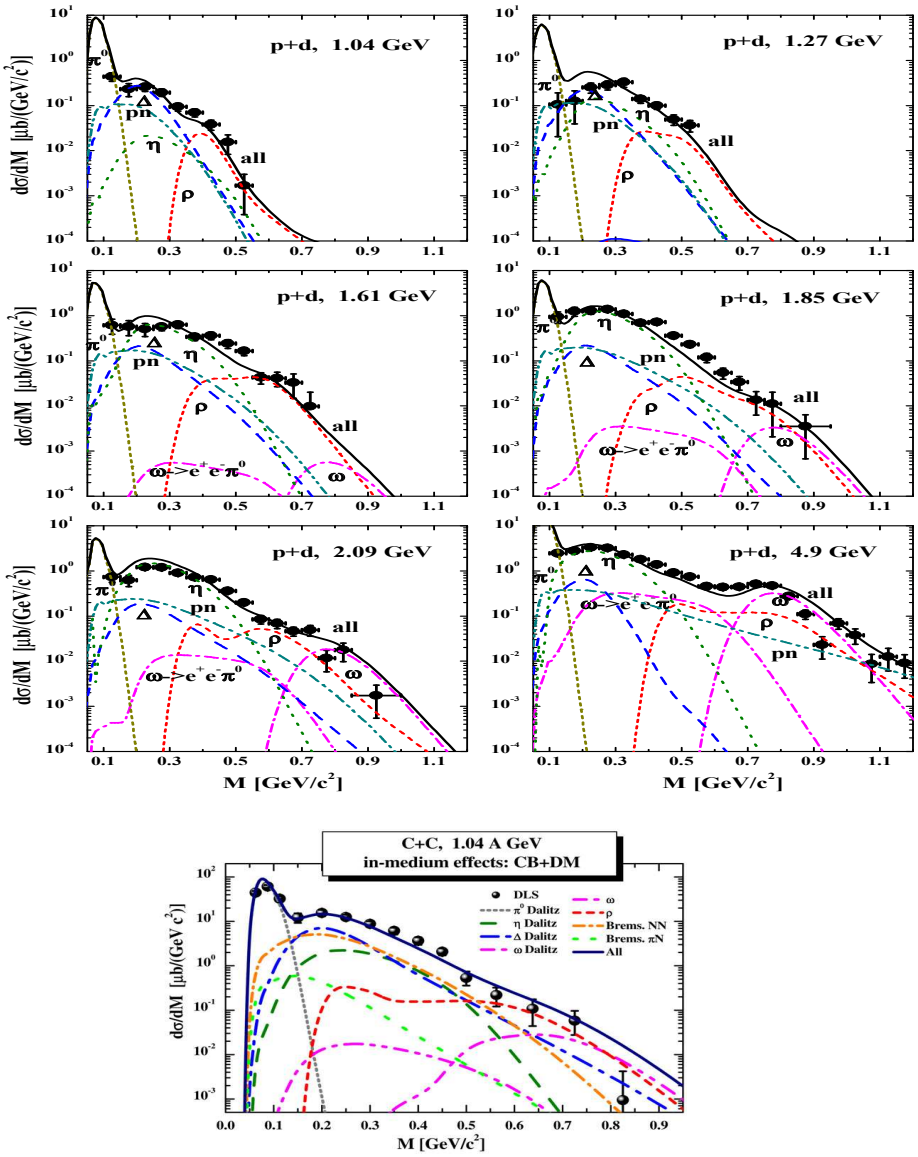

Figure 1.6: Differential cross section for e^+e^- production in pd and $C+C$ reactions at various energies in comparison to the HSD calculations [23], data measured by DLS [14]. Calculated spectrum is an incoherent sum of various processes indicated in the figure.

the calculation the pseudoscalar coupling was used for the nucleon-nucleon-meson vertex. Therefore in contrast to [17], the seagull diagram is not involved in the total Lagrangian. One should note that for the pp reaction only diagrams in Fig. 1.3 contribute, the seagull

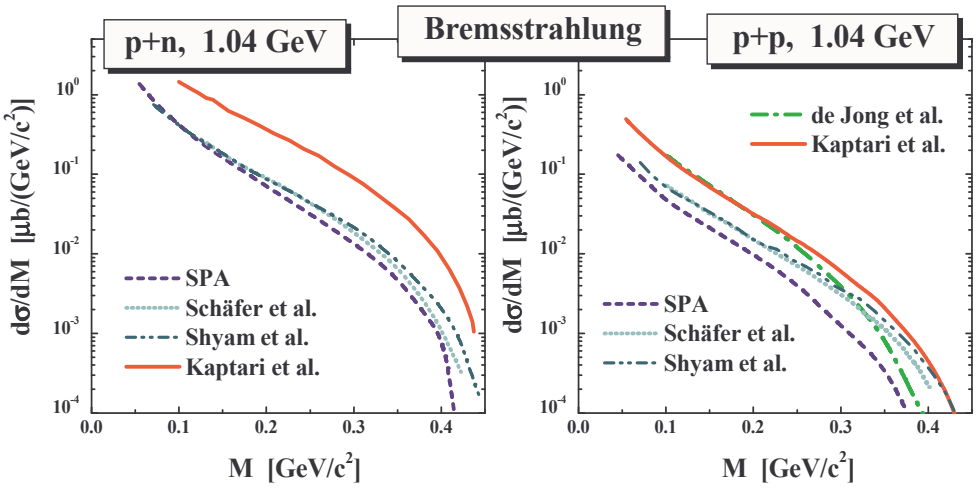

Figure 1.7: The e^+e^- bremsstrahlung from pn and pp reactions. The dashed lines show the SPA results [19], the dotted and dashed-dot-dotted lines correspond to the OBE calculations by Schaefer et al. [26] and Shyam et al. [27], respectively. The dash-dotted line (r.h.s.) displays the T-matrix result from de Jong et al. [28] while the red solid lines show the calculations by Kaptari et al. [17].

terms are not involved even if a pseudovector coupling is used. It makes a difference only for np reaction.

The other very important difference is that in [31] the pion electromagnetic form factor for the charged internal meson line is included. This inclusion makes a strong effect on the cross section for dilepton masses larger than $0.3GeV/c^2$ due to the pion form-factor.

As one can see since the differences between various OBE models are significant and new experimental data on $p-n$ reactions are of large importance to clarify the situation.

Let's now move to new HADES results for $C+C$ collision. Fig. 1.8 shows e^+e^- invariant mass distribution for $C+C$ reactions at $1.0GeV$ (left) and projected into DLS acceptance (right). There is a very good agreement between both experiments, however it leaves interpretation of the "excess" open.

Also in this context, studies of the elementary reactions $p+p$ and $d+p$ are decisive

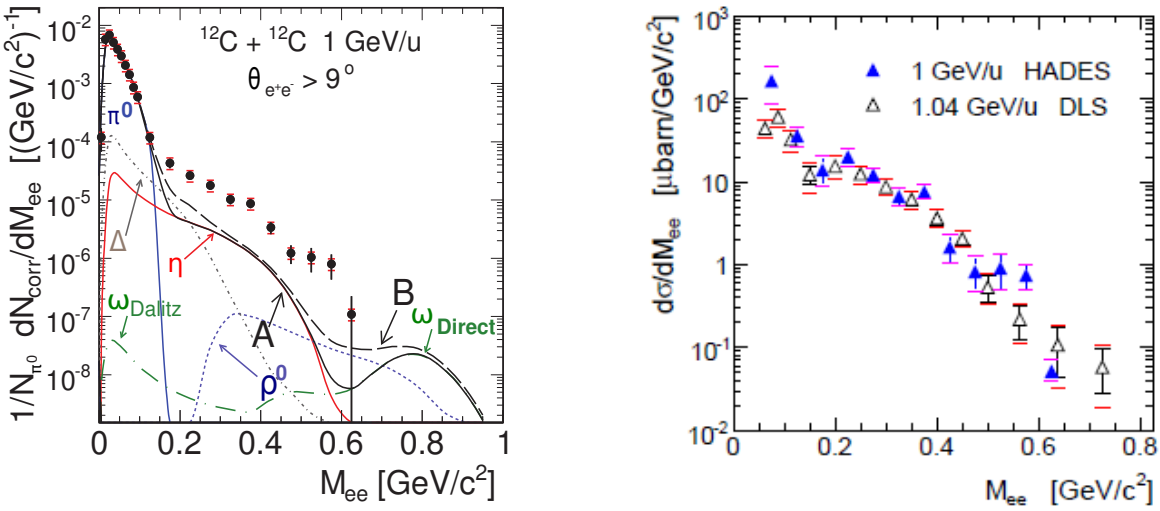

Figure 1.8: Left: e^+e^- invariant mass distribution in the reaction $^{12}C + ^{12}C$ at $1AGeV$ by HADES after efficiency correction and normalization compared with model. Right: direct comparison of the dielectron cross sections measured in this reaction by HADES (full triangles) and at $1.04AGeV$ by DLS (empty triangles) within the DLS acceptance [32].

steps to reveal a basic mechanism of dielectron production, especially the bremsstrahlung channel that is most unclear contribution to the pair yield and does not justify the claim that the excess is related to "medium effects".

1.2 Quasi free p-n reaction and spectator model

Experimental study of $np \rightarrow e+e-X$ reaction is challenging, because there is no pure neutron beam accessible at GSI. In order to solve this problem a deuteron beam was used and np collisions were uniquely identified by tagging forward emitted spectator protons from deuteron break-up in a Forward Wall detector. This experimental technique together with underlying spectator model is discussed in this chapter.

The deuteron consists of only one proton and one neutron that are bound by nuclear force. Despite the fact that the whole deuteron is at rest, its components move with

momenta of identical value, but opposite and continuously changing directions. The momentum distribution of nucleon inside deuteron is well known and is shown in Fig. 1.9, as a result of a simulation using an analytical parametrization of the deuteron wave function, calculated from the Paris potential [33], implemented in the HADES event generator PLUTO [34].

PLUTO is a software package for Monte Carlo simulations of hadronic interactions (nucleon-nucleon, pion-nucleon and nucleus-nucleus) in a few GeV energy range. Empirical models of resonance production, decays (hadronic and electromagnetic) are implemented, motivated by the physics program of HADES. Empirical angular distribution parameterizations for many processes are utilized as well. Also, the spectator model, as described below, for $d + p$ reactions is implemented.

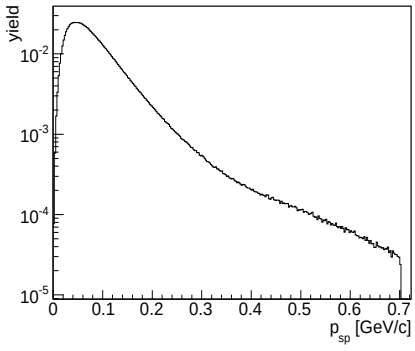

Figure 1.9: Momentum distribution of the nucleons in the deuteron, generated according to the Paris potential [33]. It is in full agreement with momentum produced by Pluto generator.

Since the neutron bound inside a deuteron is not at rest, but moves with the Fermi momentum and this momentum may change from event to event, the total energy $\sqrt{s}$ in the quasi-free proton-neutron reaction also varies from event to event.

Due to a small binding energy of the deuteron (binding energy = $2.2MeV$), neutron struck by the incoming proton may approximately be treated as a free particle in the sense that the matrix element for a given $d+p \rightarrow p_{spec}e^+e^-X$ channel with proton spectator p_{spec}

is identical to that for the free $p + n \rightarrow e^+e^-X$ channel for the same energy. Thus, proton from the deuteron affects the interaction only in terms of the associated Fermi motion of the bound neutron.

In this approximation and assuming that $p+n$ reaction takes place, the proton from the deuteron is considered as a spectator which does not interact with the target proton, but rather escapes untouched and hits the detectors carrying the Fermi momentum possessed at the moment of the collision.

The spectator model was verified by many experiments. The COSY-TOF collaboration checked the validity of the spectator model using $d + p \rightarrow p_{spec}pp\pi^-$ reaction at $p_d = 1.85 GeV/c$ [35] and COSY-11 or WASA@CELCIUS using $p + d \rightarrow n_{spec}pp\eta$. In these experiments all charged particles (and η in case of WASA) in the final state were detected which allowed for the full event reconstruction. Therefore, by the detection of all four ejectiles, the distribution of Fermi momentum of nucleon in deuterium could be obtained and compared to the expected one from the spectator model.

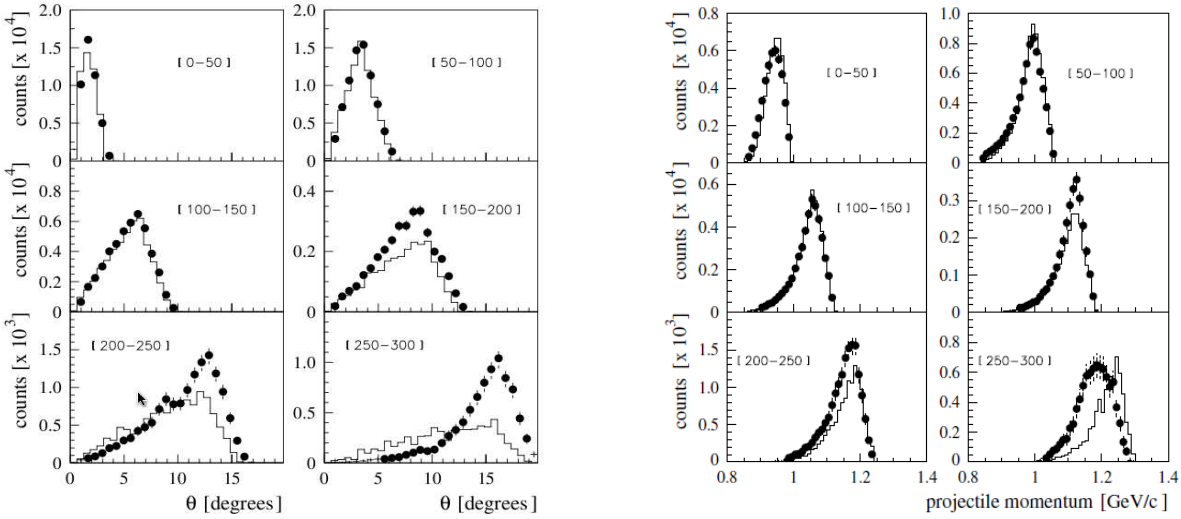

Figure 1.10: Experimentally deduced angular distribution of the spectator proton in the laboratory system (left) and effective neutron projectile momenta (right) for indicated Fermi momentum (given in MeV/c) in comparison with Monte Carlo data [36]. Note changing y-axis scale.

In the Fig. 1.10 the angular distribution (left) of the spectator protons in the laboratory system measured in COSY-TOF in comparison with Monte Carlo simulation is presented, as well as effective neutron projectile momentum (right). The cross sections for π^- production inserted into simulation was previously determined in experiments with a free neutron beam [37]. The momentum distribution within the deuteron was calculated using Paris potential. From the good overall agreement between the experimental data and the Monte Carlo simulations up to $p = 200MeV/c$ of Fermi momentum the authors conclude that a deuteron beam can indeed be used as a valid substitute for a neutron beam [36].

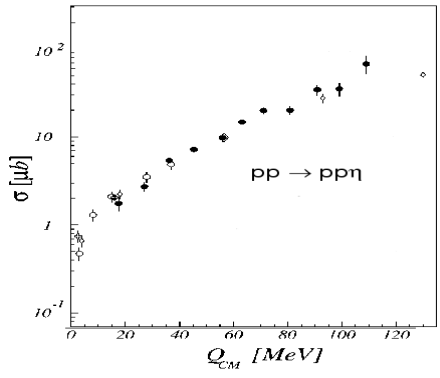

Figure 1.11: Total cross section for the quasi-free (filled circles) $d + p \rightarrow n_{spect}pp\eta$ and free $p + p \rightarrow \eta pp$ (open symbols) reaction as a function of excess energy [38].

Next example for validation of the spectator model is reaction of $p + d \rightarrow n_{spect}pp\eta$ measured with the WASA/PROMICE detector at the CELSIUS storage ring [39]. A proton beam with a kinetic energy of $T_p = 1350MeV$ was collided with deuterium in the target. An η particle was identified by its decay into two photons recorded by the WASA detector, presented in details in [40]. In Fig. 1.11 the cross section of the quasifree $p - p$ and the $p - p$ reactions in the function of excess energy Q_{CM} are compared and they agree within the error bars.

These observations allow to assume that the matrix element for quasi-free meson production from a bound nucleon is identical to that for free meson production from an unbound nucleon, except shadowing effect which is however small ($\sim 5\%$).

Chapter 2

The HADES spectrometer

The High Acceptance Di-Electron Spectrometer (HADES) shown in Fig 2.1 is located at the heavy ion synchrotron (SIS18) at GSI Darmstadt. It was designed for a measurement of dilepton pairs originating from nucleon-nucleon and heavy ion reactions with beam energies up to few GeV per nucleon.

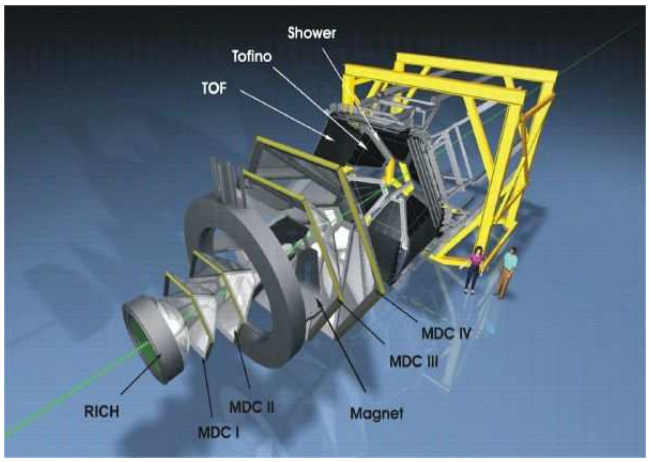

Figure 2.1: 3-dim view of the HADES detector.

The probability to produce a lepton pair in such reactions is very low (10^{-6} per event). The main goals of the detector are following:

- high mass resolution, $\Delta M_{inv}/M_{inv} \simeq 2\%$ at the vector meson (ρ, ω) region,

- large geometrical acceptance for dilepton pairs detection,
- signal to backgroud ratio ~ 1 for the vector meson mass region ($M_{inv} \simeq 0.75 GeV/c^2$),
- high rate capability, up to 10^6 interactions per second, using multilevel trigger scheme.

The HADES spectrometer is built out of six identical sectors, each one covering a polar angle region between $18^\circ \leqslant \Theta \leqslant 85^\circ$, and the full azimuthal angle. In this way the acceptance for dilepton pairs for $M_{inv} \simeq 0.20 GeV/c^2$ amounts to 20% in the mid rapidity region (see Fig. 2.2).

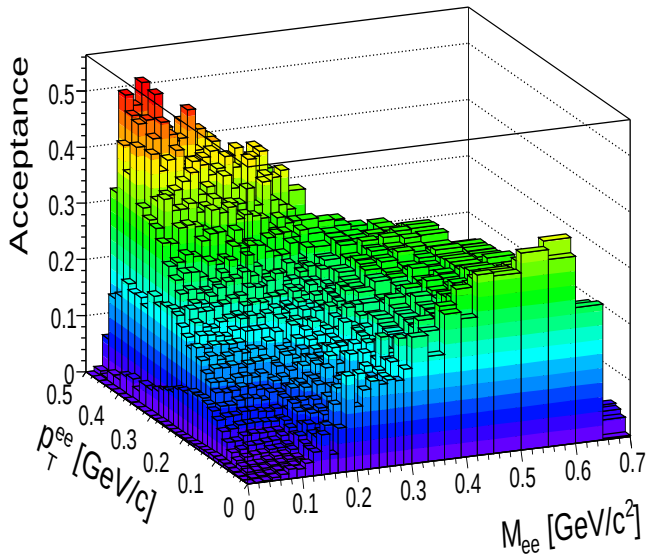

Figure 2.2: Geometrical acceptance for e^+e^- pairs as a function of pair mass and transverse momentum.

The HADES spectrometer consists of several sub-detectors shown in Fig. 2.3:

- START detector composed of Start and Veto modules,
- superconducting magnet ILSE,
- Ring Imaging Cherenkov detector RICH,

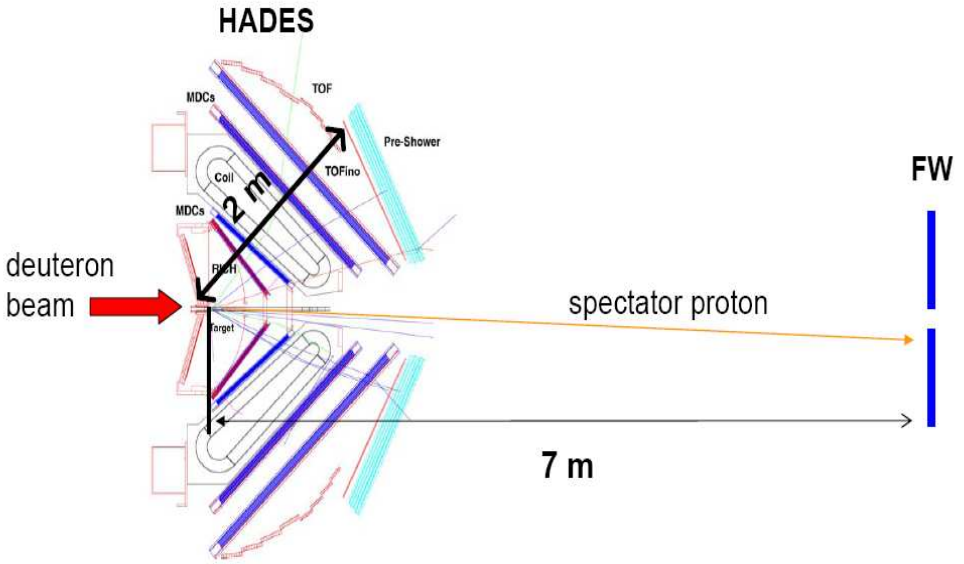

Figure 2.3: Two dimensional cross-sectional view through the HADES spectrometer. In a beam direction: START detector, target, VETO detector, Cherenkov detector RICH, multi-wire drift chambers MDC I and II, super-conducting magnet, chambers MDC III and IV, time of flight detectors TOF and TOFino, electromagnetic cascade detector Pre-Shower and 7 meters downstream Forward Wall detector.

- Four layers of Multi-wire Drift Chambers MDCI-IV,
- time of flight detectors TOF and TOFino (*Time Of Flight*) and an electromagnetic cascade detector Pre-Shower forming Multiplicity Electron Trigger Array (META),
- Forward Wall detector (FW).

Read-out electronics and data acquisition system are designed to work with beam intensities of $10^6 s^{-1}$, resulting in trigger rates of up to $2 \cdot 10^4$ events/s and a primary data rate of $100 MBytes/s$. A two level trigger system reduces this to a rate of 10^3 events/s corresponding to 2 MBytes/s.

The detailed description of the HADES detector can be found in [1].

2.1 START-VETO detector

The START-VETO detector shown in Fig 2.4 is a set of two identical diamond detectors, which size are $15 \times 25mm$ and thickness of $100\mu m$. First module, called START is placed 75 cm upstream, second module - VETO, 75 cm downstream from the target. Each module consists of eight horizontal stripes of variable width ranging from 5.4 mm for the most outer strips to 1.55 mm for the inner strips. These widths are optimized to get a coincidence of one Start strip with one of three nearest, corresponding strips in Veto, in case when there was no reaction in the target. The thickness was choosen to minimize multiple scattering and secondary reactions. The main task of this detector is to provide a signal when a reaction takes place and to give a reference start time for all HADES detectors.

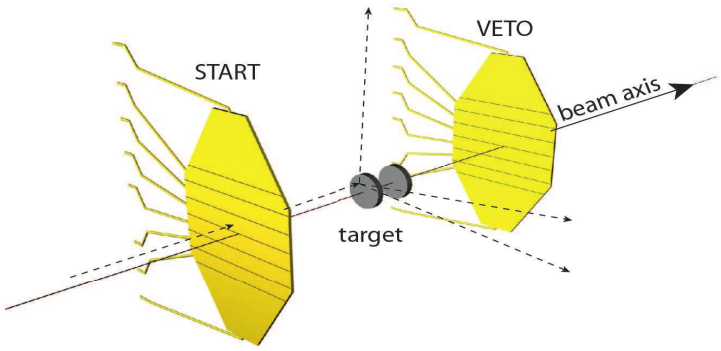

Figure 2.4: START and VETO detectors.

However, for nucleon beams, the diamond START detector could not be used, because of too low efficiency for minimum ionizing particles (MIP). A new prototype detector of high efficiency based on diamond for MIP is under development but it was not available for the presented data. Therefore a method for calculating the time of flight without this detector was used. It will be described later.

2.2 RICH

The Ring Imaging Cherenkov detector [41], which outline is shown in Fig 2.5, forms the innermost part of the spectrometer and was designed to identify electrons and positrons with momenta $p > 0.1 GeV/c$.

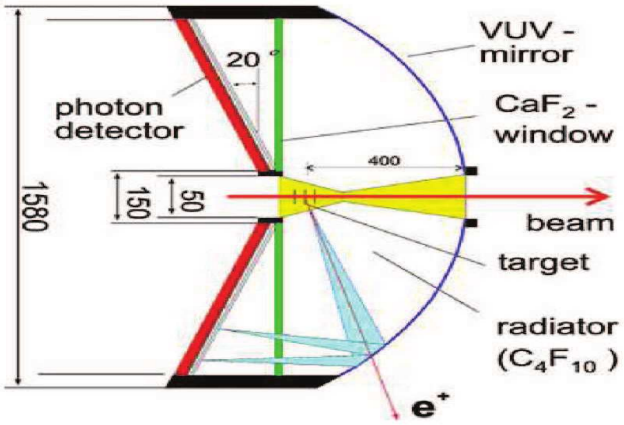

Figure 2.5: Schematic view of the RICH detector and its components: a Carbon shell mirror, a CaF_2 window and a photon detector. All distances are expressed in mm.

The concept of operation of this detector is based on the Cherenkov effect. When a charged particle passes through a radiator at a velocity greater than the speed of light in that medium ($v > v_{th} = c/n$), it generates a cone of light, called Cherenkov radiation, around its trajectory at some constant opening angle θ_c. This angle is given by:

$$\cos(\theta_c) = \frac{1}{n\beta}, \tag{2.1}$$

$$\beta = \frac{v}{c}, \tag{2.2}$$

where n is the medium refraction index, β the velocity of the particle.

By choosing a dielectric medium with an appropriate refraction index, the Cherenkov effect can be a good tool to discriminate leptons from hadrons. In HADES, the RICH detector consists of a radiator gas C_4F_{10}, placed around the interaction region, with the refraction index of n = 1.00151 corresponding to a threshold of the Cherenkov effect of

$\beta \geqslant 0.9985$ and $\gamma = \frac{1}{\sqrt{1-\beta^2}} \geqslant 18.3$, ensuring the hadron blindness of the detector, since all protons and pions are too slow at SIS beam energies to make Cherenkov light.

Photons are reflected by a low mass spherical mirror to a Photon Detector (PD), which additionally focuses them on position-sensitive detector read-out plane. The optical geometry was chosen in such a way that the photons are focused to a ring of almost constant diameter across the whole detector plane.

The reflected photons travers the CaF_2 window that separates the gas volumes of radiator and finally are detected in the PD. The detector covers the whole reflection plane of the mirror, and it is able to detect single photons providing an information about a hit. It consists of six Multi Wire Propotional Chambers (MWPC) with photocatode covered with CsI forming read-out plane. The detection system is very fast, in order to provide a signal for 2^{nd} level trigger to start acquisition when a lepton pair is present in the event.

2.3 Tracking system

The HADES tracking system is designed to measure a deflection of the particle trajectory due to magnetic field. It consists of 24 trapezoidal Multiwire Drift Chambers (MDCs) [42] symmetrically arranged in six identical sectors and forming four tracking planes, counted from I to IV. In each sector, two modules (I and II planes) are located at the front of and two (III and IV planes) behind the toroidal magnetic field generated by a superconducting magnet, as shown in Fig 2.6.

The Iron-Less Superconductive Electromagnet (ILSE) consists of six superconducting coils surrounding the beam axis and produces a toroidal, inhomogeneous field, which reaches a maximum field of $0.7T$ within the acceptance region and bends the particles mainly in the polar (Θ) direction.

Each chamber is constituted by six layers of anode wires located between cathodes and each of them is tilted at a different angle (+40°,-20°,+0°,-°,+20°,-40°) (see Fig. 2.6) in order to have a better reconstruction ability of particle trajectories. Four chamber types contain almost 27000 drift cells each, with increasing size from $5 \times 5cm^2$ for plane I to $14 \times 10cm^2$

for plane IV. Each particle, while crossing drift cells, ionize the gas and produces electrons and positive ions along its trajectory. Drifting electrons and ions make a signal on anode wires, after a time proportional to the distance from the wire. This signal provides the Start to a time measurement, while the Stop is provided by the external detector (e.g. delayed START detector signal). The drift times are converted into the minimal distance of the particle trajectory to the anode wire.

By correlating hits belonging to one track on different chambers in the same sector, before and after the magnetic field region, the full track of the particle is reconstructed. Knowing the field map the particle momentum is calculated.

The HADES tracking system has been optimized for a very good electron momentum resolution. A spatial cell resolution is $140\mu m$ which corresponds to a momentum resolution given by:

$$\Delta p/p \;=\; 1.0 + 3.6p\;[\%/(GeV/c)]. \tag{2.3}$$

The detection efficiencies for minimum ionizing particles detected in the two inner MDC'c reach about 97% per chamber, whereas for the outer drift chambers almost 100%.

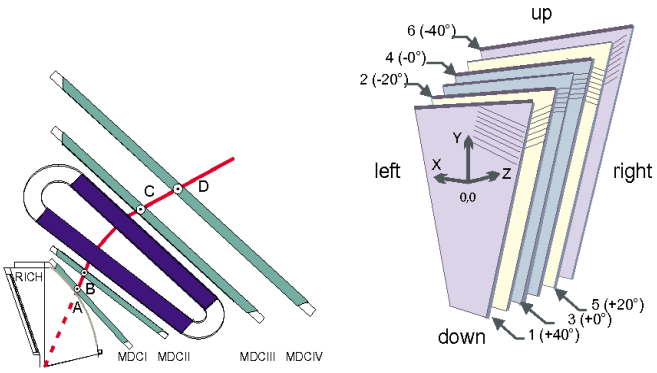

Figure 2.6: Schematic view of the tracking system. Left: arrangement of the MDC chambers and the magnetic coils. Right: view of the six anode wire frames inside a drift chamber.

2.4 META detectors

The Multiplicity Electron Trigger Array (META) is the outermost detector system of the HADES spectrometer and is composed of:

- large granularity Time Of Flight detector TOF covering polar angles (44° - 88°),
- small granularity Time Of Flight detector TOFino covering polar angles (18° - 45°),
- a Pre-Shower detector covering polar angles (18° - 45°).

It is responsible for a fast counting of the charged particles in each event in order to provide particle multiplicity which is a impulse for the first level trigger selection.

META measures the time of flight of each detected particle in order to provide particle identification. Moreover, the fast determination of the impact position of each particle, spatially correlated to the position in the hadron-blind RICH detector, allows to perform a second-level trigger search for electron tracks.

2.4.1 TOF

The TOF detector [43] follows the six-fold symmetry of the whole spectrometer covering polar angles from 44° up to 88°. Each sector consists of eight modules and each module contains a set of eight scintillator rods connected on both sides to photomultipliers.

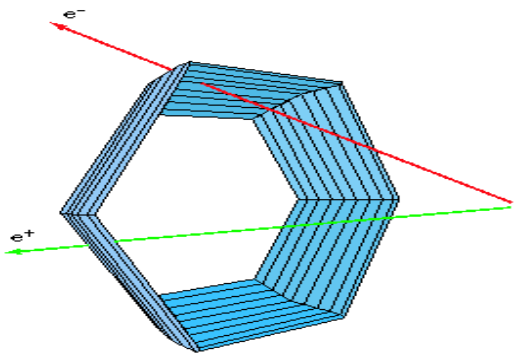

Figure 2.7: The Time Of Flight detector.

A particle which hits a rod deposits energy which is converted into a light signal. The signal reaches the pad edge and is converted into a voltage signal by a photomultiplier.

The TOF detector provides the particle identification by measuring the time between the START detector and the particle arrival signals. Additionally, assuming a given path lenght, it measures the velocity of the particle.

From the measured signals (t_{left} and t_{right}) the time of flight (t_{tof}) of particles, the hit position on the rod (x) and the energy deposited in the rod by the passing particle (ΔE) can be extracted. They can be calculated as follows:

$$t_{TOF} = \frac{1}{2}(t_{right} + t_{left} - \frac{L}{v_{group}}), \tag{2.4}$$

$$x = \frac{1}{2}(t_{right} - t_{left})v_{group}, \tag{2.5}$$

$$\Delta E = k\sqrt{A_{left}A_{right}} * e^{L/\lambda_{at}}, \tag{2.6}$$

where t_{right}, t_{left} is the time measured on the left and right side of the rod corresponding to the time between the reaction and the readout of the signal, v_{group} is the group velocity in the rod, L is the length of the rod ($\sim 165mm/ns$), A_{left} and A_{right} are the signal amplitudes at the left and right ends of the rod, λ_{at} represents the light attenuation length of the rod ($3.8m$) and k is a constant.

The time resolution was estimated to be $150ps$, which corresponds to a spatial resolution of $2.5cm$.

2.4.2 TOFino

For time of flight detector measurements at polar angles $\Theta < 45°$ system called TOFino, shown in Fig. 2.8, is used. It is divided into six sectors, each consisting of four scintillator paddles, arranged radially with respect to the beam axis. The light is collected only from the wide side of each paddle.

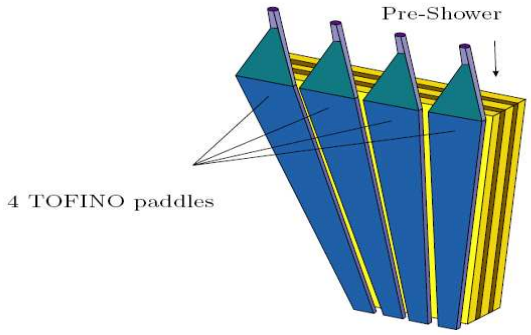

Figure 2.8: TOFino detector.

In order to calculate the time of flight, the following equation is used:

$$tof = t - \frac{x}{V_g}, \tag{2.7}$$

where t represents the calibrated time interval between the reaction and the signal from the paddle, V_g is the light group velocity in the paddle, and x is the distance from the hit position on the paddle.

In contrast to the TOF detector, only one edge is coupled to a photomultiplier, therefore there is no information about the hit position. However, since the TOFino detector is mounted directly in front of the Pre-Shower detector, it provides the particle hit coordinates on the paddle.

The time resolution ($420ps$) and double hit capability of TOFino are worse than those of the TOF detector. Its operation is limited to low multiplicity reactions. Recently, TOFino has been replaced by high granularity Resistive Plate Chamber [44] system.

2.4.3 Shower

The main aim of the Pre-Shower detector [45] is to identify electrons and positrons for low polar angles ($\theta < 45°$) by means of the electromagnetic shower detection. In this region the separation of electrons from hadrons is more difficult than at large angles due to higher hadron momenta and large hit densities. For this reason the Pre-Shower detector is

located directly behind the scintillator paddles of the TOFino and provides also position measurement.

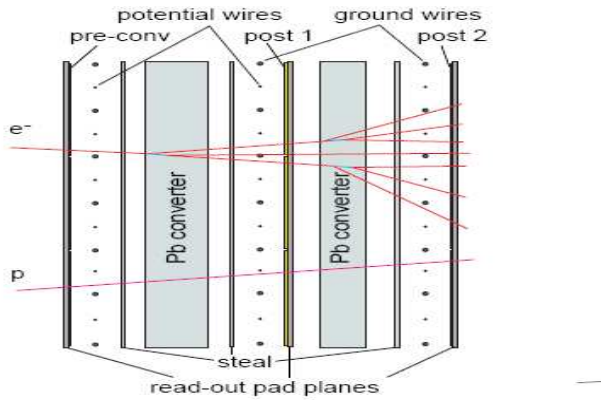

Figure 2.9: Schematic layout of the Pre-Shower detector. The three gas chambers and two Lead converters are shown. Electron-hadron discrimination is performed by comparing the number of particles measured in the chambers in front of and behind the Lead converters.

As shown in Fig. 2.9, each sector module comprises three trapezoidal wire chamber (called pre-, post1- and post2-chamber), separated by two lead converter plates of $x_0 = 2\times$ radiation lengths ($2 \times 0.56cm$). One of each cathode plane is subdivided into individual pads (32×32) array where the induced charge signal is taken from.

The idea of electron/positron identification is schematically presented in Fig. 2.9. A charged particle passing through the gas chambers produces an ionization avalanche, with electrons drifting towards the closest anode wire. This induces a positive charge on the nearby cathode pads connected to charge-sensitive preamplifiers.

The wire chambers are filled with an isobutane-based gas mixture and are operated in the limited self-quenching streamer mode (SQS). In this mode the integrated charge is rather proportional to the number of particles traversing given chamber pad than to their energy loss. Comparison of the integrated charges from the different layers is the basis of the electromagnetic shower recognition and separation of the electrons/positrons from the hadrons. Using both TOF and Pre-Shower detector more than 90% of the hadrons are

rejected and 80% of the electrons are preserved at the same time [45].

2.5 Forward Wall

In order to distinguish pn from pp reaction in $d+p$ collisions, the Forward Wall (FW) has been added to the HADES setup. It detects charged particles at low polar angles ($0.33° < \theta < 7°$), thus can be used to tag the quasi-free pn reaction.

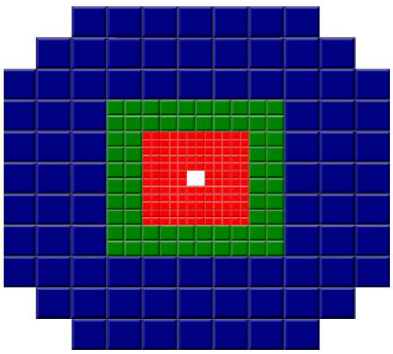

Figure 2.10: Schematic view of Forward Wall.

The FW is placed $7m$ away from the target, as it is shown in Fig. 2.3. It consists of 380 square scintillation detectors of increasing size from $40 \times 40mm^2$ for the inner module to $160 \times 160mm^2$ for the outer one. The thickness of the cells is $2.54cm$. Each cell is equipped with an individual photomultiplier. The estimated time resolution of the FW depends on the scintillator size and varies from 550 to $800ps$.

2.6 Trigger system

The beam intensity for HADES operation is about 10^6 - 10^7 particles per second, which are reduced to $\sim 2 \cdot 10^4$ collision events per second because of 1% interaction probability in the target and specific first level trigger condition (depending on experiment type). The number of events is still too high to be recorded, therefore the second level trigger was designed for capability to distinguish events with electron candidates.

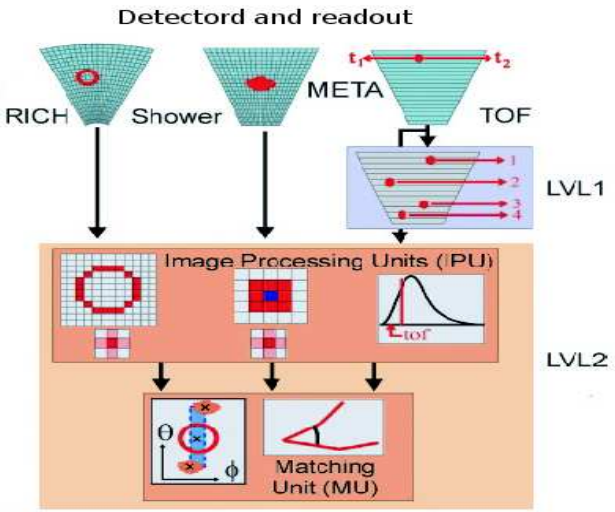

Figure 2.11: The HADES trigger system overview.

2.6.1 First level trigger

The data aquisition system is started by the positive first level trigger (LVL1) decision. The signal from photomultipliers of the TOF and TOFino detector is read out by the trigger module. The decision of the LVL1 trigger is made in very short time $t < 100ns$ based on a hardware analysis of the multiplicities in the META detectors. The LVL1 condition in the $d + p$ experiment was twofold:

1. Hit multiplicities on TOF and TOFino at least equals 2 and a signal on Forward Wall.

2. Multiplicities $\geqslant 2$ in opposite sectors for the elastic scattering detection.

2.6.2 Second level trigger

The second-level trigger (LVL2) uses the online electron pattern recognition. The main task of the LVL2 is to perform fast ($t < 10\mu s$) real-time electron identification and to limit the amount of data written on the tape to events with electron candidates only.

In $d + p$ experiment LVL2 condition to find at least one electron candidate was used. Electron identification performed by the LVL2 trigger is made in two steps:

- searching for the lepton candidates in the corresponding detectors: Cherenkov rings in the RICH, fast particles in the TOF, electromagnetic shower in the Pre-Shower,
- angular correlation (polar and azimuthal) of the lepton candidates in RICH and in TOF/Pre-Shower.

Only events with positive LVL2 decision, and some fraction (down-scaled) of untriggered LVL2 events but with positive LVL1 were recorded. The downscaling purpose is to select and scale down events in a statistical fashion, regardless of whether they contain lepton pair or not, for hadronic analysis and normalization purposes.

This LVL2 trigger has an efficiency $\sim 95\%$ for electron pairs, therefore, for evaluating the number of dilepton events in the data sample respective correction has to be taken into account.

Chapter 3

Analysis

3.1 Introduction

This chapter focuses on descripion of the analysis of experimental data up to the level of efficiency corrected pair distributions. Obtained results are compared to model predictions based on PLUTO simulations done by the author of this thesis. There are the following issues discussed in the following sections:

Section 3.2 gives the details of particle identification (PID) method. An algorithm of electron identification is presented, then e^+e^- signal and background are reconstructed.

Section 3.4 explains normalization of experimental and simulation data. Normalization is obtained by proton-proton elastic scattering yield recorded in the same experiment.

Section 3.5 presents modelling of the physical channels with e^+e^- production of the known sources into the set of spectra which are compared with experimental data.

Section 3.6 describes selection of proton spectator. In order to separate np from pp collisions the detection of charged particle in the FW detector was used. This procedure is efficient and allows to choose only events with a proton as the spectator from $d+p$ collisions.

Sections 3.7 and 3.8 show comparison of the simulated spectra with the corresponding experimental data corrected for detector and reconstruction efficiencies. In particular, inclusive e^+e^- invariant mass, transverse momenta and e^+e^- angular distributions are presented and discussed.

Section 3.9 contains comparison of inclusive e^+e^- spectra obtained in the $C+C$ reaction at $1.25AGeV$ with a superposition of the respective ones but measured in the $p+p$ and $p+n$ (obtained in this thesis) reactions by means of appropriate scaling. Critical assessment of possible new effects appearing in the nucleus collisions are compared to those already present in $N-N$ reactions is evaluated.

Section 3.10 presents reconstruction of $p+n \rightarrow pn(d)e^+e^-p_{spec}$ exclusive channel with two charged hits reconstructed in FW and e^+e^- in the HADES spectrometer. The main aim is to reconstruct the signal of the η production at threshold and search for the de^+e^- final state.

3.2 Lepton identification

Lepton identification is a fundamental part of the analysis presented in this thesis. It consists of the following steps (described below):

- reconstruction of trajectory and momentum of particle,
- Cherenkov rings reconstruction in the RICH detector,
- spatial correlation between RICH rings and tracks,
- particle time of flight calculation,
- application of the momentum dependent condition on particle velocity β measured in the TOF and TOFino detectors,
- electromagnetic shower condition in the Pre-Shower detector.

3.2.1 Trajectory and momentum of particle reconstruction

The momentum of the particle is obtained from its deflection in the magnetic field, which requires measurement of a particle direction before and behind the field. This information is provided by the inner and outer MDC chambers, as well as the META detector. In the first step, the independent straight track parts, in front of and behind the magnetic field region are reconstructed. Then, in the second step, the full track is formed as a combination of the extensions of the inner and outer track segments provided by respective algorithms described in [1], [46]. After that, using the fourth order Runge Kutta algorithm of Nystrom [47] the particle path in the magnetic field of the known strength is reconstructed. Finally, the particle momentum is obtained and the track length necessary for the velocity calculation.

3.2.2 Rings selection

Leptons traversing a radiator in the RICH detector generate a cone of Cherenkov light. Identification of a single lepton track in this detector is based on the ring image recognition, particularly Pattern Matrix method [49].

The pattern of 13×13 pads with weights reflecting the ring image properties is shown in Fig. 3.1. This pattern is overlapped with the RICH sector pad plane and for each pad the measured charge is multiplied with weight from the mask. The sum of obtained values produces a quantity defined as Pattern Matrix Quality (PM quality). This procedure is repeated for all pads in order to find local maxima which are qualified to be ring candidates.

Each of the found rings is characterized by:

1. Number of fired pads.
2. Pattern Matrix Quality parameter.
3. Integrated charge from the pads that forms the ring.
4. Ring centroid - the difference between the center of gravity of charge as deduced from the pulse heights and the fitted geometrical center of the ring.

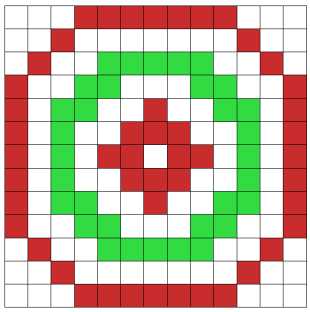

Figure 3.1: Search pattern mask for the ring recognition procedure. Green and red regions represent the positive and negative weights. Own elaboration based on [49].

Fig. 3.2 presents typical distributions of above mentioned parameters.

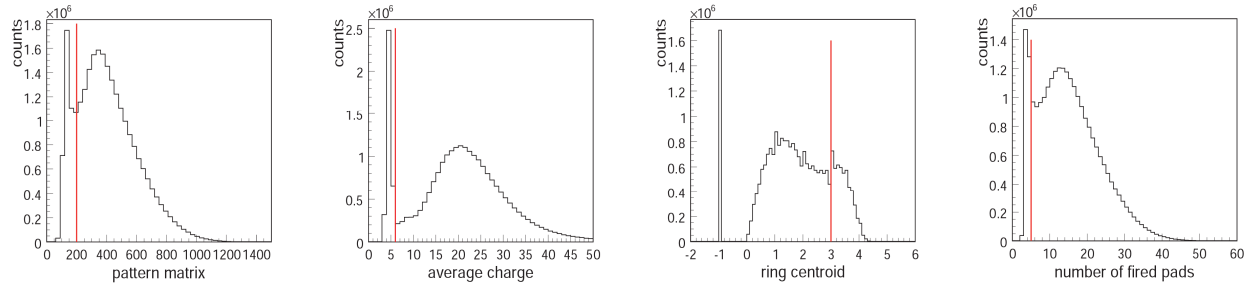

Figure 3.2: Distributions of ring quality parameters with meaning described in the text. The red vertical lines represent the applied cuts.

3.2.3 Spatial correlation between the RICH hits and the inner MDC tracks

In order to find electron tracks a spatial correlation in polar (Θ) and azimuthal (φ) angles is investigated by creation of all possible correlations between the track directions found by the RICH and the inner MDCs track segments. In the first step broad, momentum independent, windows are used:

$$\Delta\Theta = \pm 7^{\circ}\ ;\ \Delta\varphi \sin(\Theta) = \pm 7^{\circ}, \tag{3.1}$$

where $\Delta\varphi$ and $\Delta\Theta$ are differences in the azimuthal and the polar angles, respectively. Factor $\sin(\Theta)$ in $\Delta\varphi\sin(\Theta)$ is used to keep the same solid angle spanned in the case of azimuthal angles difference. In the next step, a more narrow windows as a function of momentum were calculated separately for each sector of the spectrometer.

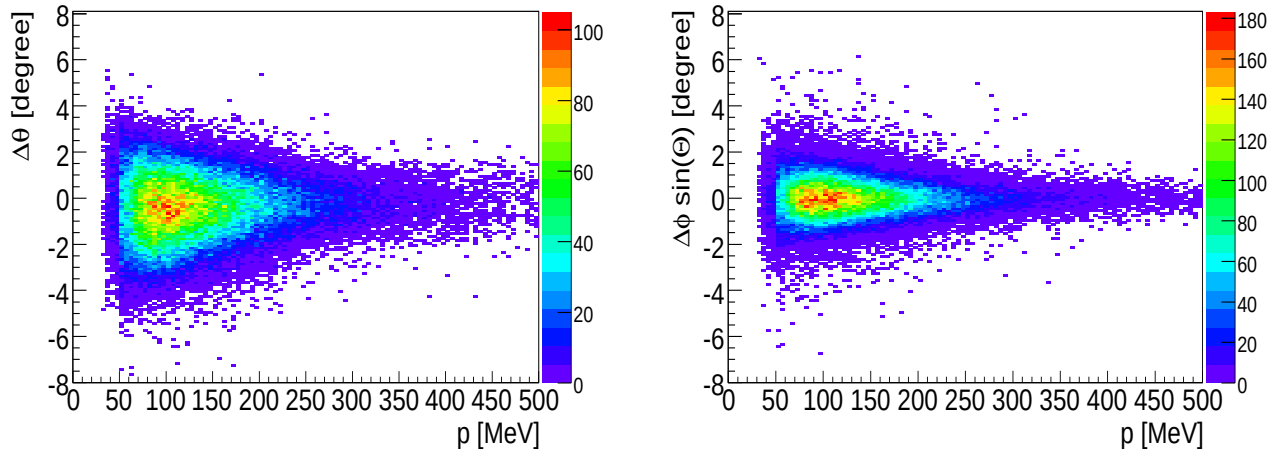

Figure 3.3: Spatial correlation between RICH hits and inner MDCs segment for polar and azimuthal angles for $p < 100 MeV/c$.

To select good lepton tracks these matching windows have been derived as:

$$-3\sigma_\Theta < \Delta\Theta < 3\sigma_\Theta \; ; \; -3\sigma_\varphi < \Delta\varphi\sin(\Theta) < 3\sigma_\varphi, \tag{3.2}$$

where σ_φ and σ_Θ were calculated as a function of momentum from the gaussian fits to the slices of distributions shown in Fig. 3.3.

3.2.4 Time of flight calculation without START detector

A particle momentum reconstruction is prerequisite for Particle Identification (PID). PID in HADES is based on particle mass calculation from the reconstructed velocity (from the measured time of flight and the track length). Since the START detector was not used in this experiment and as a consequence there is no common start time for all tracks in the same event a special method has been invented to overcome this difficulty.

In the first stage, the time calibration of TOF/TOFINO is done using lepton pairs emitted in the same event with energies above few MeV. Assuming that both leptons traveled the same track lengths, their TOF difference must be equal to zero. By setting it to zero on a pad by pad basis, all time offsets were defined.

The reconstruction of particle time of flight is based on the assumption that the particle identity can be determined by different, independent methods. It is possible for electrons and positrons using the RICH detector or pion (π^-) (in case of events without e^+ or e^-), which are the dominant source of negative charged tracks at these energies.

For such events (containing either electrons or negative pions) one can reconstruct, event by event, reaction time and use it as a reference for all other particles in the event. Then, it is achieved by calculation of a time offset:

$$t_{offset} = t_{exp} - t_{theor}, \tag{3.3}$$

where t_{exp} is the measured time for identified electron (or pion) and t_{theor} is its "theoretical" value calculated from the known momentum, mass and distance to the detector. Finally, t_{offset} is added to time of flight of all other particles in the same event.

Electrons can be further discriminated with respect to hadrons by means of spatial correlation between track directions obtained by the RICH and MDC explained below.

3.2.5 Time of flight cut

This condition is based on the time of flight reconstruction explained in the previous section. Leptons move with velocity close to the speed of light, $\beta \sim 1$, which distinguishes them from hadrons. A simply condition on the reconstructed β of particle $\beta > 0.8GeV/c$ was applied. This condition is clearly visible in Fig. 3.6.

3.2.6 Electromagnetic shower condition

The main task of the Pre-Shower detector is to improve the lepton identification at $\Theta < 45°$. It is based on the electromagnetic shower identification through the comparison of

the integrated charge on the 3×3 pads around local maximum measured in the pre-chamber and post1-, post2-chambers, as shown in Fig. 3.4.

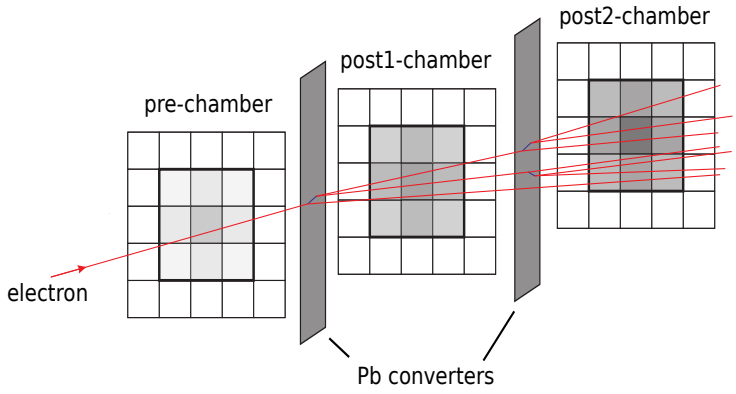

Figure 3.4: Schematic view of the shower algorithm. The larger charge deposition in the post-chambers is the signature of an electromagnetic shower [1].

The criterium which is used reads:

$$\sum Q_{post1,post2}(p) - \sum Q_{pre}(p) \geqslant Q_{th}(p), \tag{3.4}$$

where $Q_{th}(p)$ is the momentum-dependent threshold, based on simulation.

Equation 3.4 is the sum of charges measured in the post1- and post2-chambers after subtraction of the pre-chamber charge. $Q_{th}(p)$ was optimized to obtain a constant electron identification efficiency of 80% over momenta above $0.1 GeV/c$. In Fig. 3.5 distributions of this sum for electrons and hadrons are presented, together with the pion suppression as a function of electron momentum. The achieved pion suppression for $p > 500 MeV/c$ is on a level of an order of magnitude.

Moreover, the information on the energy loss in the pre-chamber is used to eliminate slow hadrons characterized by large energy loss.

Finally, after applying all above cuts the e^+ and e^- regions are separable, see Fig. 3.6, where the distribution of the momentum as a function of the velocity is shown. Sharp vertical lines are for electrons used as reference particles in the reaction time reconstruction.

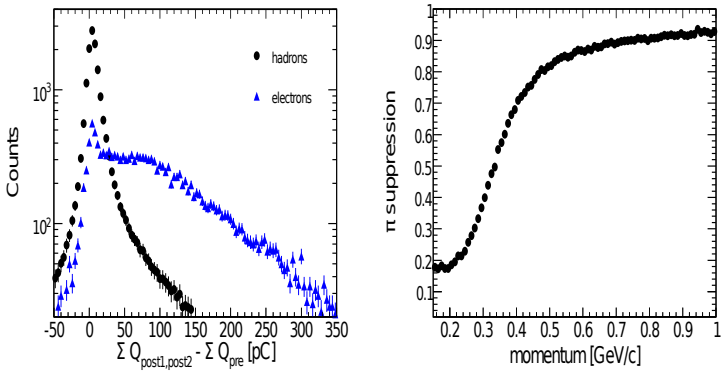

Figure 3.5: Left: Sum of charges presented in Eq. 3.4 for leptons and hadrons. Right: Pion suppression as a function of momentum, i.e. the fraction of pions rejected after the condition for lepton electromagnetic cascade has been applied [1].

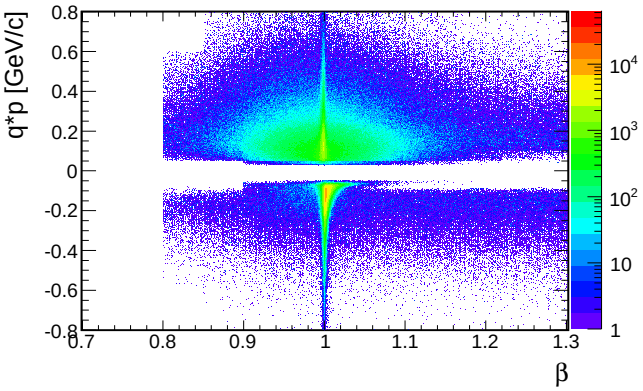

Figure 3.6: Experimental distribution of polarity×momentum vs beta for e^+e^- with graphical time of flight cut [48].

3.3 Inclusive e^+e^- distributions

3.3.1 The conversion background

The main source of background in the e^+e^- final state are pairs produced by a photon conversion. The conversion background originates from external pair conversion of photons mainly from π^0 decay. It is a source of a combinatorial background (CB) arising when

formation of dilepton pairs is done for all possible e^+e^- combinations from the same event. Indeed, a significant part of the reconstructed unlike-sign pairs are those coming not from the same interaction vertex, hence such a fake signal has to be suppressed.

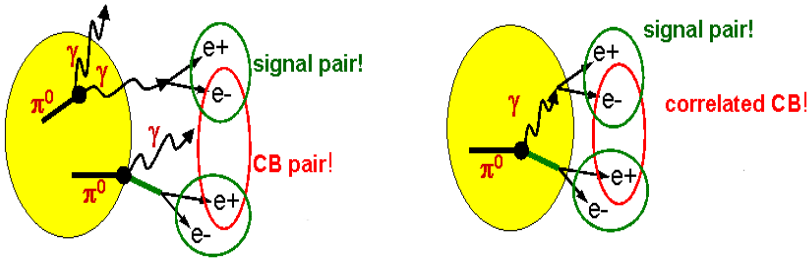

Figure 3.7: The example of the sources of uncorrelated (l.h.s.) and correlated (r.h.s.) combinatorial background.

In more details, the combinatorial background can be observed as an uncorrelated and a correlated background (Fig. 3.7). Typically, the combination between leptons originating from two independent sources gives the contribution to the smooth background. The correlated background originates mainly from the $\pi^0 \rightarrow \gamma\gamma$ decay or the π^0 Dalitz decay, where positron and electron come either from two γ conversions or from the Dalitz decay and from the γ conversion in the same π^0 decay.

In the HADES spectrometer, the combinatorial background is produced in the target or in the radiator gas of the RICH detector or in some parts of the target and RICH construction (flange). For example, photons emitted at the beginning of the target and at large polar angles can hit the RICH flange and convert into e^+e^-. This is shown in Fig. 3.8. They are suppressed using a square cut imposed on lepton tracks with momenta $p < 150 MeV/c$ and emission polar angles $\theta > 65°$ as well as the reconstructed vertex z position of the track below $-50mm$ (in subsequent experiments target was moved more downstream).

The unlike-sign combinatorial background can be estimated in two ways. First of them,

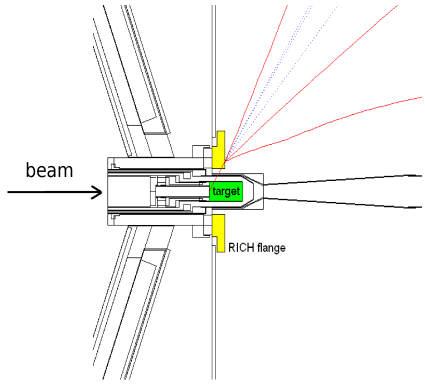

Figure 3.8: The dilepton pair from the conversion process (red lines) in the RICH flange (yellow) around the target (green) [48].

applied in current analysis, is based on the fact that the same-event (SE) like-sign CB is identical to the unlike-sign CB [1]. Therefore the combinatorial background can be obtained from the reconstructed like-sign distribution as:

$$N_{CB} = N_{++} + N_{--} \quad [51]. \tag{3.5}$$

One should note that this method also provides absolute normalization for the combinatorial background estimated by the event-mixing (EM) approach that can be used for heavy ion data (e.g. in e^+e^- analysis of $C + C$ at $1GeV$ data). Event mixing technique relies on selection of electron and positron from different events and combining them to form a combinatorial background. Thus, the CB obtained by the EM method is purely uncorrelated.

Both methods have advantages and disadvantages. The SE method properly describes correlated and uncorrelated CB, and must be used in the case of elementary reactions due momentum and energy conservation which must be preserved for each collision. In case of heavy ion reactions it can be used when dealing with sufficient statistic. For the latter case usually the EM method is used since it does not have statistical limitations and conservation laws do not modify spectra shape of uncorrelated background. However, one should still remember that EM properly describes only shape of uncorrelated CB and it

requires a proper normalization which must be provided the SE method.

The CB reconstruction in $C+C$ analysis is done by using combination of SE and EM methods. For the π^0 region the CB is reconstructed by means of SE method, while for the larger masses ($m > M_{\pi^0}$) the EM method has been chosen.

For $N+N$ reactions SE method must be used since it naturally conserves the total energy in an event which is important for $N+N$ collisions.

3.3.2 The acceptance and efficiency filters

In order to present the simulated data within the HADES acceptance compared to the experimental data after efficiency correction, one has to calculate the acceptance and efficiency filters, respectively. The $Acceptance(p,\theta,\phi)$ and the $Efficiency(p,\theta,\phi)$ are 3-dim matrices defined as follows:

$$Acceptance(p,\theta,\phi) = \frac{N_{accepted}(p,\theta,\phi)}{N_{4\pi}(p,\theta,\phi)}, \tag{3.6}$$

where $N_{accepted}(p,\theta,\phi)$ is the number of simulated particles accepted in HADES detector and $N_{4\pi}(p,\theta,\phi)$ number of particles within the full phase space. $Acceptance(p,\theta,\phi)$ is the probability for a particle emitted from the reaction vertex with a given momentum (p), polar and azimuthal angles (θ,ϕ) to be accepted inside the HADES spectrometer active volume.

Probability that a lepton is fully reconstructed and contributes to the spectrum is determined using the ratio of reconstructed particles to particles within the geometrical acceptance of the HADES spectrometer:

$$Efficiency(p,\theta,\phi) = \frac{N_{reconstructed}(p,\theta,\phi)}{N_{accepted}(p,\theta,\phi)}. \tag{3.7}$$

Using the $Efficiency(p,\theta,\phi)$, the experimental events are corrected for the detector efficiency and analysis cuts and track reconstruction efficiency.

Both matrices have been calculated using Monte Carlo simulation based on GEANT [52] and HADES analysis package [53].

Besides the correction resulting from the efficiency matrix there is a need to correct data for the efficiency of the LVL2 trigger used during the $d+p$ beamtime. The correction appears to be independent on e^+e^- mass, p_t and rapidity, and was estimated to be 0.85.

For the $d+p$ collisions the selection of the quasi-free $n+p$ reaction channel is done by tagging forward emitted spectator protons in the Forward Wall hodoscope shown in Fig. 2.10. The reduction of electron-positron pairs from $p+n$ reaction because of the FW acceptance equals 0.84. This factor is used in experimental as well as in simulation analysis.

Summarizing, the following conditions are applied in the analysis:

1. Spectator selection: at least one of the charged particles with momentum $1.6GeV/c < p < 2.6GeV/c$ is accepted in the Forward Wall.

2. e^+e^- opening angle has to be larger than 9° to eliminate the dilepton pairs coming from γ conversion in the detector material.

3. Efficiency for leptons from the same event has to be larger than 5%. It is used in order to avoid large fluctuations in the efficiency corrections.

The obtained inclusive dilepton invariant mass spectra are presented in Fig. 3.9 for both signal (black) and CB (blue) [left]. Right figure shows e^+e^- signal distribution after efficiency correction.

3.4 Normalization

The number of $p-p$ elastic scattering events from the quasi-free scattering $d+p \rightarrow ppn_{spec}$ collected during the experimental beamtime was used to normalize the experimental e^+e^- spectra and allowed to compare it with the model calculations.

The energy and momentum conservation laws provide the following conditions for quasi-elastic pp pairs selection from $d+p$ collisions:

i) coplanarity:

$$\mid \phi_1 - \phi_2 \mid \sim 180^\circ, \tag{3.8}$$

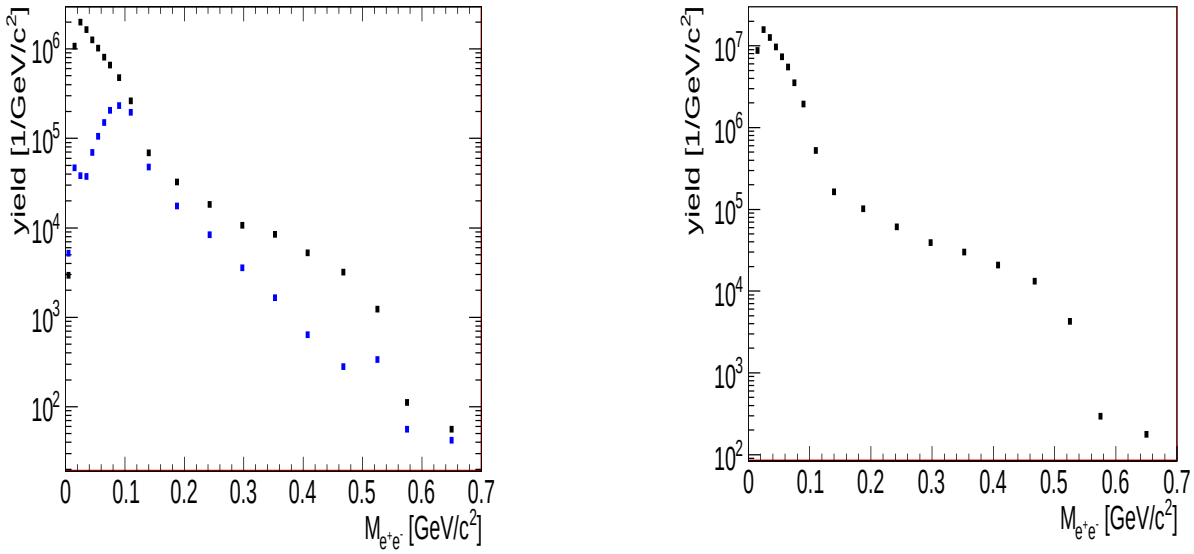

Figure 3.9: Inclusive dielectron invariant mass distribution before normalization to the $p+p$ elastic scattering yield. Left: Signal and combinatorial background. Right: After CB subtraction and efficiency correction.

ii) kinematical constraint on:

$$\tan(\theta_{p1}) \cdot \tan(\theta_{p2}) \sim \frac{1}{\gamma_{cm}^2} = 0.596, \tag{3.9}$$

where ϕ_1, ϕ_2, θ_{p1}, θ_{p2} are azimuthal (ϕ) and polar (θ) angles for measured protons p_1 and p_2; γ_{cm} is the γ Lorentz factor calculated in the center of mass frame. For the fixed kinetic beam energy one has:

$$E_k = 2\gamma^2 m_{pr} - 2m_{pr}, \tag{3.10}$$

where m_{pr} is a mass of proton. In $d+p$ reaction, particles momenta, therefore also γ, are smeared, due to nucleon Fermi momentum known from wave function describing nucleon inside deuterium. Dedicated Monte Carlo simulations with PLUTO generator (section 1.2) show that the observed smearing is well reproduced.

The two-dimensional distribution corrected for proton reconstruction efficiency shown in Fig. 3.10 displays $\Delta\phi$ vs $\tan(\theta_{p1}) \cdot \tan(\theta_{p2})$ correlation. The kinematic boundary of pairs

resulting from the elastic scattering (shown as black square), was set to $2\sigma_{\theta,\phi}$, where $\sigma_{\theta,\phi}$ is a width of a Gaussian fit of azimuthal $(\phi_1 - \phi_2)$ and polar $(\tan(\theta_{p1}) \cdot \tan(\theta_{p2}))$ distributions and amounts to $\sigma_\theta = 0.019$ and $\sigma_\phi = 3.1°$.

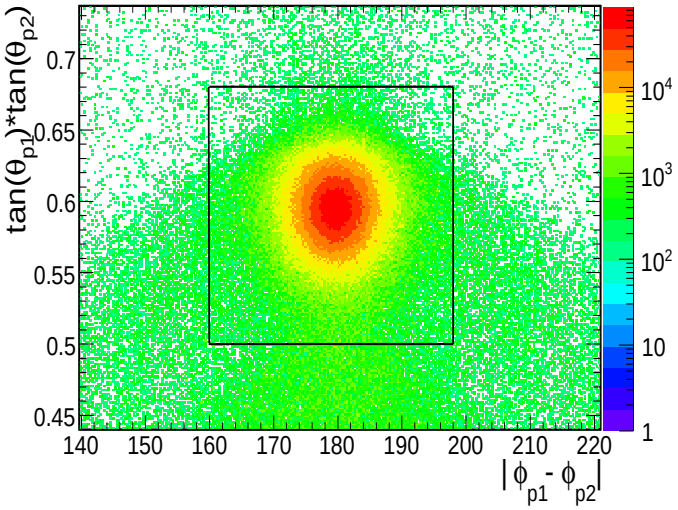

Figure 3.10: $\mid \phi_1 - \phi_2 \mid$ vs. $\tan(\theta_{p1}) \cdot \tan(\theta_{p2})$. The events placed inside a black square were accepted as coming from elastic scattering collisions.

Projections on $\mid \phi_1 - \phi_2 \mid$ and $\tan(\theta_{p1}) \cdot \tan(\theta_{p2})$ show the peaks are close to the expected positions, respectively $\mid \phi_1 - \phi_2 \mid = 179.6°$ $(\sim 180°)$ and $\frac{1}{\gamma_{cm}^2}$=0.596 (~ 0.600).

For the elastic *pp* scattering a squared missing mass of two protons is given by:

$$M^2 = \left(E_{ini} - \sum_i E^i_{out}\right)^2 - \left(\overline{p}_{ini} - \sum_i \overline{p}^i_{out}\right)^2 \tag{3.11}$$

and is shown in Fig. 3.11. Finite momentum resolution of the spectrometer and smearing due to Fermi momentum explain observed widths. Using condition 3.8 and 3.9 one can separate distributions for protons coming out from elastic (red line) and non-elastic events (blue line).

The obtained number of measured elastic scattering events in HADES acceptance after efficiency correction equals $N^{measured}_{elastic} = 9.16 \cdot 10^8$.

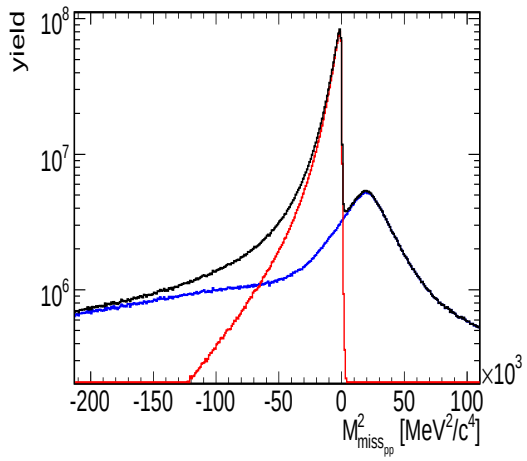

Figure 3.11: The distribution of the square of missing mass of two protons. The yield under red curve corresponds to elastic scattering events, whereas blue curve denotes protons coming from non-elastic reaction, mainly π^0 production. The black curve is the sum of these yields.

In the next step, simulated elastic $p-p$ distributions are compared with the available experimental data obtained at $E_{kin} = 1.2822GeV$ from the EDDA group at COSY synchrotron [54]. The comparison is shown in Fig. 3.12, where a differential cross section of $p-p$ elastic scattering as a function of scattering angle Θ^{CM}_{pr} is presented. The empirical data are marked as black squares, whereas PLUTO simulation as a blue curve. Shapes of these distributions are consistent, what is better seen in Fig. 3.13, where the ratio of two distributions normalized to the same area is shown.

In order to correct the $p-p$ elastic scattering yield for the finite HADES acceptance and reconstruction efficiency respective factor must be calculated. For this purpose distributions of elastic scattering events were generated and filtered through the HADES acceptance (Fig. 3.14) defined in chapter 3.3.1. In order to extract the normalization factor $\sigma(pp_{elastic})/N_{elastic}$, $p-p$ elastic yield reconstructed in HADES has to be projected onto the acceptance of the EDDA experiment, where respective cross section was measured,

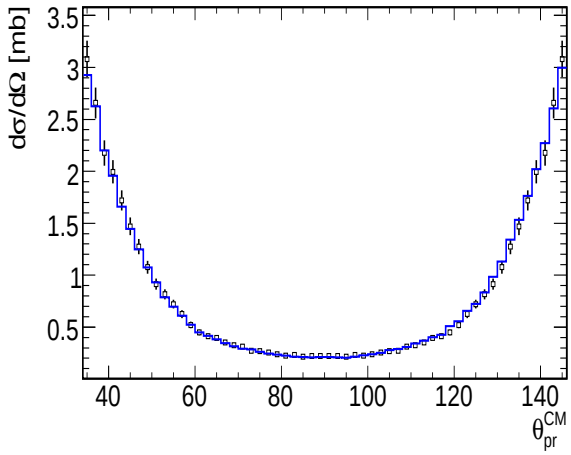

Figure 3.12: Comparison of the $p-p$ differential cross section for elastic scattering as a function of the CM angle for EDDA group (black) and data generated by PLUTO (blue).

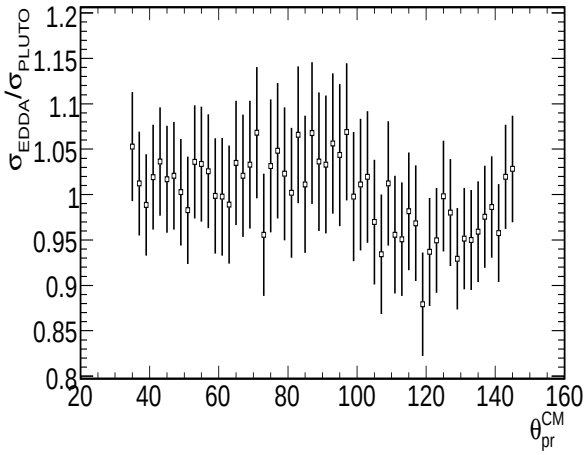

Figure 3.13: Ratio of the experimental and the simulated distribution (shown above).

namely: 42° - 145° in CM, or equivalent 16.5° - 67.8° in the laboratory system. The respective acceptance correction factor amounts to 1.739. Therefore, the final number of elastic scattering events collected during $d+p$ experiment, corrected for the detector acceptance the reconstruction efficiency, is equal:

$$N_{elastic}^{eff,acccor} = 1.59 \cdot 10^9. \tag{3.12}$$

The uncertainty of the normalization was obtained in a two ways. In the first method, it is extracted from differences between simulated and experimental distributions as a function of the scattering angle, shown in Fig. 3.15, as follows:

$$\Delta N_{elastic}^{42^o-145^o} = 1.739 \cdot \sqrt{\sum_{i=42}^{145} \delta_i^2 \cdot f_i^2} = 3.24 \cdot 10^7, \tag{3.13}$$

where δ_i is the yield uncertainty in the i-th bin of the scattering angle given by the difference

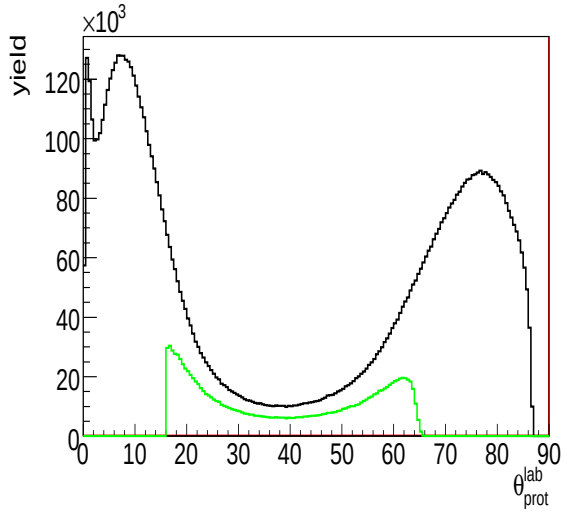

Figure 3.14: Result of elastic scattering simulation in the full solid angle (black) and in the HADES acceptance (green).

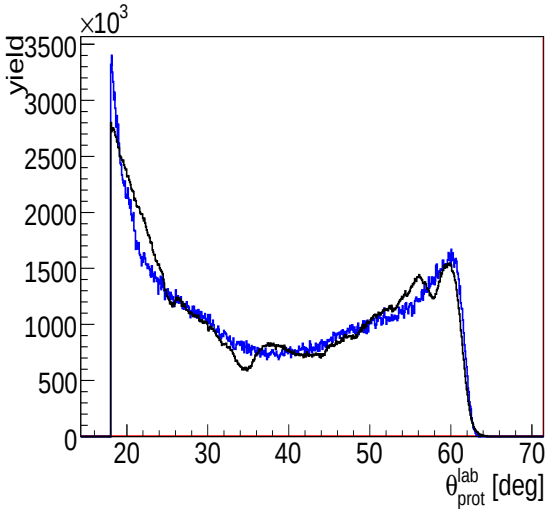

Figure 3.15: Yield of $p-p$ elastic scattering as a function of the scattering angle: simulation (blue) in comparison with experiment (black). Both distributions are normalized to the same area.

between the yield of elastic scattering in the experiment and in the simulation normalized to the same total area and f_i is an abundance weight according to the elastic cross section. The second method to calculate this uncertainty is based on the difference between elastic yields reconstructed in three independent HADES sector pairs. This approach leads to a following equation:

$$\Delta N_{elastic}^{42^o-145^o} = 1.739 \cdot \frac{\sqrt{\sum_{i=1}^{3}(N_i^{sec} - N_{av})^2}}{i-1} = 2.3 \cdot 10^7, \tag{3.14}$$

where N_i^{sec} is a number of elastic events in a given sector pair, N_{av} is the average for 3 sector pairs. Finally, the method with the largest value of uncertainty is chosen yielding:

$$N_{elastic}^{42^\circ-145^\circ} = (1.59 \pm 0.04) \cdot 10^9 \text{ events.} \tag{3.15}$$

In order to calculate the total elastic scattering inside EDDA acceptance, the measured $p-p$ differential cross sections σ_i are integrated (see Fig. 3.12):

$$\int \frac{d\sigma}{d\Omega} \cdot d\Omega = 2\pi \sum_i \sigma_i \cdot (\cos(\theta_r) - \cos(\theta_l)) = 6.04\, mb, \tag{3.16}$$

where θ_l and θ_r are left and right limits of the θ intervals. The error of the EDDA cross section in the selected method amounts to:

$$\Delta\sigma_{elastic}^{42^o-145^o} = \sqrt{\sum_{i=42}^{145} \sigma_i^2} = 0.37\, mb, \tag{3.17}$$

where σ_i is the uncertainty of the measurement in the EDDA experiment for an i-th bin in polar angle. Finally, the normalization factor for all spectra presented in the following chapter amounts to:

$$\frac{\sigma_{elast}}{N_{elast}} = (3.84 \pm 0.25) \cdot 10^{-12}, \tag{3.18}$$

where the error includes both: the EDDA error (eq. 3.17) and the error of reconstructed elastic events inside the HADES acceptance (eq. 3.15).

3.5 Reaction simulations

In order to compare data collected during experiment with model calculation, the simulation based on PLUTO generator ([55], [34]) has been performed.

The aim of this comparison is to shed more light on the origin of e^+e^- pairs in the reaction $d+p \rightarrow p_{spec}e+e-X$ at $1.25GeV/u$. Reaction channels studied in this simulation are presented in Tab. 3.1 together with cross sections for decaying particle integrated over nucleon momentum distribution inside deuteron and effective branching ratios for dielectron decays integrated over mass of decayed particle. Cross sections include reactions denoted as "⇒" in the table and branching ratio obtained for the decay marked as "→". They can be divided into channels with a proton as a spectator particle (1., 2., 4., 5., 7., 8., 10., 11., 13., 14.) and neutron spectator (3., 6., 9., 12.) or channel with deuteron in the final state (8., 13., 14.).

Table 3.1: The simulated channels, cross sections and branching ratios along with their sources presented in square brackets.

lp.	channel	cr. sect.	br. ratio
1.	$d\,p \Rightarrow\ p_{sp}\,n\,\Delta^+ \ \Rightarrow\ p_{sp}\,n\,p\,\pi^0 \ \rightarrow\ p_{sp}\,n\,p\,\gamma\,e^+\,e^-$	$3.67mb$ [59]	0.012
2.	$d\,p \Rightarrow\ p_{sp}\,p\,\Delta^0 \ \Rightarrow\ p_{sp}\,p\,n\,\pi^0 \ \rightarrow\ p_{sp}\,p\,n\,\gamma\,e^+\,e^-$	$3.67mb$ [59]	0.012
3.	$d\,p \Rightarrow\ n_{sp}\,p\,\Delta^+ \ \Rightarrow\ n_{sp}\,p\,p\,\pi^0 \ \rightarrow\ n_{sp}\,n\,p\,\gamma\,e^+\,e^-$	$3.67mb$ [59]	0.012
4.	$d\,p \Rightarrow\ p_{sp}\,p\,\Delta^0 \ \rightarrow\ p_{sp}\,p\,n\,e^+\,e^-$	$5.54mb$ [59]	$4.82 \cdot 10^{-5}$
5.	$d\,p \Rightarrow\ p_{sp}\,n\,\Delta^+ \ \rightarrow\ p_{sp}\,n\,p\,e^+\,e^-$	$5.54mb$ [59]	$4.93 \cdot 10^{-5}$
6.	$d\,p \Rightarrow\ n_{sp}\,p\,\Delta^+ \ \rightarrow\ n_{sp}\,p\,p\,e^+\,e^-$	$5.54mb$ [59]	$4.94 \cdot 10^{-5}$
7.	$d\,p \Rightarrow\ p_{sp}\,n\,p\,\eta \ \rightarrow\ p_{sp}\,n\,p\,\gamma\,e^+\,e^-$	$13.4\mu b$ [38]	$5.96 \cdot 10^{-3}$
8.	$d\,p \Rightarrow\ p_{sp}\,d\,\eta \ \rightarrow\ p_{sp}\,d\,\gamma\,e^+\,e^-$	$22.8\mu b$ [38]	$6.10 \cdot 10^{-3}$
9.	$d\,p \Rightarrow\ n_{sp}\,p\,p\,\eta \ \rightarrow\ n_{sp}\,p\,p\,\gamma\,e^+\,e^-$	$2.41\mu b$ [38]	$5.64 \cdot 10^{-3}$
10.	$d\,p \Rightarrow\ p_{sp}\,n\,p\,e^+\,e^-$	$1.48\mu b$ [17]	1
11.	$d\,p \Rightarrow\ p_{sp}\,p\,N^0(1520) \Rightarrow\ p_{sp}\,p\,n\,\rho \ \rightarrow\ p_{sp}\,p\,n\,e^+\,e^-$	$8.91\mu b$ [63]	$8.12 \cdot 10^{-4}$
12.	$d\,p \Rightarrow\ n_{sp}\,p\,N^+(1520) \Rightarrow\ n_{sp}\,p\,p\,\rho \ \rightarrow\ n_{sp}\,p\,p\,e^+\,e^-$	$8.91\mu b$ [63]	$8.12 \cdot 10^{-4}$
13.	$d\,p \Rightarrow\ p_{sp}\,d\,\rho \ \rightarrow\ p_{sp}\,d\,e^+\,e^-$	$6.40\mu b$ [63]	$8.12 \cdot 10^{-4}$
14.	$d\,p \Rightarrow\ p_{sp}\,d\,\gamma^* \ \Rightarrow\ p_{sp}\,d\,e^+\,e^-$	$41.7nb$ [60]	1

All these channels can also be grouped into reactions with $\pi^0 \rightarrow e^+e^-\gamma$ (1.,2.,3.), $\Delta \rightarrow Ne^+e^-$ (4.,5.,6.), $\eta \rightarrow e^+e^-\gamma$ (7.,8.,9.), $N - N$ bremsstrahlung (10.) and $\rho \rightarrow e^+e^-$ decays (11., 12., 13. and 14.).

The dominant channel is a π^0 meson production and its Dalitz decay into $e^+e^-\gamma$. π^0 can be produced in two ways: either directly in nucleon-nucleon collisions or by the decay of baryonic resonances. According to resonance model, used in the simulations, the first case is negligible at our energy [59]. The second scenario proceeds via excitation of a nucleon to the Δ or N^* baryonic resonances state during the reaction. After that, the resonance decays either to a nucleon and a π^0 or directly to a nucleon and e^+e^-. A parametrization of the total cross section for the one-pion production in $p+n$ reactions as a function of the center of mass energy is presented in Fig. 3.16 together with available data points. From

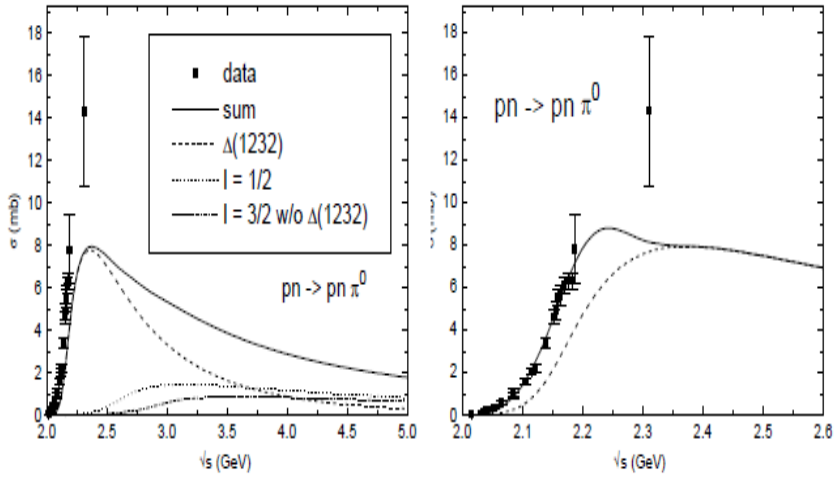

Figure 3.16: Left: one-pion production cross sections (solid line) for different isospin channels in the function of available energy [59]; contributions from the $\Delta(1232)$ (dashed); the isospin 1/2 resonances (dotted); the higher isospin 3/2 resonances (dashed dotted) according to resonance model [59]. Right: $pn \rightarrow pn\pi^0$ production cross section taking into account only the contributions due to decay of baryonic resonances (dashed line) and total cross sections obtained by adding the direct pion production in nucleon-nucleon collisions (solid line) in comparison to experimental data.

this parametrization one can read that the total cross section for π^0 production is 8 mb at our beam energy and is dominated by Δ formation. The other, heavier baryonic resonances play a minor role.

Figure 3.17 presents angular distributions of resonance in the $n+p \rightarrow N+\Delta$ production and $n + p \rightarrow N + N^0(1520)$ in $n + p$ center of mass frame. In both cases their shape is symmetric with respect to zero with prominent forward-backward asymmetry (in particular for Δ particle) indicating peripheral character of the production [12], [56].

As mentioned above the $\Delta(1232)$ can also directly decay to the e^+e^- pair and nucleon in Dalitz decay $\Delta \rightarrow Ne^+e^-$ with branching ratio (BR) at resonance pole $4 \cdot 10^{-5}$. The respective mass dependant branching ratio BR(M) for this decay has been given by [58]

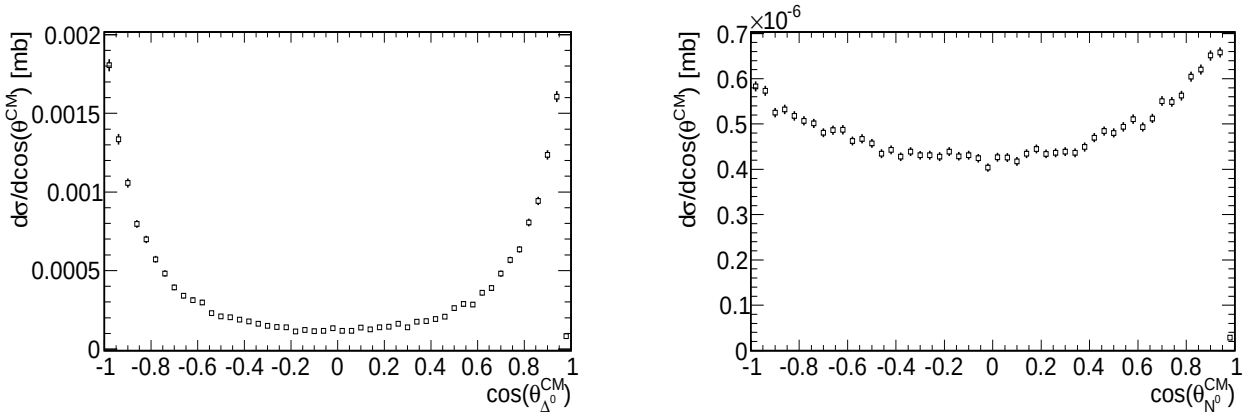

Figure 3.17: Angular Θ distribution of resonans particle for $d\,p \rightarrow\ p_{sp}\,n\,\Delta^{+}$ (left) and $d\,p \rightarrow\ p_{sp}\,p\,N^{0}(1520)$ (right).

and implemented in PLUTO simulations [55]. This contribution will be called as "model A" in the text.

Yet, another important contribution to the dilepton spectra originates from the nucleon-nucleon bremsstrahlung channel discussed in the introduction chapter. The cross section of this channel has not been measured and was implemented in the simulations according to Kaptari and Kaempfer calculation [17]. It assumes a coherent sum of nucleon and Δ contributions. One should note that in this approach Δ excitation and its Dalitz decay is coherently added to the "quasi-elastic" part and will be presented as a sum referenced in text as "bremsstrahlung" or "model B" in the text.

Besides π^0 also η meson can be created in $d + p$ reaction at $1.25AGeV$. Since $E_{kin} = 1.25GeV$ is the kinetic energy which corresponds exactly to the η meson production threshold in free $N - N$ collisions this can only happen when Fermi momentum of nucleon is opposite to the momentum of the beam. As it is known from former experiments, the η production proceeds mainly via the excitation of $N^{*}(1535)$ which subsequently decays into the nucleon-η channel. The cross sections for the respective channels $p + n\ \rightarrow\ d\,\eta$, $p + n\ \rightarrow\ p\,n\,\eta$, $p + p\ \rightarrow\ p\,p\,\eta$ are known from WASA measurements - H. Calen work [38] and COSY11 [57] and are presented in the Fig. 3.18 together with parametrization used in

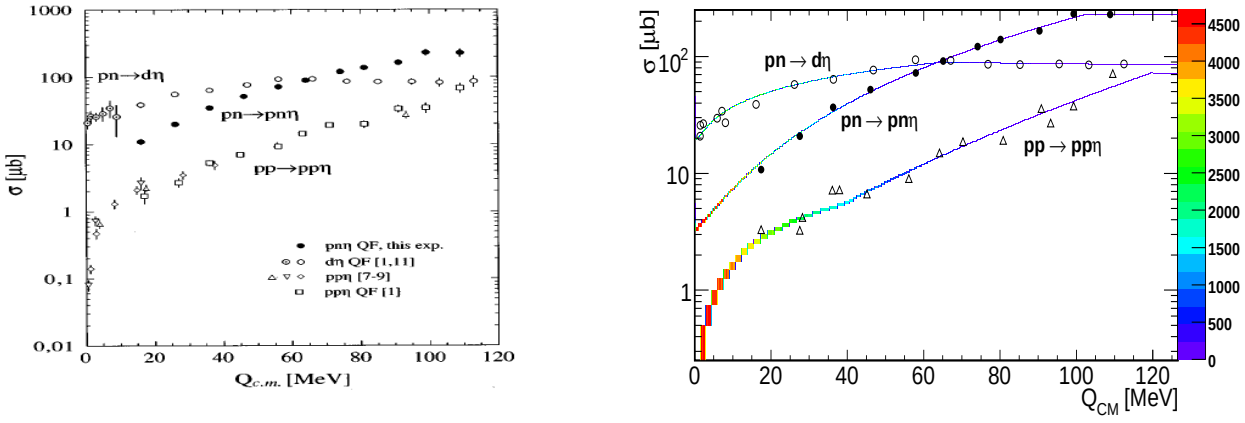

Figure 3.18: Left: total cross section for the η meson production as a function of the excess energy in c.m. system: $p+n \rightarrow d\eta$ (open circles); $p+n \rightarrow np\eta$ (solid points); $p+p \rightarrow pp\eta$ (open squares) [38]. Right: fits to the experimental data, where colors show abundance of events at the given energy.

the simulation. It turns out that at our beam energy most of the events with η production (90%) has the energy excess defined as $Q_{CM} = \sqrt{s} - 2m_p - m_\eta$, smaller then $50MeV$.

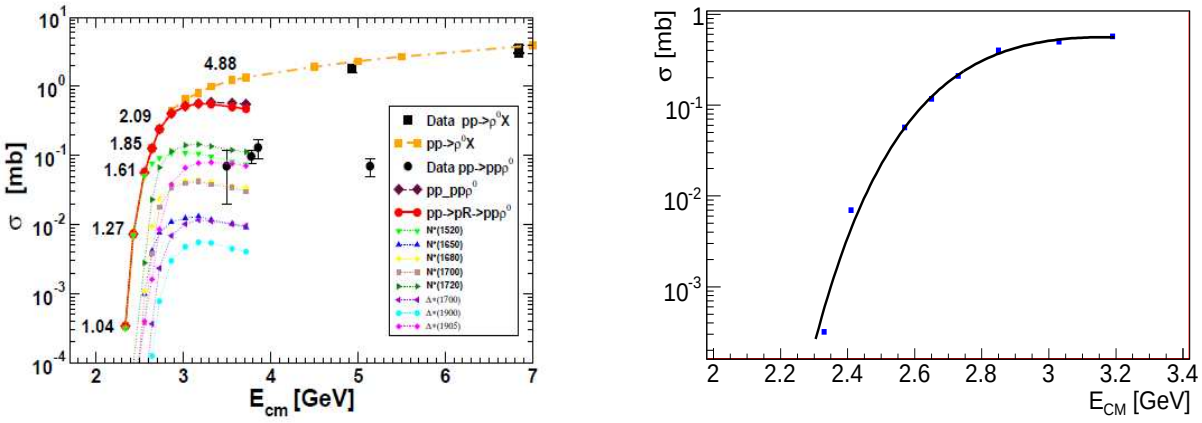

Figure 3.19: Left: The calculations [64] of cross sections (color lines) for ρ^0 meson production in $p+p$ collisions for inclusive ($p+p \rightarrow \rho^0 X$) and exclusive ($p+p \rightarrow pp\rho^0$) channels in comparison to experimental data (black marks) [63]. Right: fit to calculation of the channel $pp \rightarrow pR \rightarrow pp\rho^0$.

The last source considered in simulation of the dilepton pairs is "subthreshold" ρ production. This channel is simulated in three ways. The standard method used in the previous publication [67] is a decay of $N(1520)$ in $pn \rightarrow N(1520)N \rightarrow pn\rho$ collisions. Note that due to large ρ meson width $\Gamma_\rho = 150MeV$ such hypothetical production can take place. Resonance production via $N(1520)$ has been assumed since it is known that this resonance has a large branching ratio for ρ and can provide another contribution to dilepton production. The cross section for this process is unknown and is adopted from theoretical calculation [64]. It is important to remember that the ρ cross sections predicted in [64] concern only the $p + p$ collision. However, the simulation covers also $d + p \rightarrow p_{spec}d\rho$ channel (13. in 3.1), where the corresponding cross section function (from 3.19) was assumed identical to the one for the channel including $N(1520)$. The difference in the integrated cross section shown in table 3.1 (and in Fig. 3.20) results from different range of access energy for particle production in both cases. The last "ρ-like" contribution $dp \rightarrow dp\gamma^*$ (14. in 3.1) is inspired by calculations of Martemyanov, Krivoruchenko in spirit of Vector Meson Dominance (VMD) for inverse reaction to deuterium photo-desintegration [60].

The resulting simulated e^+e^- differential cross section as a function of the dielectron invariant mass distribution inside the HADES acceptance is shown in Fig. 3.20, where individual components are marked by lines of different colors.

The three methods of ρ production are alternative and only one of them can be chosen to contribute to a total e^+e^- distributions to avoid double counting. In the same manner bremsstrahlung and Δ channels should be considered.

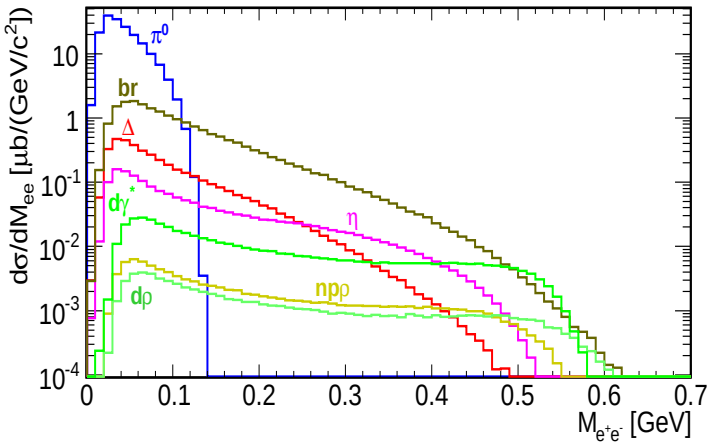

Figure 3.20: The invariant mass distribution of e^+e^- for the $dp \rightarrow p_{spec}e^+e^-X$ reaction at $1.25AGeV$ in HADES acceptance. Colors represents following contributions: π^0 (blue), bremsstrahlung (brown), η (pink), Δ (red), ρ through radiative capture (green), ρ with deuteron channel (pale green) and ρ channel via $N(1520)$ (yellow).

3.6 Selection of proton spectator

Description of the selection of reaction where the proton is a spectator particle is a main subject of this chapter. During the $d+p$ experiment the Forward Wall was installed into the HADES setup in order to detect the spectator proton, thus to tag the quasi-free $p+n$ reaction and to separate them from the $p+p$ channel. Spectator selection was realized by condition on a momentum of particle detected in the Forward Wall to be in the range from $1.6GeV/c$ to $2.6GeV/c$. The momentum window takes into account FW resolution resulting from the time of flight measurement. To verify this condition I have made dedicated simulations with following channels:

1. $d\,p \rightarrow p_s\,n\,\Delta^+ \rightarrow p_s\,n\,p\,dilepton \rightarrow p_s\,n\,p\,e^+\,e^-$.
2. $d\,p \rightarrow p\,n_s\,\Delta^+ \rightarrow p\,n_s\,p\,dilepton \rightarrow p\,n_s\,p\,e^+\,e^-$.
3. $d\,p \rightarrow d\,\Delta^+ \rightarrow d\,p\,dilepton \rightarrow d\,p\,e^+\,e^-$.

where subscript s denotes spectator particle.

The resulting e^+e^- invariant mass distributions for pairs with opening angle $\alpha_{e^+e^-} > 9°$ inside HADES acceptance, with an additional condition for the spectator proton, defined as particle hit in the region of FW acceptance with the momentum between $1.6GeV/c$ and $2.6GeV/c$ are shown in Fig. 3.21. The reduction rate of particular channels due to the proton spectator condition is shown in Fig. 3.22. One can see that the applied spectator condition is very efficient in discrimination against $pn_spe^+e^-$ and dpe^+e^- channels (for the $M_{e^+e^-} > m_{\pi^\circ}$ purity is 96%).

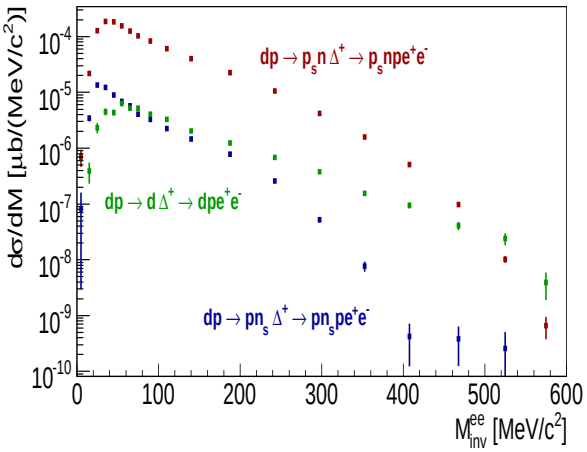

Figure 3.21: Invariant mass distribution of e^+e^- in HADES acceptance with spectator conditions and $\alpha_{e^+e^-} > 9°$ (see text). Types of channels are shown in the picture.

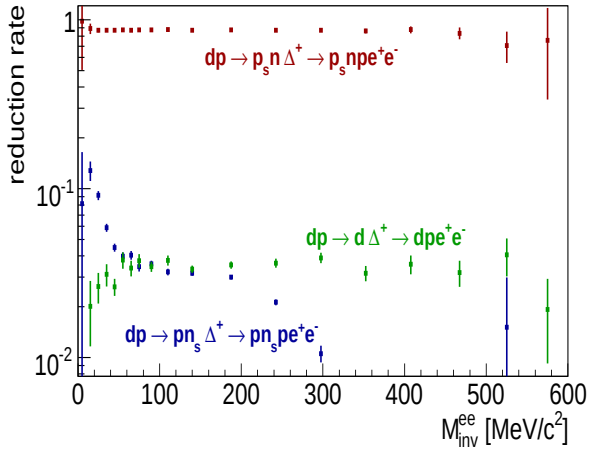

Figure 3.22: Reduction rate of survived di-electron pairs after additional spectator condition as a function of e^+e^- invariant mass for various reaction channels.

In more details, reduction rates are the following: channel with p_s loses 11% of statistics but 95% is lost for channel with n_s and 97% in the case of absence of spectator ("coherent" production).

Furthermore, channels with $\rho \rightarrow e^+e^-$ production were studied with respect to the acceptance for the detection of the spectator proton. Following channels have been generated:

1. $d\,p \rightarrow p_s\,p\,N^0_{1520} \rightarrow p_s\,p\,n\,\rho \rightarrow p_s\,p\,n\,e^+\,e^-$.

2. $d\,p \rightarrow p_s\,n\,N^+_{1520} \rightarrow p_s\,n\,p\,\rho \rightarrow p_s\,n\,p\,e^+\,e^-$.

3. $d\,p \rightarrow p\,n_s\,N^+_{1520} \rightarrow p\,n_s\,p\,\rho \rightarrow p\,n_s\,p\,e^+\,e^-$.

4. $d\,p \rightarrow d\,N^+_{1520} \rightarrow d\,p\,\rho \rightarrow d\,p\,e^+\,e^-$.

5. $d\,p \rightarrow p\,n\,N^+_{1520} \rightarrow p\,n\,p\,\rho \rightarrow p\,n\,p\,e^+\,e^-$ (no spectator emission).

Also for these reactions a strong decrease of number of events is noticeable when no proton spectator is detected in FW (Fig. 3.23 and 3.24). The survival rates for channels are: 72%, 82%, 0.2%, 3.6%, 6.6%, respectively.

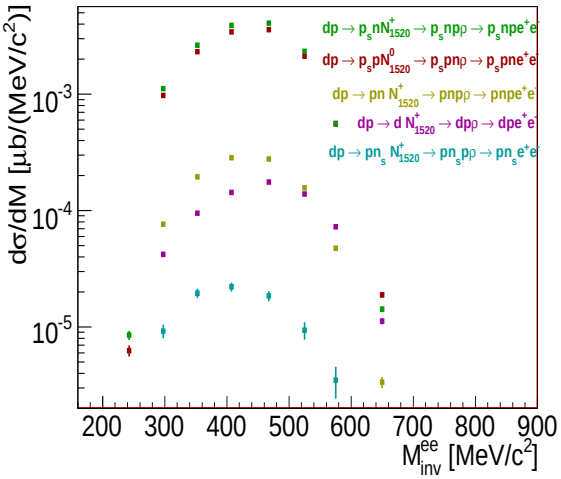

Figure 3.23: e^+e^- invariant mass distributions in HADES acceptance with the spectator condition and the e^+e^- opening angle $\alpha_{e^+e^-} > 9°$ for various reactions.

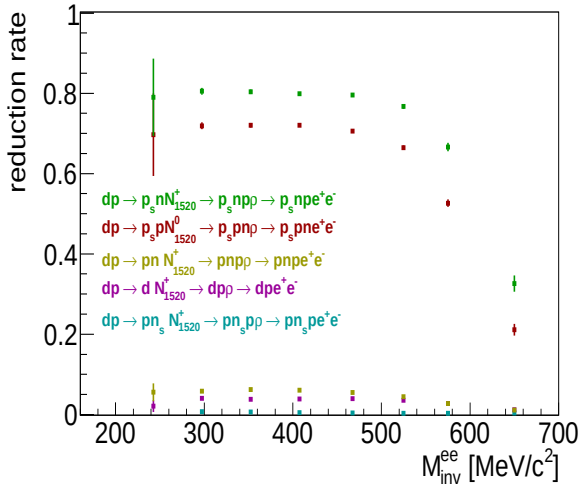

Figure 3.24: Rate of survived dielectron pairs after additional spectator condition as a function of the e^+e^- invariant mass for various reactions.

The application of the spectator condition induces also some reduction for the reactions of interest because of finite acceptance of the FW detector. The result of the simulation shows that FW acceptance amounts to at least 84% for the reactions of the type $d + p \rightarrow p_{spec}e^+e^-$.

Next, experimental distributions for the spectator hits registered in FW will be shown and compared to the simulations assuming spectator model. In Fig. 3.25 and 3.26 the presented spectra are normalized to the same area in order to compare their shape.

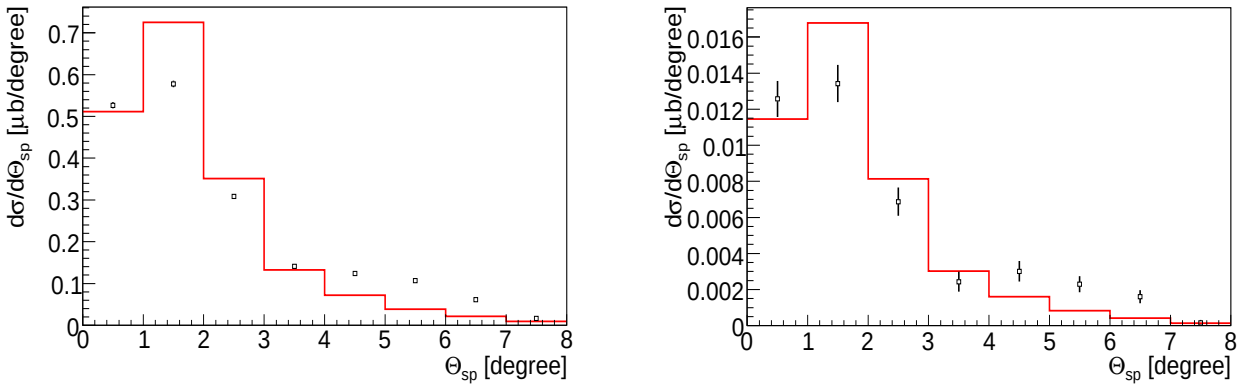

Figure 3.25: The experimental (black) and simulated (red) differential cross section in the function of polar angle for two regions of e^+e^- invariant mass: $M^{ee}_{inv} < M_\pi$ (left) and $M^{ee}_{inv} > M_\pi$ (right).

Fig. 3.25 shows polar angle distributions of the spectator proton measured in the FW for two e^+e^- invariant mass region: $m_{e^+e^-} < M_\pi$ (left) and $m_{e^+e^-} > M_\pi$ (right). Fig. 3.26 shows the experimental and simulated momentum distributions of spectator for various θ angles.

As one can see the spectator model gives reasonable description of the measured angular distributions up to $\theta = 4°$.

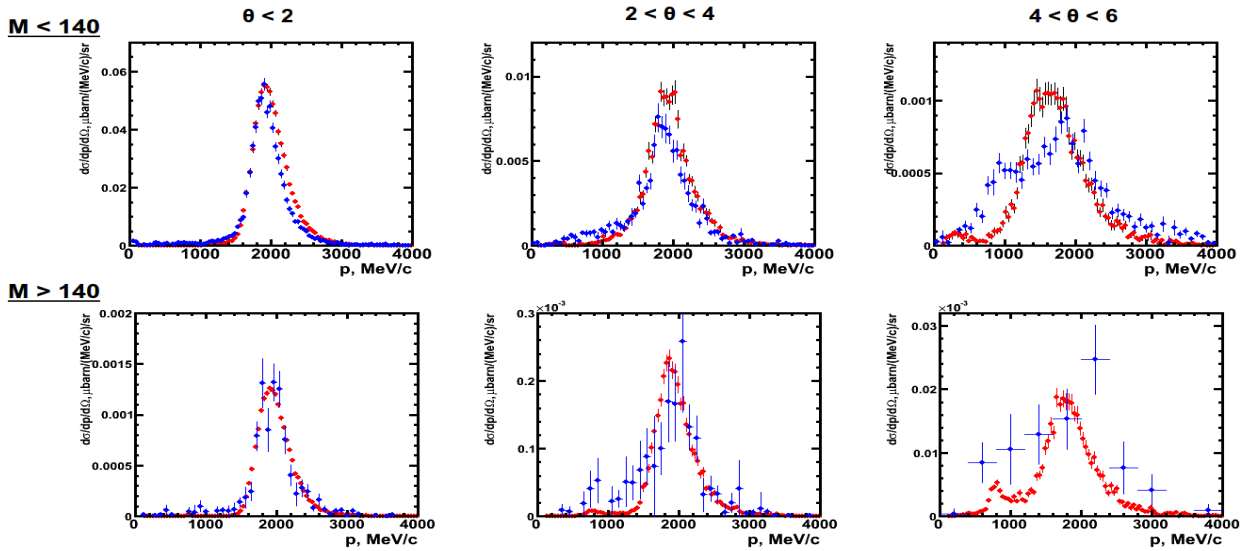

Figure 3.26: The proton spectator momentum distributions for θ angle slices (2, 4, 6 degree) and two mass regions ($m_{e^+e^-} < M_\pi$ and $m_{e^+e^-} > M_\pi$) [65].

3.7 Comparison of experiment results with model calculations

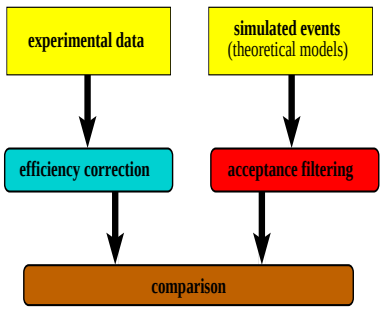

Figure 3.27: Schematics of comparison method of experimental data with theory.

Fig. 3.27 shows the procedure that was used to compare experiment with the simulation. On one side experimental distributions are corrected for efficiency, event by event, on the other simulation events are filtered with the HADES acceptance. Respective efficiency and acceptance matrices have been introduced in section 3.3.2. Normalization of

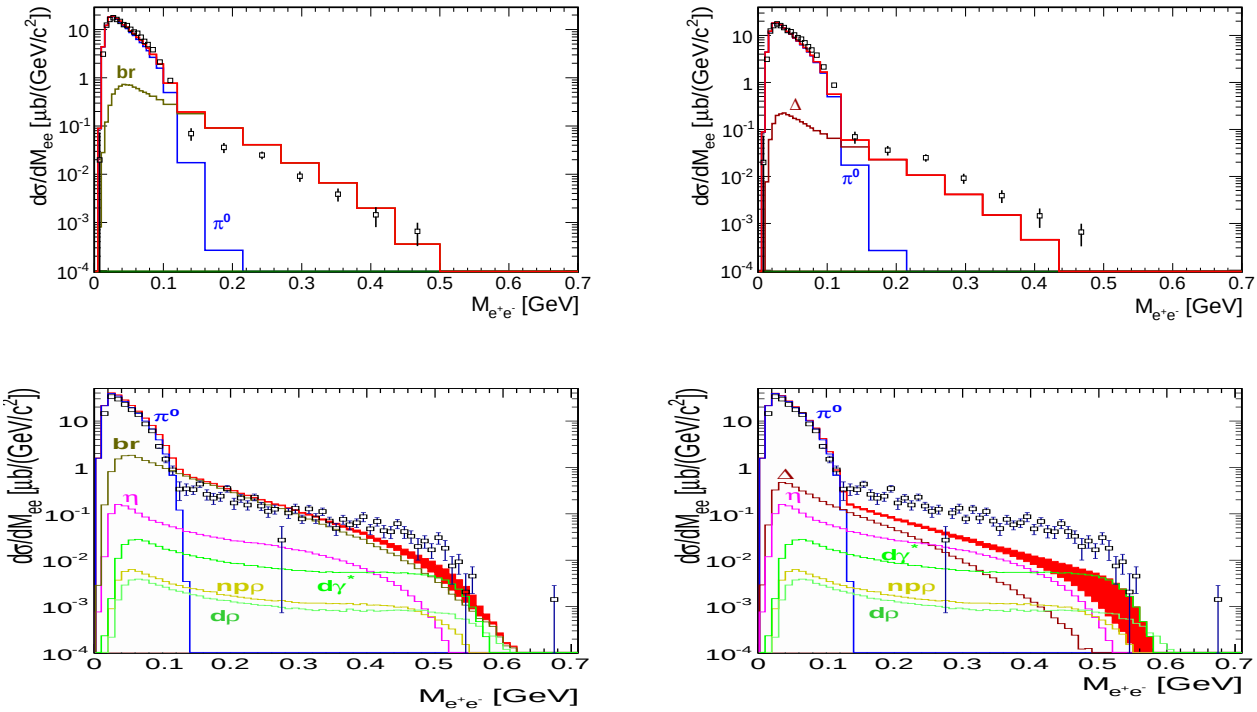

Figure 3.28: Invariant mass distribution of e^+e^- for $p+p$ (up) and $d+p$ (down) reaction at $1.25 AGeV$. Black squares represent experimental data and red line - sum of the contributions: π^0 (blue), Δ (dark red), bremsstrahlung (brown), η (pink), ρ channels (yellow and green). Down left hand side distribution contains bremsstrahlung and right hand side Δ channel.

the experimental distributions is provided by elastic scattering as explained in section 3.4. Simulation is normalized to the absolute cross sections.

Fig. 3.28, as a first example, shows inclusive e^+e^- invariant mass distribution for $p+p$ and $d+p$ collisions. The experimental distributions are compared with PLUTO simulations. Various e^+e^- contributions are shown using separate histograms: π^0 (blue), Δ channel - model "A", NN bremsstrahlung - model "B" (brown), η Dalitz decay (pink) and ρ contribution (yellow). A red hatched area shows a range spanned by the two extreme assumptions about ρ production:

- ρ coming from $N^0(1520)$ decay (11. in the table 3.1),

- $d\gamma^*$ channel (13. in the same table).

Experimental data are plotted with statistical errors only. Systematical errors related to normalization and efficiency correction amounts to 15% and have only weak mass dependence (see appendix B and Fig. B.6).

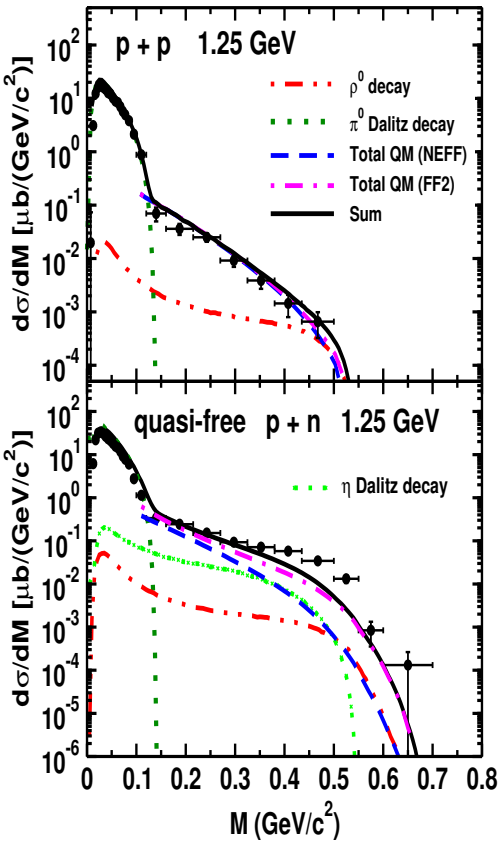

Figure 3.29: Invariant mass distribution of the dileptons produced in the $p+p$ (upper panel) and quasifree $n+p$ (lower panel) reactions at $1.25 AGeV$. The black points represent HADES data. Coloured lines show the various contribution from the new Shyam, Mosel calculation (described in the legend) [30].

For comparison in Fig. 3.29 one can see the same experimental data with the newest predictions of Shyam, Mosel model (described in chapter 1.1). As it can be seen, the decisive

ingredient improving agreement with the data is inclusion of the pion electromagnetic form-factor.

Revert to Fig. 3.28 there is a good agreement between data and both models in the π^0 region. However, in the model including model "A" instead of model "B" a significant deficit of dilepton pairs appears for $M_{inv}^{ee} > M_{\pi^0}$ (Fig. 3.29, right). On the other hand, the model "B" describes $n + p$ data better (but still is not able to reproduce the high mass part of the spectrum) but clearly overestimate $p + p$ data for $M_{inv}^{ee} > M_{\pi^0}$.

3.8 γ^* distributions

In this chapter differential distributions of inclusive virtual photons are presented and compared to model predictions. The components included in the simulated distributions have been introduced in previous section and shown in Fig. 3.28 (bottom, left panel) with one condition. From all ρ channels only $\rho \rightarrow npe^+e^-$ is shown. Two another have different magnitude but similar shape which is the most important feature in two following section. For the bremsstrahlung component Kaptari model will be used in the following section.

The approach of comparison of all spectra will be common. The experimental data have been corrected for efficiency and simulations have been filtered with the acceptance filter as presented in Fig. 3.27. Then simulation distributions have been normalized to the model cross section described in the section 3.5 and experimental spectra according to the procedure shown in the section 3.4.

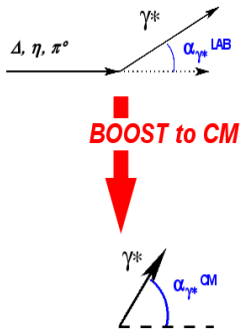

Figure 3.30: The visualization for calculating $\theta^{CM}_{\gamma^*}$ angle.

Systematic errors of normalization and efficiency correction are not shown. They are considered as constant and equal to 15%.

First, distribution of the dilepton (γ^*) polar angle in the center of mass (CM) frame is discussed. This angle characterizes production of the virtual photon. $\theta^{CM}_{\gamma^*}$ is the polar angle between γ^* momentum vector boosted to the CM frame and z-axis of CM (as shown in Fig. 3.30).

Left column of Fig. 3.33 presents the experimental distributions of $\cos(\theta^{CM}_{\gamma^*})$ (black

symbols) compared to the model (colored points) in the HADES acceptance. CB has been subtracted from the signal and the spectrum has been corrected for the efficiency. On the other side simulation has been filtered for acceptance and divided into channels.

This procedure was applied separately for three mass region: $M^{ee}_{inv} < M_{\pi^0}$, $140MeV < M^{ee}_{inv} < 280MeV$, and $M^{ee}_{inv} > 280MeV$ and the result is shown in the left column in Fig. 3.33.

In the next step, acceptance corrected distributions were calculated. In order to obtain these distributions the acceptance correction factors have to be obtained. They are given as the ratio between two simulated spectra, shown in Fig. 3.31, in the HADES acceptance and the full solid angle. Black symbols presents distribution of $\cos(\theta^{CM}_{\gamma^*})$ in full solid angle obtained in simulations. Observed slight anisotropy of virtual photon emission is a consequence of anisotropic Δ production (see Fig. 3.17). The blue symbols show simulation data filtered with the HADES acceptance (same spectra as in Fig. 3.33).

The obtained ratio is shown in Fig. 3.32. It is important to mention that correction may depend on the applied model. Furthermore, as one can see, the correction factor depends strongly on the angle. In order to reduce too large extrapolation factors one applies corrections only to the region where acceptance is large: (-0.4; 0.45).

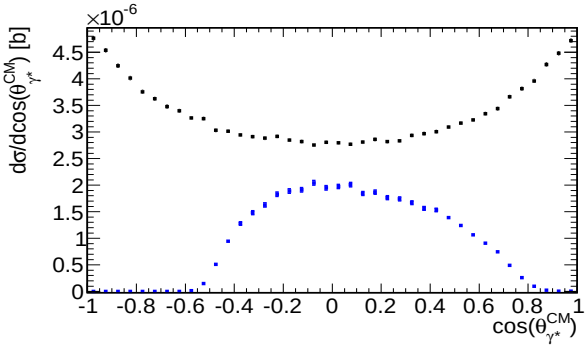

Figure 3.31: The simulated $\cos(\theta^{CM}_{\gamma^*})$ distribution for $M^{e^+e^-}_{inv} < 140MeV$ in full solid angle (black) and inside HADES acceptance (blue).

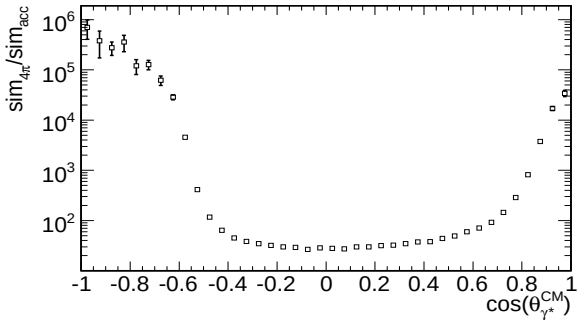

Figure 3.32: The acceptance correction for $\cos(\theta^{CM}_{\gamma^*})$ for $M^{e^+e^-}_{inv} < 140MeV$.

After application of this correction to the spectra in the HADES acceptance the comparison in full solid angle was obtained for three mass region and is shown in right column in Fig. 3.33.

Concluding from above comparison one can say that in the mass region below $150MeV/c^2$ there is a reasonable consistency between the model and the data.

It is worth noticing the cross section obtained in experiment for π^0 channel equals $6.03mb$, instead of assumed $7.34mb$ in simulated model [59].

For higher mass region: $150MeV/c^2 < M_{inv}^{e^+e^-} < 280MeV/c^2$ and $M_{inv}^{e^+e^-} > 280MeV/c^2$ the experimental spectra have a similar shape to that one assumed in the simulation, i.e. supporting isotropic emission but differ, as already seen in the invariant mass distributions, in absolute scale. However, one should emphasize that such emission was assumed because of the lack of more detailed prescription given in the work of Kaptari, Kampfer [17].

In the next paragraph e^+e^- rapidity distributions are discussed. Rapidity is defined in terms of the momentum by the Eq. 3.19.

$$y = \frac{1}{2} \cdot \ln(\frac{E + p_{||}c}{E - p_{||}c}). \tag{3.19}$$

Fig. 3.34 shows γ^* rapidity distributions efficiency and acceptance corrected (black symbols) compared to simulation (colored symbols) for three regions of $M_{e^+e^-}$.

One can see there is a good agreement in the shape of presented spectra for mass region of M_{π^0} and between $140MeV$ and $280MeV$. Only for the mass larger than $280MeV$ the dilepton excess is visible in the limited range of mid-rapidity, namely from 0.4 to 1.0.

The last investigated distribution is the transverse momentum of virtual photon p_T. It is the perpendicular component of the momentum (shown as $|\overrightarrow{p}|$ in Fig. 3.35).

The p_T spectra shown in Fig. 3.8 indicate quite good agreement between applied model and the experimental data in π^0 mass region.

In the mass region larger than $140MeV$, where breamsstrahlung plays the dominant role, the difference is quite significant. The experimental signal has the peak around $75MeV/c$, whereas in the model it is $325MeV/c$ indicating much softer production mech-

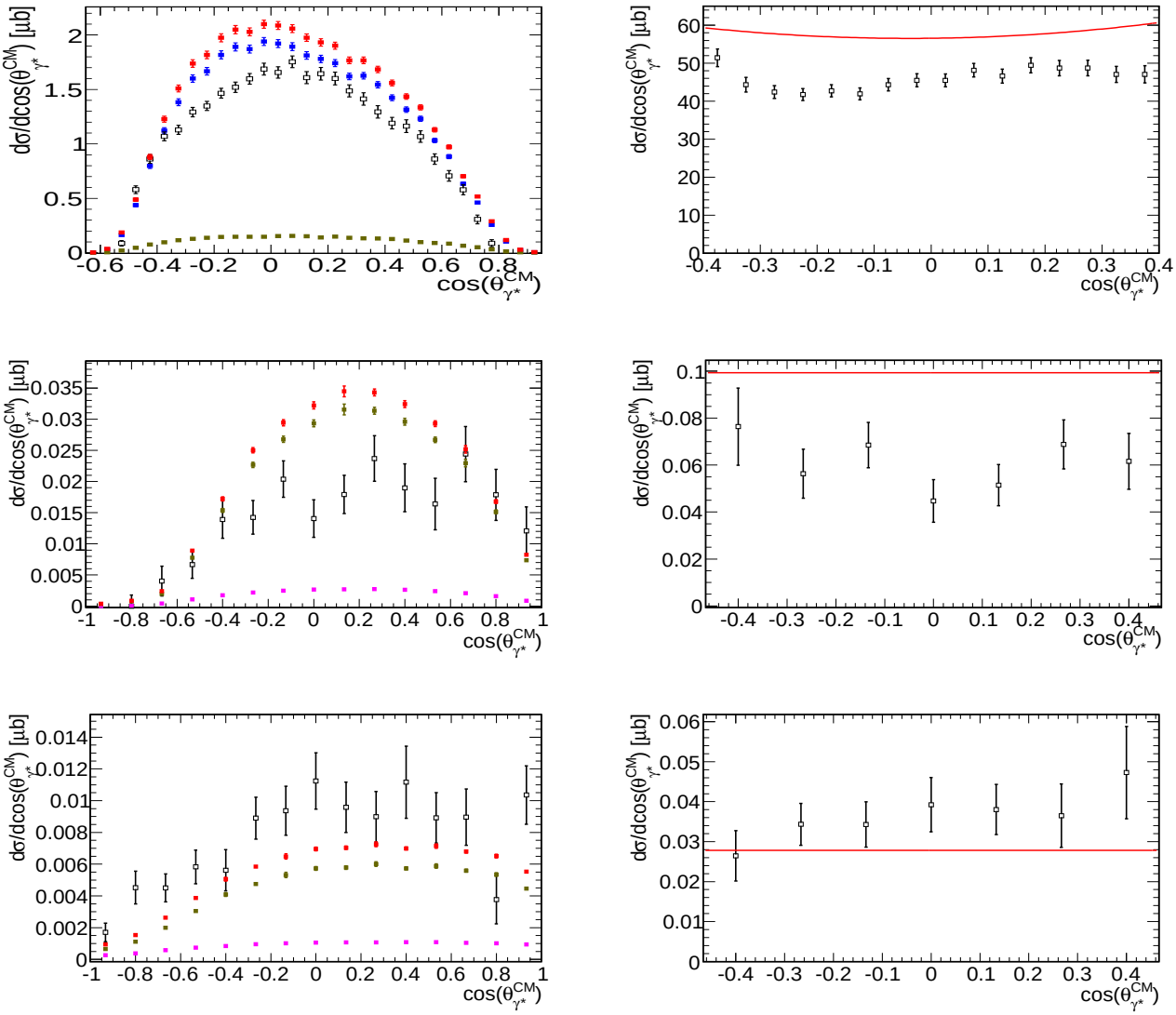

Figure 3.33: The comparison of $\cos(\theta^{CM}_{\gamma^*})$ for simulated (blue - π, brown - bremsstrahlung, pink - η, yellow - ρ, red - total) and experimental data (black points) in the HADES acceptance (l.h.s.) and acceptance corrected (r.h.s., where total simulation spectra is fitted with the red line) for different masses. First row: $M^{e^+e^-}_{inv} < 150 MeV/c^2$; second: $150 MeV/c^2 < M^{e^+e^-}_{inv} < 280 MeV/c^2$; last row: $M^{e^+e^-}_{inv} > 280 MeV/c^2$.

anism.

The shape of the measured transverse momentum distribution for $M^{ee}_{inv} > 280 MeV/c$

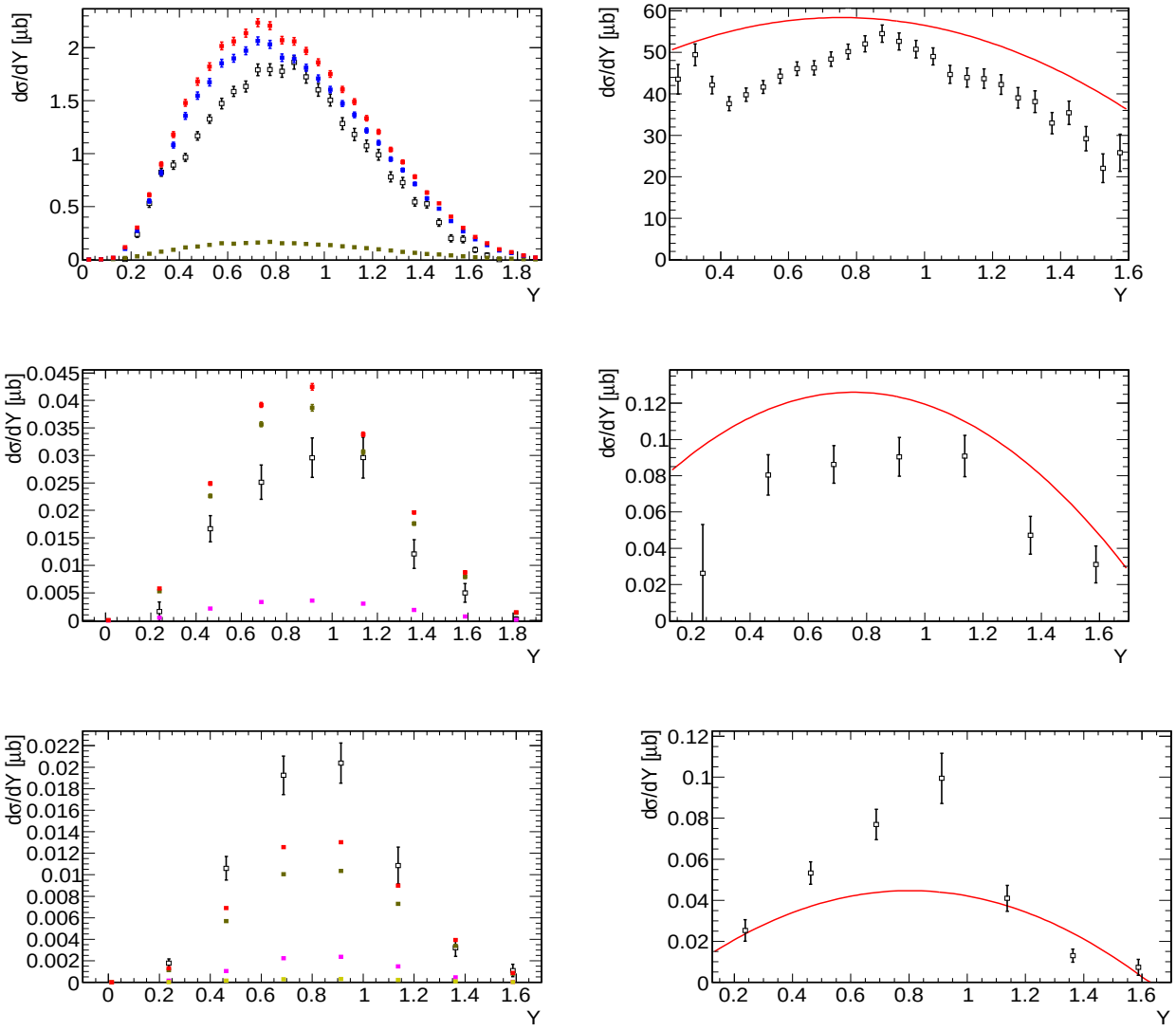

Figure 3.34: The comparison of rapidity. Description is the same as in Fig. 3.33.

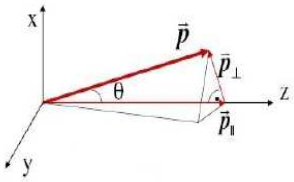

Figure 3.35: Definition of the transverse momentum.

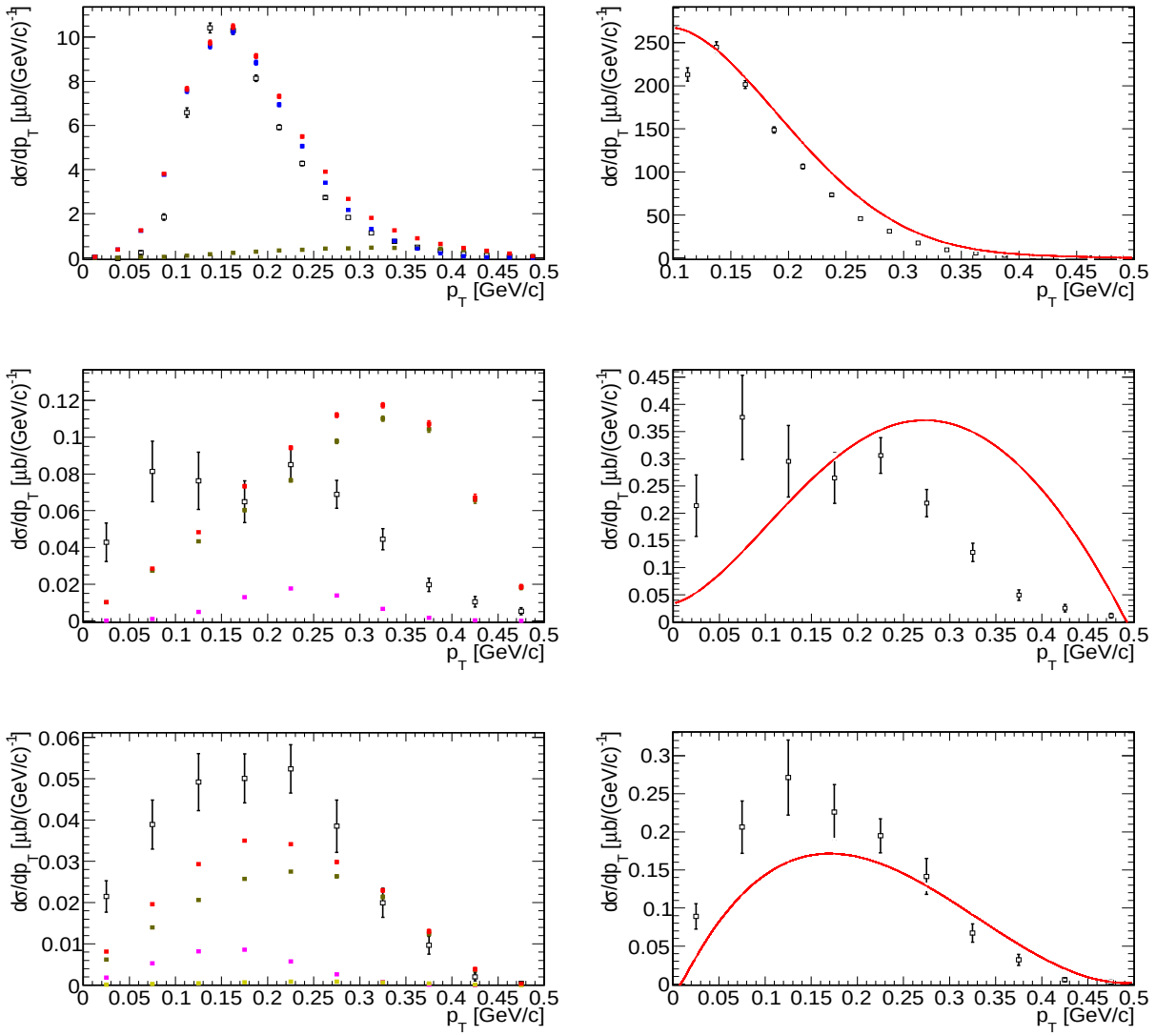

Figure 3.36: The comparison of transverse momentum. Description is the same as in Fig. 3.33.

looks more similar to the simulation, however also with a mean value shifted to lower values.

Summarizing this chapter, assumed model fits in shape and absolute size quite good to the experimental data for the π^0 Dalitz mass region. For larger dilepton masses dis-

agreement between model and the data is larger, in particular striking in the transverse momentum distributions. This is perhaps not a surprise since assumed model was simplified (i.e. isotropic emission) and already was not able to describe invariant mass distributions.

3.9 Comparison of pn with CC at $1AGeV$ data

In this chapter a comparison between three experimental data sets is performed:

1. $d + p$ at $1.25AGeV$.

2. $p + p$ at $1.25GeV$ (experiment done in 2006).

3. $^{12}C + ^{12}C$ at $1AGeV$ (experiment done in 2004).

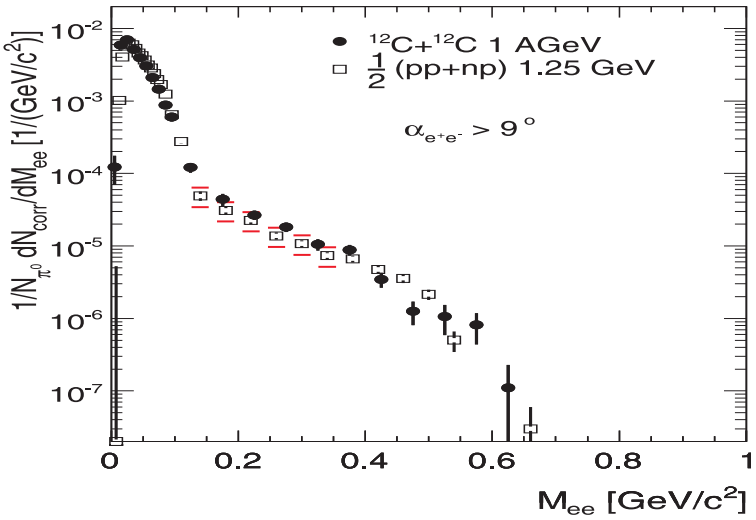

Figure 3.37: Invariant mass spectra for $C + C$ collisions compared with the spectra of the sum of $n + p$ and $p + p$ reactions [67].

The purpose of this comparison is to explore whether the nucleus-nucleus reaction can be considered as a simple superposition of the N-N collision. Indeed, such superposition can be constructed from the measured $p + p$ and $n + p$ reactions and assuming that dielectron production in $n + n$ reactions, not measured by HADES, is the same as in $p + p$ channel. First evidence for such hypothesis is shown in Fig. 3.37, where the e^+e^- invariant mass distribution obtained from the averaged $p+p$ and $n+p$ is compared to $C+C$. To be consistent, elementary reaction spectra were normalized to reconstructed number of π^0 mesons. Both distributions agree within error bars, despite the fact that they are measured with

slightly different beam energies which is, to first order, compensated by the normalization to the pion yield.

Polar angle, rapidity and p_T distributions of γ^* obtained in NN ($np + pp$) with CC in the HADES acceptance region will be discussed now.

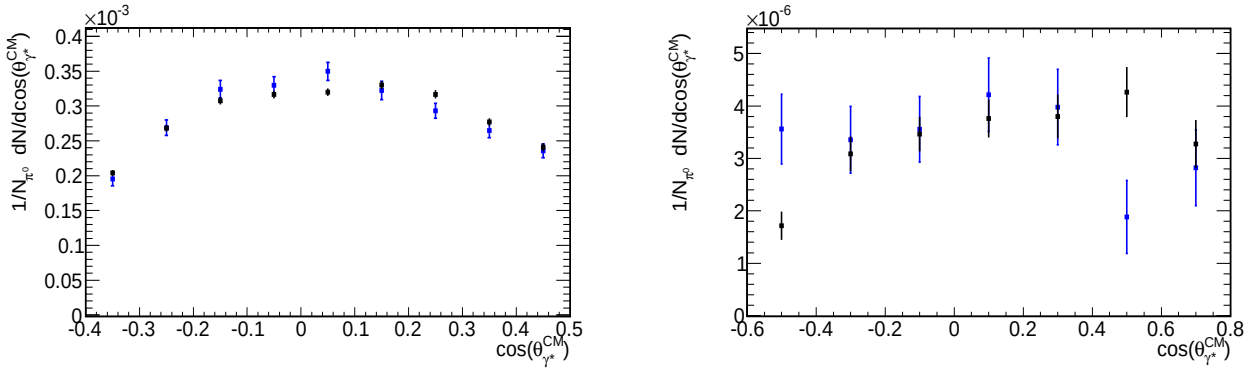

Figure 3.38: Comparison of γ^* angular distribution in the center of mass frame for the experimental data of $C + C$ at $1GeV$ (blue) and N-N at $1.25GeV$ (black) in the HADES acceptance for $M_{inv}^{e^+e^-} < M_{\pi^0}$ (left) $M_{inv}^{e^+e^-} > M_{\pi^0}$ (right).

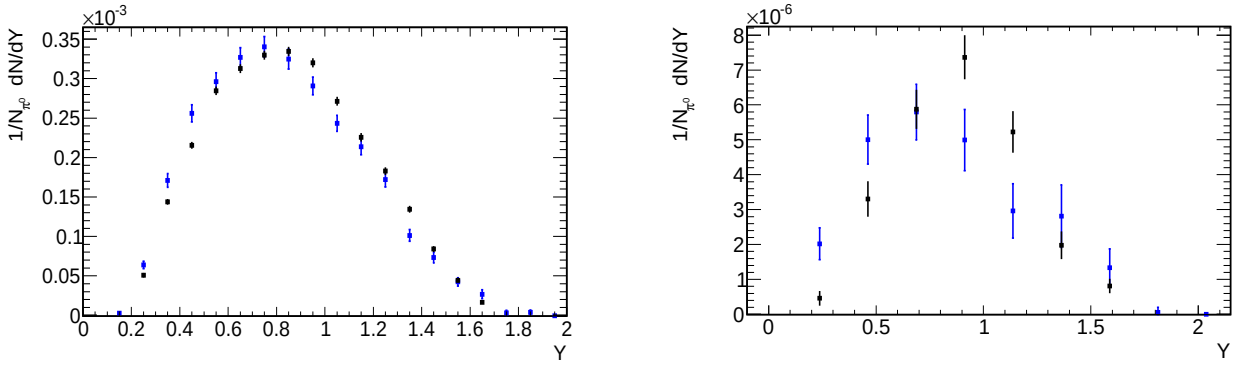

Figure 3.39: Comparison of rapidity for experimental data of $C + C$ at $1GeV$ (blue) and N-N at $1.25GeV$ (black) in the HADES acceptance for both mass regions.

Figs. 3.38, 3.39 and 3.40 show $\cos(\theta_{\gamma^*}^{CM})$, rapidity and transverse momentum distribution for the $C + C$ (blue) and N-N (black) collisions. Three data sets are divided into two mass regions: $M_{inv}^{e^+e^-} < M_{\pi^0}$ (left figures) and $M_{inv}^{e^+e^-} > M_{\pi^0}$ (right figures).

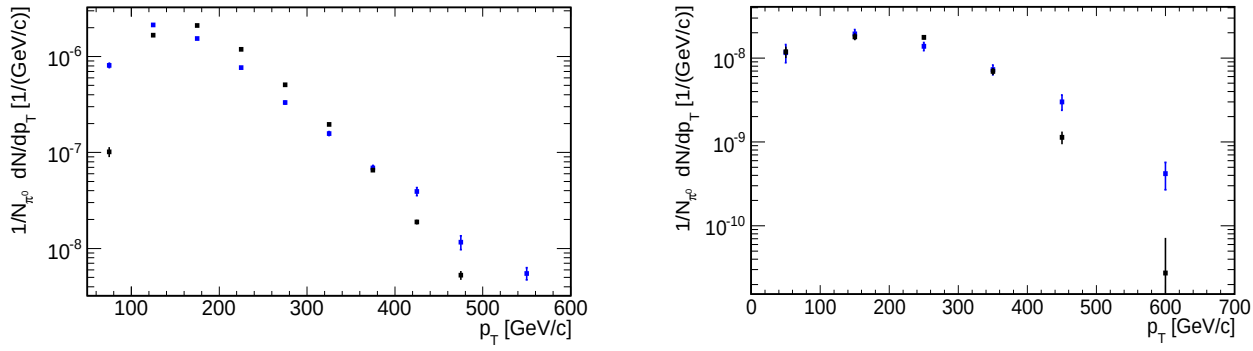

Figure 3.40: Comparison of transverse momentum for experimental data of $C+C$ at $1GeV$ (blue) and $d+p$ at $1.25GeV$ (black) in the HADES acceptance for both mass regions.

The sum of elementary collisions in the case of $\cos(\theta_{\gamma^*}^{CM})$ distribution is consistent with CC reaction. For the two next distributions, rapidity and p_T the maximum of each distribution is slightly shifted to the smaller values. But there still is no new dramatic effect with the changing the collision system to $C+C$.

3.10 Exclusive $pn \rightarrow pne^+e^-$ channel reconstruction

More insight into origin of e^+e^- excess observed in $d+p$ reactions can be provided by studying exclusive channels. In this chapter analysis of exclusive channels tagged by proton spectator and another charge particle hit in the FW will be presented. Main channels which are expected to contribute, due to close to threshold kinematics, are heavy meson (η and ρ) production. This can be seen from the distribution of polar angle of non-spectator proton shown in Fig. 3.41. As one can see detection of two charged hits in FW detector should significantly enhance contribution of such channels. Therefore, if decays of these mesons are explanation of the observed excess in the inclusive spectrum their contribution to the pair production associated with two charged particle hits in FW should be even more pronounced.

Indeed, an important part of e^+e^- yield at high mass region is $\eta \rightarrow e^+e^-\gamma$ Dalitz decay. As it was discussed in section 3.5 cross section for the η production in $p+p$ and $n+p$ reactions are very well known and were implemented in the simulations. Due to kinematical threshold η meson production is associated with proton emission at very low polar angles. Therefore for the exclusive analysis, not only e^+e^- pairs in the HADES spectrometer acceptance are required, but also another proton (besides proton spectator) has to be registered in the Forward Wall (FW) detector.

In order to select such channels events with 3 hits collected in FW have been chosen. Hits detected in FW were sorted by means of the increasing polar angle.

If the charged particles induce a signal in the adjacent FW cells they are clustered and treated as a single hit if two or more hits in the closest neighborhood have time of flight difference smaller than $5ns$ (see below). In this case physical variables as θ, ϕ, p are averaged over all contributing pads from a cluster.

Momentum of a charged particle detected in the Forward Wall is calculated from time of flight under assumption that it is a proton. If momentum of the particle is found between $1.6GeV/c$ and $2.6GeV/c$ (wide range determined by simulation), it is assigned as spectator. If more than one particle fulfills this condition, as the spectator the one with smaller θ

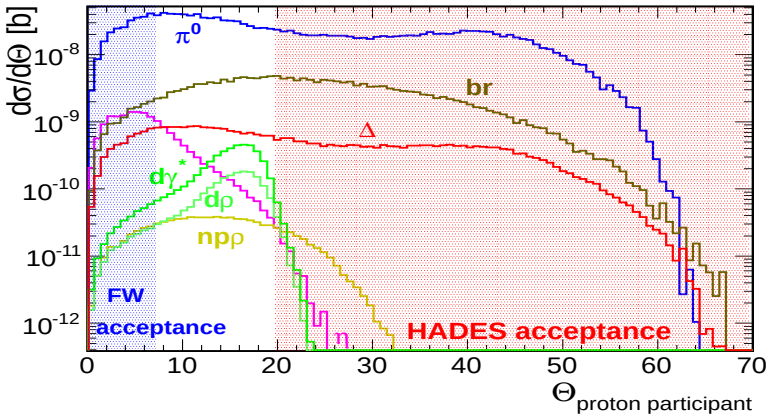

Figure 3.41: Polar angle distribution of the proton participating in the reaction for all simulated channels. Blue and red regions represent the Forward Wall and the HADES acceptance region.

angle is chosen.

Fig. 3.42 shows time differences between hits in cells that form a cluster. Since the Forward Wall is composed of three groups of cells of increasing size (2×2, 4×4 and 8×8 cm^2) the time difference has been shown for each group separately. The Gaussian fits deliver sigma values equal 0.80, 0.84 and $1.14ns$, which give us, according to formula $\sigma/\sqrt{2}$, time resolution amounting to: $0.56, 0.60, 0.81ns$. This is a little bit more than resolution obtained in the paper [68].

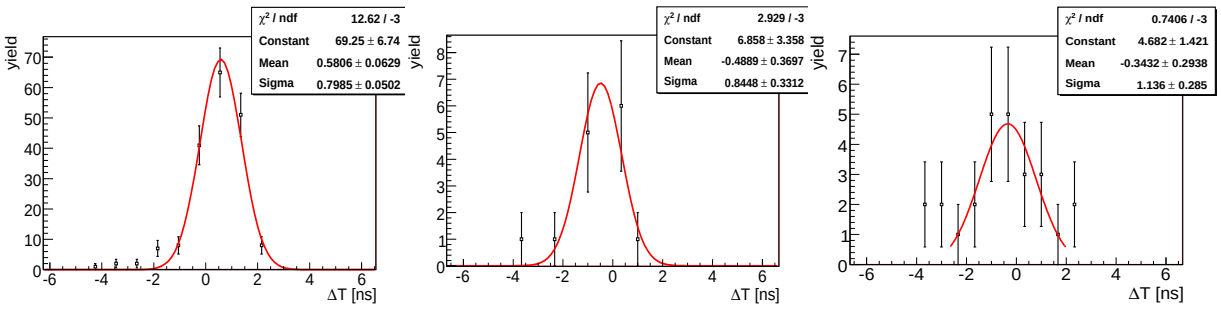

Figure 3.42: Time difference of two hits belonging to one cluster for the following sizes of cells of FW detector: 4×4, 8×8, 16×16 cm^2. Gaussian fits are presented as a red curve.

To demonstrate that the cluster separation is done properly, Fig. 3.43 shows the time difference between two independent clusters for the $M_{inv}^{e^+e^-} > 280 MeV/c^2$. One can clearly see that a participated proton is well separated in time from the proton spectator, however there is a significant unexplained contribution with $\Delta > -5\ ns$. Simulated spectra, shown on the left hand side picture, contain bremsstrahlung model of Kaptari (model "B"), while on the right side only Δ Dalitz (model "A") was included in the simulated cocktail. A red hatched area shows a range spanned by the two extreme assumptions about ρ production, like in Fig. 3.28.

Because of small intensity model "A" has been rescaled to be equal with model "B" in this chapter (they will be marked in pictures as Δ_x) in order to compare their shapes.

For both plots in Fig. 3.43 one can notice that the shape of model "A" fits better to the experimental spectrum for ΔT between -5 and $0ns$ (where the clusters are separated in space, but not in time) but is too small in the real magnitude to explain observed yield.

One should notice the experimental dilepton's excess in the Fig. 3.43 is the same excess as in Fig. 3.44.

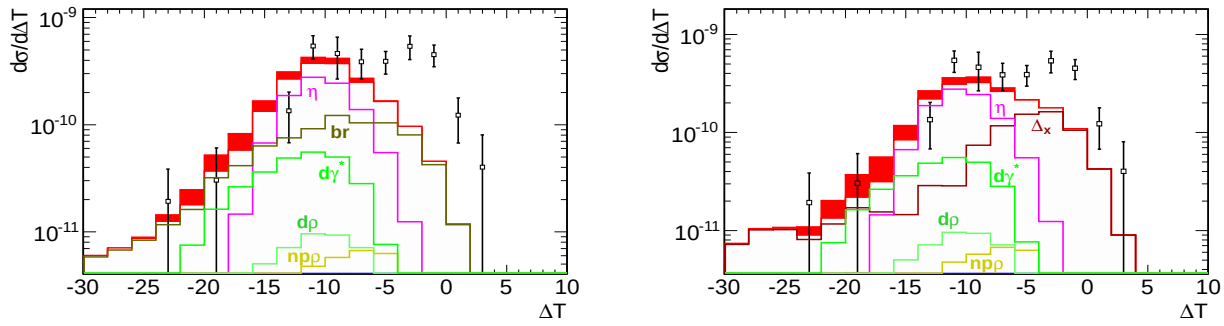

Figure 3.43: Time difference between two separated clusters in FW for $M_{inv}^{e^+e^-} > 280 MeV$. Left: to the sum of simulated channels model "B" is included. Right: model "A" is included.

After discussion about the method of two hit reconstruction in FW we can come into comparison of our model with various distributions obtained for the events with reconstructed two charged particles in FW (assumed to be protons) and e^+e^- in HADES.

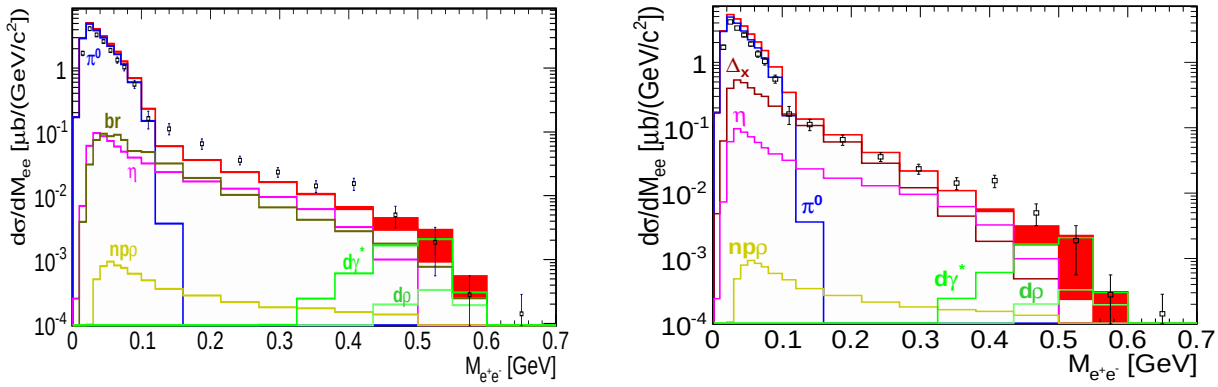

Figure 3.44: Invariant mass distribution of e^+e^- obtained for events with two hits in FW. Left: model "B". Right: model "A".

As first e^+e^- invariant mass spectra is shown in Fig. 3.44, where experimental and all simulated channels are presented. They look different than in Fig. 3.28 because of condition for selection of two charged hits in FW. The dielectron enhancement above simulated cocktail is smaller (in particular for model B) what indicates that it is not associated with events with two charged hits in FW. Cocktail with model A has even smaller excess, because this channel has a larger cross section for dielectrons than model (B) including only Δ production. Using additional production channel $d\gamma^*$ as a "ρ-like" source the simulated spectra improves agreement with experimental data above $M_{ee} > 450MeV$.

In the next Fig. 3.45 the e^+e^- missing mass distributions for the events with one hit in FW (only spectator selection) are presented. They are plotted for $M_{inv}^{e^+e^-} > 280MeV$ where excess is the largest. From these distributions it seems that the excess is compatible with kinematics expected for the bremsstrahlung, Δ and η channels. They have a broad pn mass instead of narrow one expected for the $d\rho$ channels. Even if the cross section for ρ particles could be increased, it would influence the region of M_{miss}^{ee} between 1.75 and $1.9GeV/C^2$ (which is already well described) while the excess is mainly located at higher missing masses. It is worth to note that although Δ channel has smaller contribution than bremsstrahlung, it has maximum in the region of $2.0GeV/c^2$ (for bremsstrahlung it

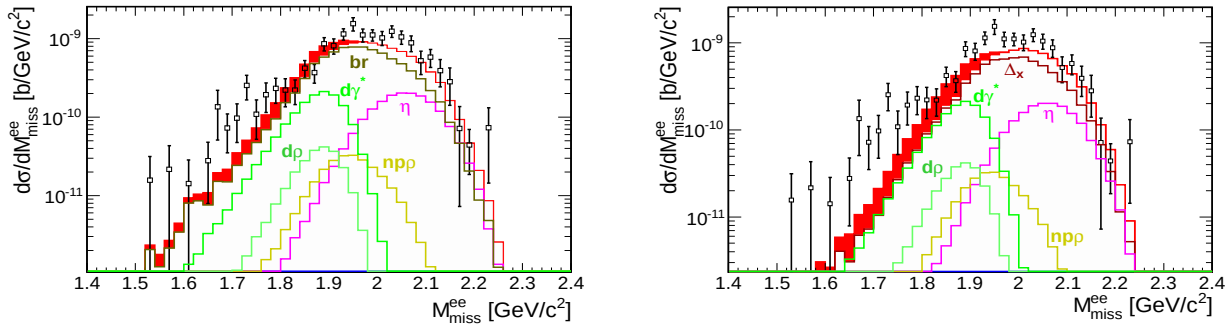

Figure 3.45: Missing mass of e^+e^- for $M^{e^+e^-}_{inv} > 280MeV$ in the case when electron and positron and at least one proton are identified. Left picture contains bremsstrahlung, right one Δ channel. Channels are described with colors in figures.

is $1.94GeV/c^2$), which better fits the experiment.

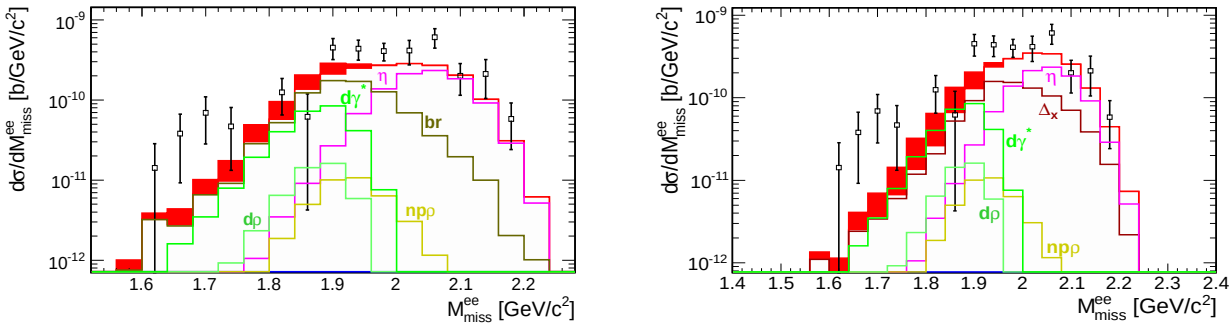

Figure 3.46: Missing mass of e^+e^- for $M^{e^+e^-}_{inv} > 280MeV$ in the case when electron and positron and at least two protons are identified. Left picture contains bremstrahlung, right one Δ channel. Channels are described with colors in figures.

Fig. 3.46 presents the same missing mass distributions (shown in Fig. 3.45), but with the additional condition for identification of the charged hit in FW which is assumed to be proton. In these distributions η and ρ contributions are more important and almost describe the whole yield, what can be understood from Fig. 3.41. Their contribution is enhanced if one selects events with two charged particles in FW. However, from comparison of Fig. 3.45

and Fig. 3.46 one can conclude that such processes which include heavy meson production are not responsible for the dielectron excess observed in the inclusive spectrum.

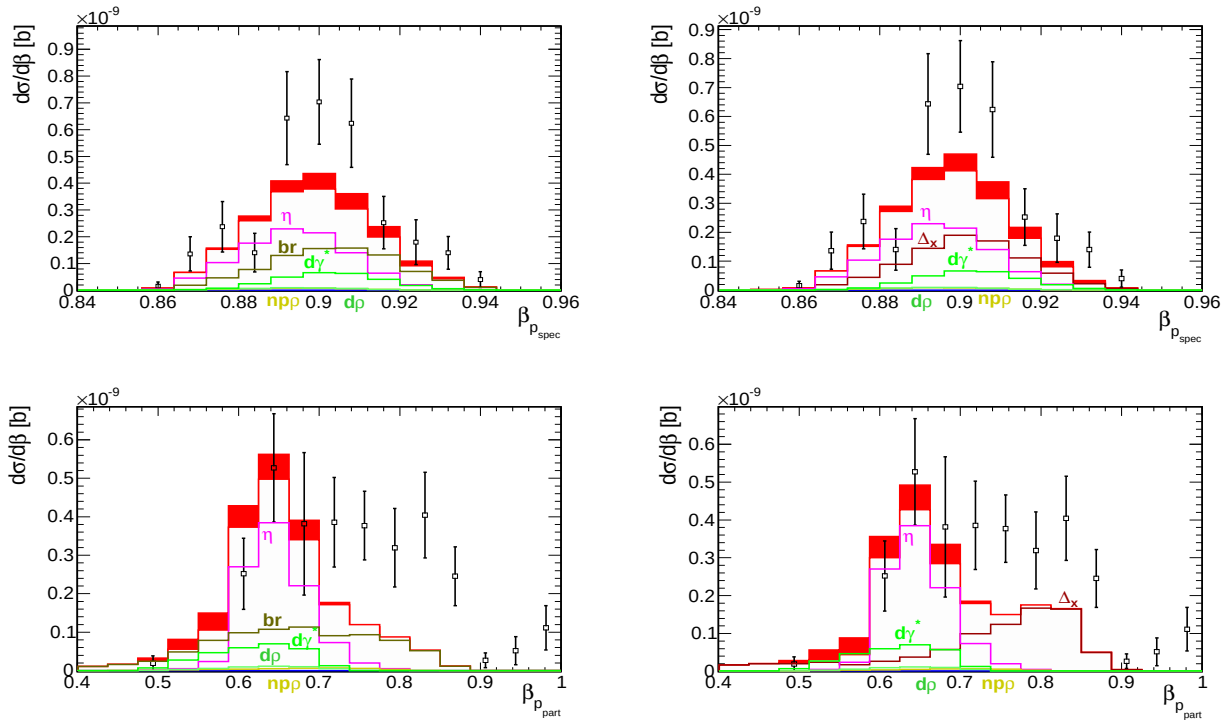

Figure 3.47: Velocity of proton spectator (upper figures) and proton participated in the reaction (lower figures) for $M_{inv}^{e^+e^-} > 280MeV$.

In the four pictures (Fig. 3.47) distribution of velocity (β) of charged particles detected in FW is shown. As one can see shape of distributions for spectator protons (upper row) are described properly by simulations. The missing yield is just a consequence of the pair excess at higher masses. Furthermore, it seems that abundance of η channel in simulation is consistent with the measurement since both distributions are consistent at low velocities where η channel contributes. Moreover, one can conclude that Δ channel would better fit the data, which is particularly seen in the distribution of β of the proton from the reaction. Indeed, the excess appears for the β between $0.7 - 0.9$, where only bremsstrahlung or Δ channel are available. This is the next evidence for underestimation of the final states of the pne^+e^- type ("Δ-like" decays) in the excess.

Below, in Fig. 3.48 the distributions of opening angle between protons are shown. They give evidence that not only our simulation properly reproduces experiment, but also for small values of opening angle (around 2 degrees) one can find sign of FSI interactions in the last one (the FSI was not included in simulation).

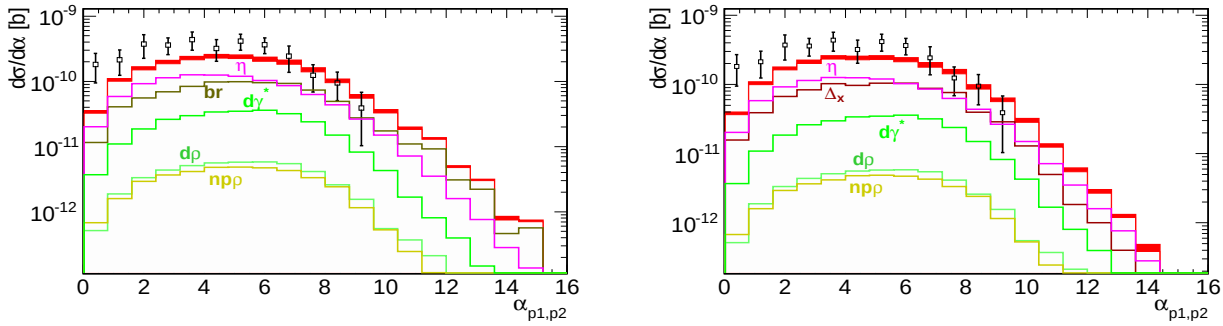

Figure 3.48: Opening angle between protons in FW for $M_{inv}^{e^+e^-} > 280MeV$.

The pne^+e^- analysis confirms dielectron experimental excess is generated by Δ/bremstrahlung-like mechanism. It removes speculation about additional channel with deuteron or insufficiency channel with ρ or η.

Chapter 4

Summary

In this thesis I characterized in detail $d+p$ reaction at the $1.25GeV$ of kinectic energy. First I presented the motivations which run the experiment on the HADES detector in 2006. The spectrometer itself was described in the next section. The analysis of collected data was divided in three parts:

1. Comparison of experimental data with simulation of reaction $d+p$ at $1.25AGeV$, which allows to describe the excess of dilepton pairs in the meaning of angular distributions and compare them with the model.

2. Comparison of distributions for elementary and heavy ion reactions. One can conclude that the excess is created on the elementary stage of reaction.

3. Conclusion that the exclusive pne^+e^- reconstruction indicates the source of the excess as Δ or NN bremsstrahlung channel. The ρ and η channel in the current magnitude reproduce properly the experimental data and increase of their magnitude only reduce the agreement with experiment. On the second hand the shape of Δ channel fits better than bremsstrahlung model to the dilepton excess.

Appendix A

Data aquisition system

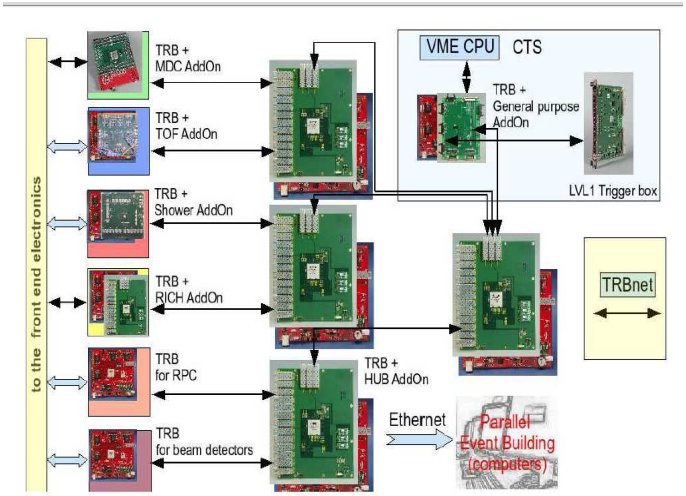

Figure A.1: The new data acquisition system (DAQ).

HADES will be moved to the upcoming FAIR (Facility for Antiproton and Ion Research) accelerator complex, where its experimental program will be continued up to $8GeV$ of kinetic beam energies per nucleon. The average amount of data is expected to be 300 MB/s and mean trigger frequency will be $20kHz$ ($100kHz$ in peak). In order to fulfill these requirements the HADES readout and trigger system is currently under upgrade.

An overview of the new Trigger and Data Acquisition system is shown in Fig. A.1. The

complete readout chain consists of the following basic elements:

- front-end electronics,
- readout electronics,
- slow control and trigger distribution system,
- event building system.

The first level trigger (LVL1) decision is created based on the charged particle multiplicity provided by TOF and TOFINO photomultipliers. The response time for these detectors is up to $t < 100ns$. After the data have been readout from the front-end electronics (after positive LVL1 trigger), the acquaired data from the RICH, TOF and a Pre-Shower detectors is taken into account to calculate the LVL2 trigger decision. A level-2 (LVL2) trigger algorithm selects events by searching for the electron candidates.The positive decision from LVL2 induces a full readout of data from all sub-detectors.

In order to handle a latency, which corresponds to several events (on the average it is 5-10 events), the readout boards must have buffers large enough to hold the data for this time. If a LVL2 decision is issued, the data of the corresponding event is sent via UDP network protocol to the Event Builder (EB). The EB is a PC which combines the data from different asynchronous data sources into complete events and finally writes them to the mass storage.

Up to now each subdetector has dedicated individual readout system. In the new design the "Trigger and Readout Board" (TRB), shown in Fig. A.2, will be used as a general platform for all subsystems. Together with a given AddOn board, that is assigned to a particular subdetector, TRB composes one physical unit.
The current version of TRB contains:

- Etrax FS processor with $128MB$ memory connected to the $100MBit/s$ Ethernet, with a standard Linux 2.6 kernel. It will be described later,

- 128-channel Time to Digital Converter electronics, with time resolution $\sigma = 40ps$, based on the HPTDC from CERN,
- optical link with throughput of $2GBit/s$,
- programmable logic FPGA (Field Programmable Gate Array), called Xilinx Virtex 4, connected to all main components on the TRB to manage data flow on the board,
- TigerSharc DSP (Digital Signal Processor),
- a high data rate digital interface connector (32 LVDS lines, $15GBit/s$ and 32 TTL lines). It gives the possibility to mount AddOn boards to the TRB, which provide the detector specific interfaces or additional computing resources.

All the detector specific functions are performed by the detector dependent AddOn boards, which is mounted on the TRB. According to this concept, following AddOn boards were built:

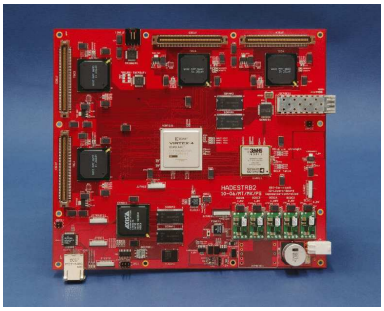

Figure A.2: The front view of the Trigger and Readout Board.

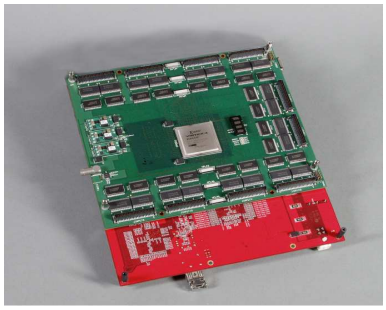

Figure A.3: The MDC AddOn mounted on the TRBv2 top. Here, the back side of the TRBv2 is visible in parts.

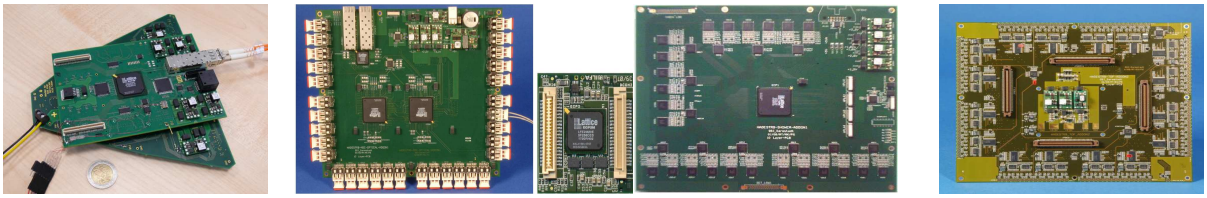

for: RICH, MDC, Pre-Shower and TOF.

A.0.1 Device driver for Etrax FS and Direct Memory Access (DMA) technology

In this chapter the second version of TRB is presented. A first version (TRBv1) was used successful during the beam time April 2007 to readout the forward wall and the beam detectors.

The TRBv1 was fully integrated into the HADES DAQ system. $80kHz$ on LVL1 (with large down scaling) was achieved and LVL2 rates up to $18kHz$, which corresponds to the data rates of $1.8MB/s$. One should point out, that without DMA capabilities on the Etrax, the processors performance has to be shared between the HADES sub event building software and the readout from the LVL2 memory.

The design goal after optimization is $80kHz$ LVL1 rate and a LVL2 bandwidth of 10 $MByte/s$. In order to make it possible the collaboration decided to use direct memory access (DMA) technology in the process of readout. To explain how this new technology is implemented in our design, first some details about Etrax FS , Fig.A.4, will be presented.

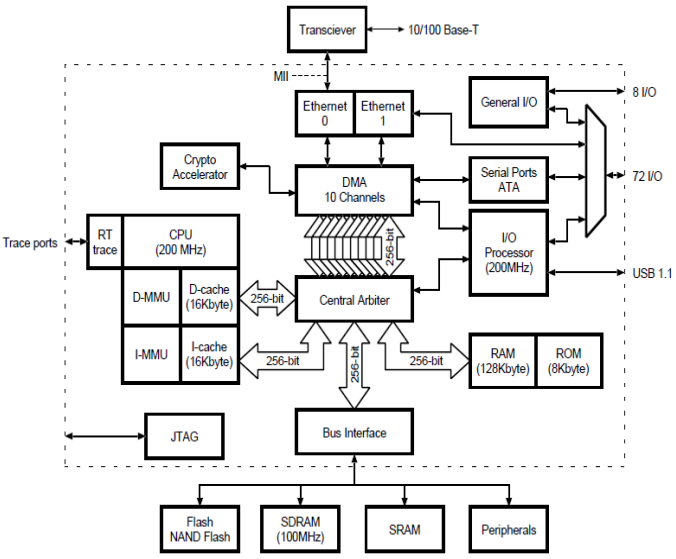

Figure A.4: Overview of the Axis Etrax FS.

The main elements of the Etrax FS chip are:

- $200MHz$ RISC (Reduced Instruction Set Computers) processor with a 32-bit data and address width with the standard Linux kernel installed,
- micro-code programmable I/O processor consisting of three $200MHz$ 32-bit processors with local memory and hardware accelerators for real-time performance,
- 10 DMA channels each with 64 bytes FIFO (First In First Out buffer),
- dual $10/100Mbit/s$ full duplex Ethernet,
- several synchronous and asynchronous I/O ports with 80 read/write configurable I/O pins.

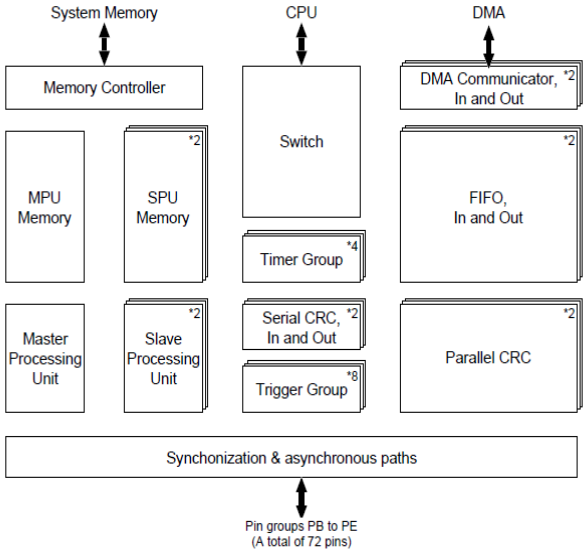

Figure A.5: Block diagram over the I/O Processor.

As one can see in Fig. A.5, the I/O Processor is not a processor in a conventional sense. From a software perspective it should be considered as a collection of blocks, which are connected to each other in a chip-specific manner. However, the flow of data are configurable

with regards to which hardware blocks the data should traverse on its way to or from a peripheral device.

The I/O processor contains one Master (MPU) and two Slaves (SPU) Processing Units. When the first one can be consider as a traditional processor with interrupt (IRQ) handling capabilities, SPUs differ from an ordinary CPU, because they can't handle interrupts and SPUs can execute state-machine code in a special mode called FSM-mode. The one of the most important module presented in Fig. A.5 is the switch, which is used to configure the individual connections between the modules of the I/O Processor.

The connections are defined by registers inside the Switch in the way to construct a chain, where data will be transfer from I/O ports to DMA channel. After that data are handled by a device driver.The DMA channel is a bus where data are moving (reading/writing) without using the central processing unit (CPU). The wholeness was presented in the Fig. A.6.

Regardless of used AddOn boards (or in the case when front-end electronics are connected directly to TRB) the experimental data go to FPGA chip. In the case of positive LVL2 trigger decision they are forwarded to the first SPU of Etrax FS via I/O ports and the parallel data path (PDP).

Next the data are sent to the device driver in the package of fifteen 32-bit words and are stored in the dedicated buffer.

On demand of readout application these events are copied from this buffer and sent via Ethernet to the Event Builders all the time. This visual scheme was presented in the Fig.A.6 inside violet box.

The protocol between FPGA and Etrax FS is presented in the same figure, but in the yellow frame. When 32-bits word is written on port B and C, a trigger from FPGA on the pin 16 of the port B is set. Then data are automatically readout by Etrax chip and it is routed over a dedicated path to DMA Communicator-In (DMC-In). Because of the size of DMC-In buffer FPGA sends data to Etrax as a chain of 15 words with a constant frequency. SPU was set to be sensitive for trigger going from FPGA and after the first-in-the-chain FPGA trigger SPU sets busy signal on pin 17 of the port B. This signal informs

FPGA to not send next chain of words. In this state FPGA chip can only finish writing a current chain of data. After the busy state was set, SPU is waiting some time needed

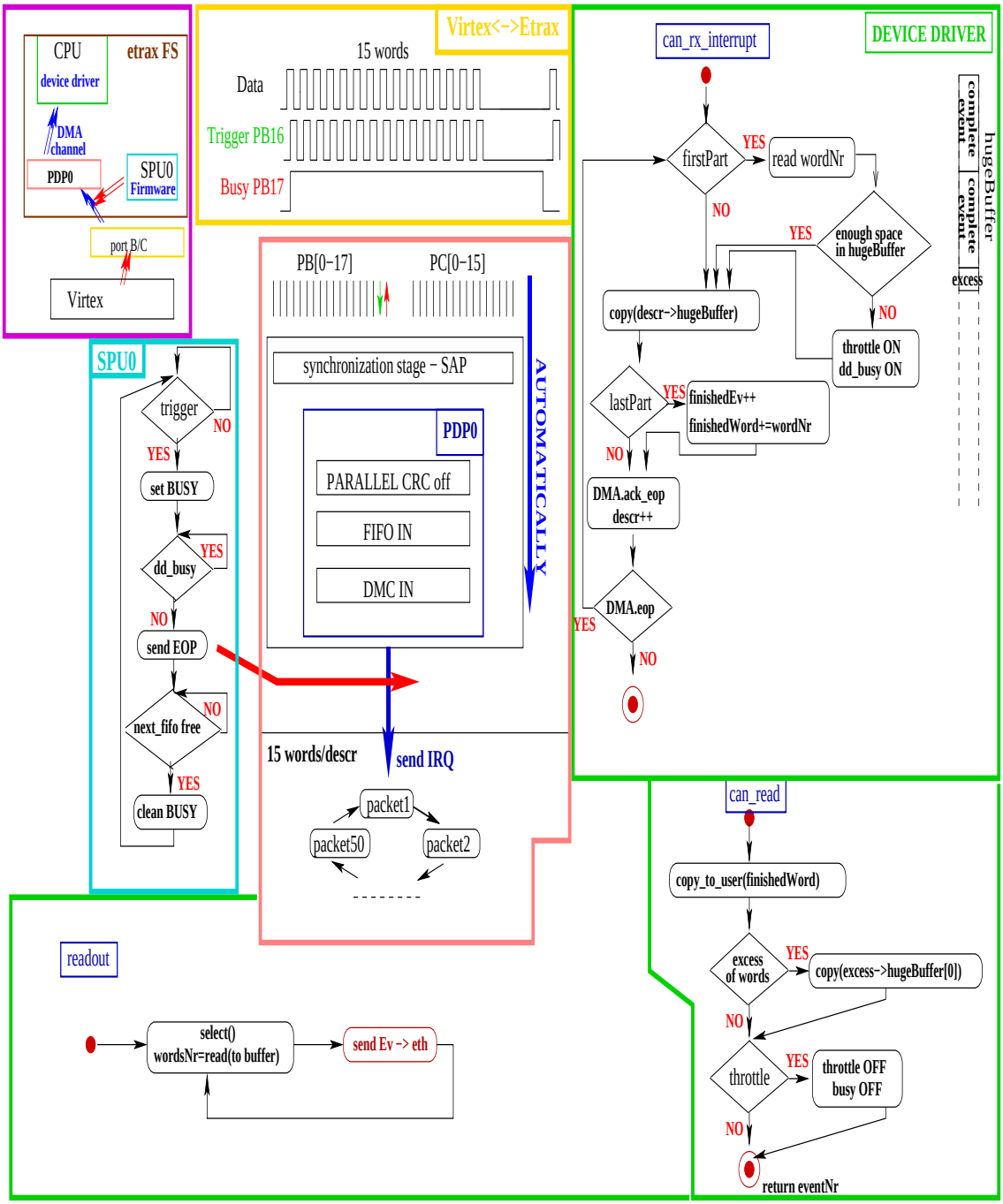

Figure A.6: The data flow diagram.

to gather 15 words and then it checks if a device driver busy state ("dd_busy") is set. If not, SPU writes 16. word to DMC-In which contains EOP (End Of Packet) signal which induces rewriting data from DMC-In buffer to DMA channel. In practice, it means that data are available via the device driver. This is the main step of SPU logic. After the whole process, the busy signal is cleared and the whole cycle is repeated (Fig. A.6, blue box).

The data path inside modules managed by the switch is presented in the Fig. A.6, pink frame. In the previous paragraph automatic readout of data was mentioned. The logic values from pins on ports B and C are readout and synchronized by the Synchronization and Asynchronous Paths (SAP) module. At the moment of the trigger arrival the Synchronization and Asynchronous Paths (SAP) module readouts the logic values from pins on ports B and C. The data is synchronized (32-bits word as BUS1 is created) and adapted to the I/O Processor $200MHz$ clock. After that the word goes to the Parallel Data Path In (PDP-In) module. It consists of Parallel CRC, Fifo-in and DMA Communicator-In (DMC-In) modules. Each of these modules are connected with the next one and data flows freely up to the DMC-In. When the word with EOP sent by SPU reached DMC-In, an eop-interrupt to CPU is sent. The next word will be written to the next packet. These packets are, we can say, interface between SPU and CPU. SPU controls writing data to them, while CPU is reading them and sending to readout application. There is no need to sending any information about availability of empty packets, because this is controlled by SPU ("next_fifo free" request).

The eop-interrupt calls "can_rx_interrupt" function in the device driver, Fig. A.6 it is represented by one of the green frames. This part of driver logic handles the incoming packets. Most of the non-empty events contain more than 15 words, therefore usually more than one packet belongs to one event. Taking this into consideration one needs to read a header of each event from the first packet of event and extract a number of words in that event. Then the packet is copied (always 15 words) to a main buffer and if the last packet of event arrived the position of the next event in the main buffer will be adjust to the real size of previous event. The data in the data acquisition system are 64-bit aligned, when the number of words in the event is uneven, one empty words is added. If the main buffer

has no space for the next event, "dd_busy" is set.

The function described above responds for the request from SPU and is responsible for the moving the events to the main buffer. On the other hand, there is "can_read" function. It is triggered by "readout" application and copies a finished events to it. It could happen that "can_read" function was called, when the main buffer contains not only the finished events, but additionally one partly-completed event. In this case, this unfinished event is copied at the beginning of main buffer.

The last application on the way of an event from I/O ports to Ethernet is the user space application called "readout" It consists mainly of three methods:

- select(), to wait if at least one event is located in the main buffer,
- read(), to read finished events to the local buffer,
- NetTrans_send(), to send data through the Ethernet to the eventbuilder.

After implementation of the above logic the rate of events increased from $40k/s$ to $125k/s$ with covering 15 words per event, which corresponds to $11MB/s$ of UDP Ethernet transfer. It is shown in Fig. A.1.

Table A.1: Data transfer in the DMA mode with different data load.

32 bit words per event	LVL1 frequency $[kHz]$	Speed $[MB/s]$
14	124	11
22	82	9.2
38	44	8.5
64	27	8.1
110	18	7.9
170	10.5	7.8
640	3	7.7

Appendix B

Self consistency check of acceptance and efficiency matrices

The procedure of full analysis of simulation is long-lasting and complicated. It covers the following steps:

1. Generation of events of given reaction.

2. GEANT package which defines the detector geometry and generates detector hits based on a realistic modeling of the physical processes occuring along the tracks.

3. DST production, where the hits are digitized and analyzed, among others: calculation of track of particles, its momentum and polar and azimuthal angle.

4. PAT tool to check the event hypothesis and set the type of each particle.

Instead of above mechanism, one can use a different method which is based on filtering the generated events by acceptance and efficiency matrices. Second reason to create these matrices is that if we one wants to compare their specra with another experimentalal group this comparison should proceed after correction for efficiency where the proper matrix is needed.

To check if these matrices were produced right, set of actions have been performed:

A) creating acc./eff. matrices

1. gathering the vertex of event from DST files to about 1000 files;
2. simulation of "white tracks" (particles with flat distributions of momentum, θ and ϕ; one track per HADES sector) in Pluto generator for each kind of particle (e^+e^-p);
3. generating the detector's response in GEANT;
4. DST production with "embedded" background. It means that the background is not simulated, but taken from experimental data;
5. create the acceptance matrices with designed macro, shown in Fig. B.1;
6. running 1-prong PAT and create the efficiency matrix, Fig. B.1;

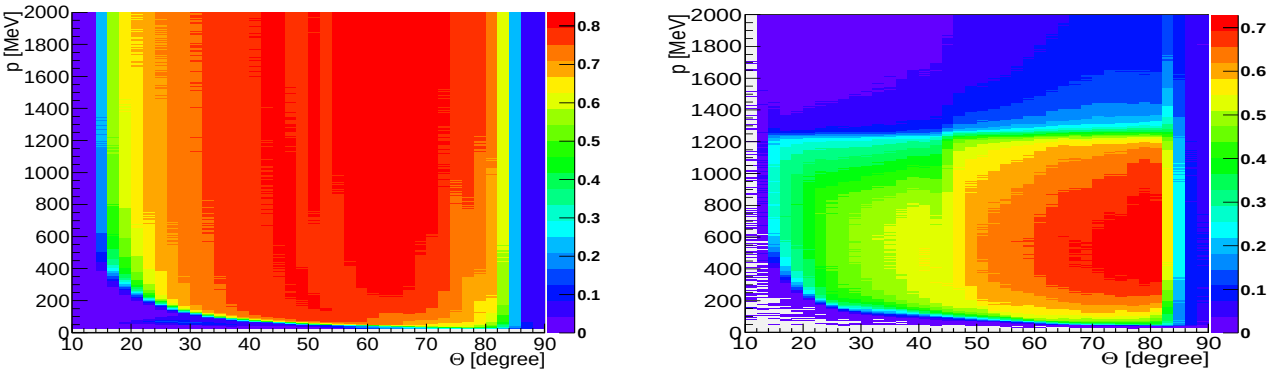

Figure B.1: Acceptance (l.h.s.) and efficiency (r.h.s.) matrices for positron in pp@1.25GeV.

B) full analysis of physical channel belongs to given reaction

1. gathering the vertex of event from DST files to about 100 files using limit of events;
2. simulation of physical channel events in Pluto generator;
3. generating the detector's response in GEANT;
4. DST production with "embedded" background with this same limit as used in the 1. point;
5. running 2-, and higher prongs PAT;

6. draw the difference between reconstructed and ideal momentum, θ and ϕ distribution in order to get smearing and desmearing spectra. presented in Fig. B.2.

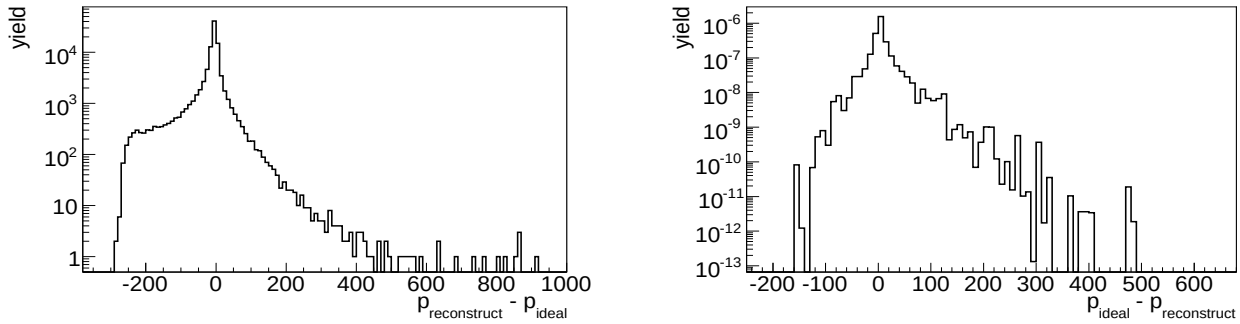

Figure B.2: Smearing (l.h.s.) and desmearing (r.h.s.) histograms for positron for the slice of $300 - 310$ MeV respectively of ideal and reconstructed momentum in $pp@1.25GeV$.

C) filtering the events with matrices

1. Simulation of physical channel events in Pluto generator (the same step as above).
2. Filtering events with acceptance matrices.
3. Filtering events with efficiency matrices.
4. In case of need smearing the physical values in momentum and angles.

D) creating correction for pairs

In contrast to procedure of creating matrices, in the full simulation can happen that more than one particle hit the same sector. It is the fact that efficiency is falling with increasing multiplicity of hits. In order to restore this disagreement all spectra taken in the full chain analysis have to be improved. This correction depends on the opening angle of e^+e^-. Therefore the best way to create it is to divide the distribution of this angle (constucted on the base of ideal values) for full simulation and events filtered with acceptance/efficiency matrices for cases when both e^+e^- are heading to the same sector. The curve fitted to this correction is presented in Fig. B.3.

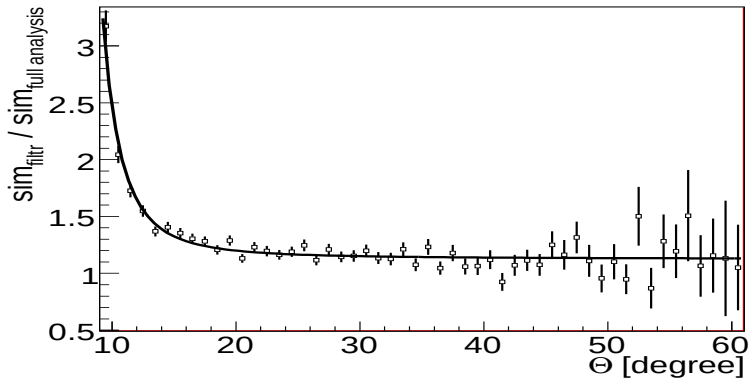

Figure B.3: The fitted correction for pairs going to the same sector.

E) final comparison of full and filtered simulation

1. first confrontation should be done between the e^+e^- invariant mass calculated based on ideal values from the full simulation and events filtered with acc/eff matrices. See Fig. B.4;

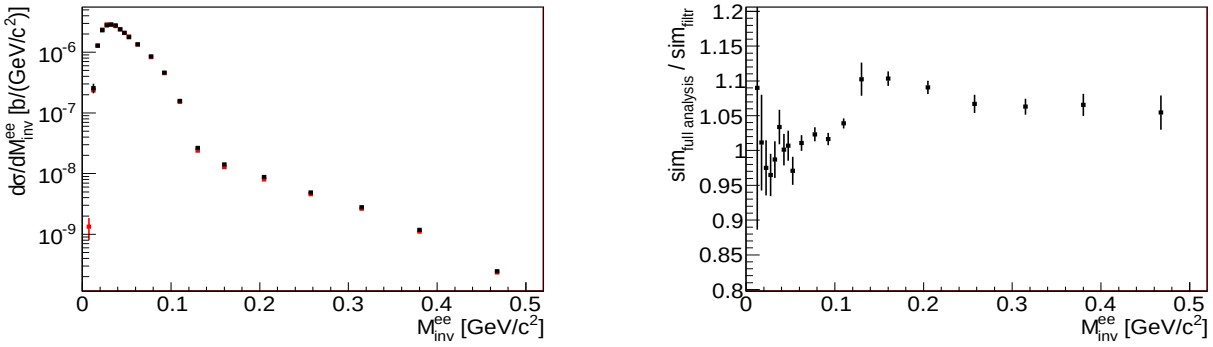

Figure B.4: Comparison (l.h.s.) and ratio (r.h.s.) both method of analysis. The invariant mass for full chain (black) calculated based on ideal values, filtering method (red) using both kind of matrices (acc/eff) without smearing momentum, Θ and ρ.

2. to check smearing method one should pass on to reconstruted values in full simulation and smear the physical values in filtering events, shown in Fig. B.5;
3. compare the full simulation after efficiency correction using desmeared reconstructed

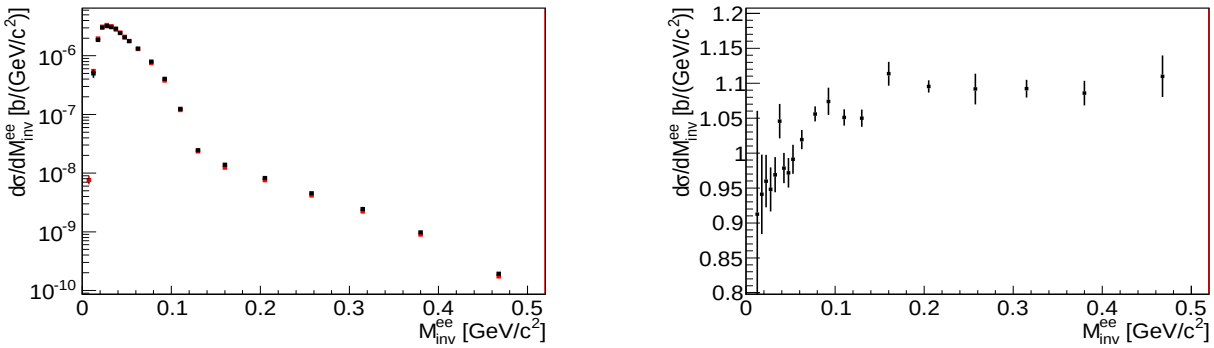

Figure B.5: Comparison (l.h.s.) and ratio (r.h.s.) of M^{ee}_{inv}. This time with using reconstructed/smearing values.

values and events filtered only by HADES acceptance, presented in Fig. B.6. In case of $pp@1.25GeV$ the differences were on the level of 15%;

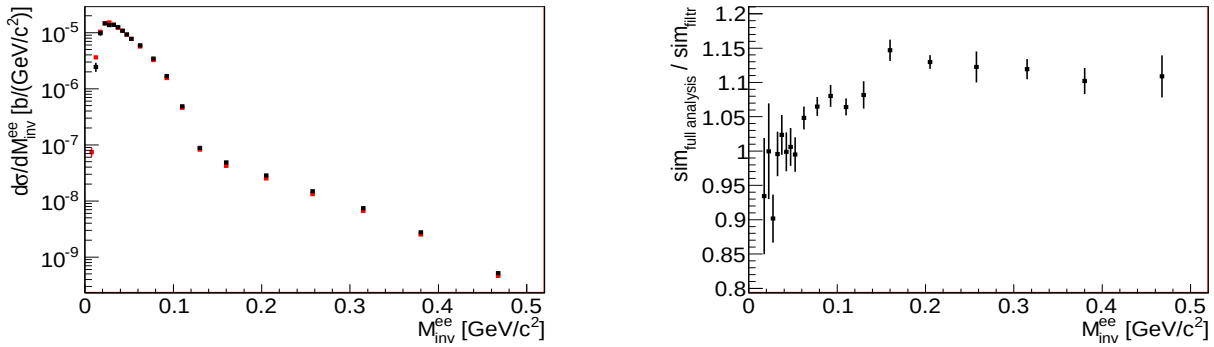

Figure B.6: Comparison (l.h.s.) and ratio (r.h.s.) of M^{ee}_{inv}. Full analysis is corrected for efficiency and events are filtered only with acceptance matrix.

More details one can find at the www-page [69].

Acknowledgements

I would like to gratefully acknowledge my advisor, Prof. Dr Piotr Salabura for his support, critique and many advices, especially for "not to force the open door".

I would like to thank my colleagues from Cracow:

Dr. Witold Przygoda - for all the scientific and non-scientific discussions

Dr. Tomasz Wojcik - for his guidance in software world

MSc Annie Kożuch, msc Adrian Dybczak, msc Marek Pałka and msc Damian Gil - for being so good friends through all these years of studies.

I am thankful to my wife, who always stands beside me.

It has been a great experience to work within the HADES collaborations.

Every meeting was full of inspiring discussions and new exciting tasks. Especially I would like to thank Michael Traxler, who showed me how challenging hardware can be.

Bibliography

[1] G. Agakichiev et al., "The High-Acceptance Dielectron Spectrometer HADES", Eur.Phys.J. A41:243-277, 2009

[2] G. Roche et al., "Dielectron production in Ca+Ca collisions at $1AGeV$ And $2AGeV$", Phys. Lett., B229:228, 1989

[3] A. Marin at al., "Dilepton measurements with CERES", PoS CPOD07, 034, 2007

[4] M. Floris at al., "Low Mass Dimuon Production in Indium-Indium Collisions at the CERN SPS", nucl-ex/0606023, 2006

[5] G.Q. Li, C. Gale, "Intermediate-mass dilepton production in heavy-ion collisions at $200AGeV$", Phys.Rev.Lett.81:1572-1575,1998

[6] S. Afanasiev, et al., "Enhancement of the dielectron continuum in $\sqrt{s_{NN}} = 200GeV$ Au+Au collisions", arXiv:0706.3034[nucl-ex]

[7] Earl K. Hyde, "Bevalac: Status of the Machine and of the Physics Research Program", Physica Scripta. Vol. 10A, 30-35, 1974

[8] A. Yegneswaran et al., "The dilepton spectrometer", Nucl. Instr. and Meth. A290, 61 (1990)

[9] R. Porter et al., "Dielectron cross section measurements in nucleus nucleus reactions at $1.0AGeV$", Phys. Rev. Lett., 79: 1229, 1997

[10] V.D. Toneev et al., "Hadronic sources of dileptons from heavy ion collisions at intermediate and relativistic energies", Phys. Lett. B287, 302 (1992)

[11] E. Abouzaid at al., "Measurement of the Rare Decay $\pi^0 \to e^+e^-$", Phys. Rev. D75, 012004 (2007)

[12] Gy. Wolf, G. Batko, "Dilepton production in heavy-ion collisions", Nucl. Phys. A517, 615-638, 1990

[13] L.G. Landsberg, "Electromagnetic decays of light mesons", Phys. Rep. 128, 301 (1985)

[14] W. K. Wilson et al., "Inclusive dielectron cross sections in $p+p$ and $p+d$ interactions at beam energies from 1.04 to $4.88GeV$", Phys.Rev.C57: 1865-1878, 1998

[15] C. Fuchs, A. Faessler, "Dilepton and vector meson production in elementrary and heavy ion reactions", Nucl. Phys., A755:499-502, 2005

[16] G.E. Brown, M. Rho, "Scaling effective Lagrangians in a dense medium", Phys. Rev. Lett. 66 (1991) 2720.

[17] L.P. Kaptari, B. Kaempfer, "Di-electron bremsstrahlung in intermediate-energy pn and Dp collisions", Nucl. Phys. A 764 (2006) 338

[18] C. Ernst, S.A. Bass, M. Belkacem, H. Stocker, W. Greiner, "Intermediate mass excess of dilepton production in heavy ion collisions at relativistic energies", Phys.Rev.C, vol. 58, nr 1, july 1998

[19] C. Gale, J. Kapusta, "Dilepton radiation from high temperture nuclear matter", Phys. Rev. C35, 1987, 2107

[20] E. L. Bratkovskaya et al., "Low-mass dileptons and dropping rho meson mass", Phys. Lett. B445 (1999) 265-270

[21] B. Andersson, G. Gustafson, "A high energy string dynamics model for hadronic interactions", Lund preprint LUTP - Phys, 1987

[22] B. Andersson, G. Gustafson, Hong Pi, "The FRITIOF model for very high energy hadronic collisions", Z. Phys. C 57,485-494 (1993)

[23] E. L. Bratkovskaya, W. Cassing, "Dilepton production and off-shell transport dynamics at SIS energies", Nucl. Phys. A807, 214-250, 2008

[24] E. L Bratkovskaya et al., "Perspectives of e^+e^- production in pp, pd and pBe reactions at SIS energies", Nucl.Phys A686 (2001) 568

[25] V.V. Shklyara,b, B. Kampfer, B.L. Reznik, A.I. Titova, "Bremsstrahlung in intermediate-energy nucleon reactions within an effective one-boson exchange model", Nucl. Phys. A628: 255-274, 1998

[26] M. Schaefer, T.S. Biro, W. Cassing, U. Mosel, "e^+e^- production in proton-neutron collisions", Phys. Lett. B 221 (1989) 1-5

[27] R. Shyam, U. Mosel, "Role of baryonic resonances in the dilepton emission in nucleon-nucleon collisions", Phys. Rev. C 67, 2003, 065202

[28] F. de Jong, U. Mosel, "The effect of electro-magnetic formfactors on dilepton production off pp-collisions", Phys. Lett. B 392, 1997, 273

[29] G. Rawitscher, "Calculation of the two-body T-matrix in configuration space", Few-Body Systems, Volume 44, Numbers 1-4 / December, 2008, 245-247

[30] R. Shyam, U. Mosel, "Dilepton production in proton-proton and quasi-free proton-neutron reactions at $1.25GeV$", arXiv:1006.3873

[31] R. Shyam, U. Mosel, "Dilepton production in nucleon-nucleon collisions reexamined", Phys. Rev. C, 79, 2009, 035203

[32] Y. C. Pachmayer et al., "Dielectron Production in ^{12}C + ^{12}C Collisions at $1GeV/u$ and the Solution to the DLS Puzzle", Nucl.Phys A686 (2001) 568

[33] M. Lacombe, B. Loiseau, J. M. Richard, R. Vinh Mau et al., "Parametrization of the Paris $N-N$ potential", Phys. Rev. C21, 1980, 861

[34] http://www-hades.gsi.de/computing/pluto/html/PlutoIndex.html

[35] http://www.fz-juelich.de/ikp/COSY-TOF/publikationen/index_e.html

[36] The COSY-TOF Collaboration, "Study of spectator tagging in the reaction $np \rightarrow pp\,\pi^-$ with a deuteron beam", European Physical Journal A29 (2006) 353

[37] M. Daum et al., "The reaction $np \rightarrow pp\pi^-$ from threshold up to 570 MeV", Eur. Phys. J. C 23, 43 (2002)

[38] H. Calen at al., "Measurement of the quasifree $p\,n \rightarrow\ p\,n\,\eta$ reaction", Phys. Review C57 (1998) 2667-2670

[39] R. Bilger et al., "Spectator tagging in quasi-free proton-neutron interactions in deuterium using an internal cluster-jet target at a storage ring", Nucl. Instr. Meth. A457(2001) 64

[40] H. Calen, et al., "Detector setup for a storage ring with an internal target", Nucl.Instrum.Meth.A379:57-75, 1996

[41] K. Zeitelhack et al., "The hades rich detector", Nucl. Inst. and Meth., A433:201, 1999

[42] C. Muentz et al., "The HADES Tracking System", Nucl. Instrum. Meth., A535:242-246, 2004

[43] C. Agodi et al., "The HADES Time-Of-Flight wall", Nucl. Inst. and Meth, A492:14-25, 2002

[44] P. Fonte et al., "Development of large area and of position-sensitive timing RPCs", Nucl. Instr. Methods, A(478):170-175, 2001

[45] A. Balanda et al., "Development of a fast pad readout system for the HADES shower detector", Nucl. Inst. and Meth, A417:360, 2004

[46] H. Wind, Nucl. Instr. Method 115(1974) 431

[47] W.H. Press, Numerical Recipes, 3rd Edition, Cambridge University Press (2007)

[48] T. Galatyuk, "Di-electron spectroscopy in HADES and CBM: from $p+p$ and $n+p$ collisions at GSI to $Au+Au$ collisions at FAIR", Doctoral Thesis

[49] J. Lehnert et al., "Performance of the HADES ring recognition hardware", Nucl. Instr. Meth. A502 (2003) 261

[50] F. Krizek, "Study of inclusive electron-positron pair production in collisions of Ar+KCl at $1.756 AGeV$", Doctoral Thesis, 2008

[51] D. Jouan, S. Constantinescu, S. Dita, C. Alexa, S. Langlois et al, "Single muons recombinations as a determination of the combinatorial background in muon pair measurements and estimation of the associated error", Rapport de recherche (2002) 1-23

[52] http://wwwasd.web.cern.ch/wwwasd/geant

[53] http://www-hades.gsi.de/computing

[54] D. Albers et al., nucl-ex/04xxyyy, Eur. Phys. J A

[55] I. Frohlich at al, "A versatile method for simulating $pp \rightarrow ppe^+e^-$ and $d+p \rightarrow ppe^+e^-p_{spec}$ reactions"

[56] V. Dmitriev, O. Sushkov, and G. Gaarde, "$N+N \rightarrow N+\Delta$ angular distribution", Nucl. Phys. A459 (1986) 503

[57] P. Moskal at al, "Near-threshold production of the eta meson via the quasi-free $pn \rightarrow pn\eta$ reaction", Phys. Rev. C 79, 015208 (2009)

[58] M. I. Krivoruchenko, A. Faessler, "Remarks on Delta Radiative and Dalitz Decays", Phys.Rev.D65, 2002

[59] S. Teis at al., "Pion-Production in Heavy-Ion Collisions at SIS energies", Z. Phys. A356 (1997) 421-435

[60] B. V. Martemyanov, M. I. Krivoruchenko, A. Faessler, "Dilepton production in pp and np collisions at $1.25GeV$", arXiv:1108.4265v1

[61] V. Dmitriev, O. Sushkov, C. Gaarde,"Delta Formation In The H-1 (he-3, H-3) Delta++ Reaction At Intermediate-energies.", Nucl. Phys. A459 (1986) 503

[62] M.I. Krivoruchenko, B.V. Martemyanov , Amand Faessler, C. Fuchsa,"Electromagnetic transition form factors and dilepton decay rates of nucleon resonances.", Annals Phys.296:299-346,2002

[63] V. Flaminio, W. G. Moorhead, D. R. O. Morrison and N. Rivoire, "Compilation of cross sections III: p and $\overline{p}$ induced reactions", CERN-HERA 84-01 (1984).

[64] K. Schmidt, E. Santini, S. Vogel, C. Sturm, M. Bleicher, H. Stoecker, "Production and evolution path of dilepton at HADES energies", Phys. Rev. C79: 064908, 2009

[65] K. Lapidus, "Characteristics of dielectron production in d+p collisions @ $1.25AGeV$", HADES Collaboration Meeting XX, Sesimbra, 2009

[66] T. Liu, "Exclusive measurements with the spectrometer HADES in proton-proton reactions at $1.25GeV$", Doctoral Thesis

[67] G. Agakishiev *et al.* [HADES Collaboration], "Origin of the low-mass electron pair excess in light nucleus-nucleus collisions", arXiv:0910.5875 [nucl-ex].

[68] Yanh-Hwan Shin, "Azimutal anisotrope Emission von K^+ Mesonen in Au+Au Stoessen bei $1AGeV$", Doctoral Thesis

[69] http://hades-wiki.gsi.de/cgi-bin/view/SimAna/Apr06SelfconsistencyCheck